Annual Report
Jahresbericht

2004

WALTHER–MEISSNER–INSTITUT
für Tieftemperaturforschung
Bayerische Akademie der Wissenschaften

Contact:

Prof. Dr. Rudolf Gross
Walther–Meißner–Institut für Tieftemperaturforschung
Bayerische Akademie der Wissenschaften
and
Lehrstuhl für Technische Physik – E23
Technische Universität München

Address:

Walther–Meißner–Str. 8	Phone:	+49 – (0)89 289 14201
D - 85748 Garching	Fax:	+49 – (0)89 289 14206
GERMANY	e–mail:	Rudolf.Gross@wmi.badw.de
	WWW–address:	http://www.wmi.badw.de

Secretary's Office:

Jutta Laaser	Phone:	+49 – (0)89 289 14202
	Fax:	+49 – (0)89 289 14206
	e–mail:	Jutta.Laaser@wmi.badw.de
Emel Dönertas	Phone:	+49 – (0)89 289 14205
	Fax:	+49 – (0)89 289 14206
	e–mail:	Emel.Doenertas@wmi.badw.de

Preface

The Walther–Meißner–Institute for Low Temperature Research (WMI) is operated by the Commission for Low Temperature Research of the Bavarian Academy of Sciences. At the same time the WMI is the host institute of the chair for Technical Physics (E 23) of the Technical University of Munich (TUM) with the director of the WMI being ordinarius at the Faculty of Physics of the Technical University of Munich. Since 2004 the WMI also hosts a new scanning probe division. The head of this division, Prof. Bianca Hermann, is professor at the Ludwig-Maximilians-University of Munich (LMU) and also member of the Center for Nano Science (CeNS) of the LMU. That is, the WMI hosts both groups from the TUM and LMU. In this way a tight collaboration has been established between research groups of both Munich universities joining technological and human resources in the fields of experimental and theoretical solid state and condensed matter physics, low temperature techniques, physical chemistry, materials science as well as thin film and nanotechnology.

The WMI carries out research projects at low and ultra–low temperatures and supplies liquid helium to both universities in Munich. It also provides the technological basis for low and ultra–low temperature techniques and methods. The research program of the WMI is devoted to both **fundamental** and **applied research** in the field of **low temperature solid state physics**.

With respect to **basic research** the main focus of the WMI is on

- superconductivity and superfluidity,
- magnetism and spin transport,
- mesoscopic systems and quantum phenomena in nanostructures,
- self-organization of molecules on surfaces,
- and the general properties of metallic systems at low and very low temperatures.

The WMI also conducts **applied research** in the fields of

- solid state based quantum information processing systems,
- superconducting and spintronic devices,
- oxide electronics,
- and the development of low and ultra low temperature systems and techniques.

With respect to **materials science** the research program is focused on

- the synthesis of superconducting and magnetic materials,
- the single crystals growth of oxide materials,
- the epitaxial growth of complex oxide heterostructures,
- and the growth of self-organized molecular ad-layers.

With the installation of a new helium liquefier and a new low temperature Scanning Tunneling Microscope, the experimental facilities of the WMI could be further renewed and expanded in 2004. Furthermore, the experimental facilities for the study of superconducting quantum

bits have been extended in 2004 to allow for high frequency characterization of such devices down to the mK regime. The new helium liquefaction system not only provides the basis for the experimental low temperature research at the WMI but also for more than 20 other research groups at both Munich universities. With the installation of the new low temperature scanning probe system the WMI has extended its characterization techniques by a powerful new method that perfectly fits to the already existing techniques and materials oriented work. The combination of the broad expertise of the WMI groups in low temperature techniques, nanotechnology as well as superconducting and magnetic materials with the competence of the new scanning probe division is expected to stimulate our future research activities.

The various research projects of the WMI have been successfully continued in 2004. In particular, the research work within the SFB 631 on ***Solid State Based Quantum Information Processing: Physical Concepts and Materials Aspects***, which has been installed by the German Science Foundation in July 2003, has been successfully started (see `http://www.wmi.badw-muenchen.de/SFB631`). The WMI also took the leadership in setting up the new Research Unit FOR 538 on ***High Temperature Superconductivity***, which has been installed by the German Science Foundation effective in April 2004 (see `http://www.wmi.badw-muenchen.de/FG538`). The research program of FOR 538 is subdivided into seven interlinked projects located at the WMI (3), as well as at the University of Würzburg (1), the Leibniz Institute for Solid State and Materials Research at Dresden (1), and the Max-Planck-Institute for Solid State Research at Stuttgart (2). The main purpose is to arrive at a detailed understanding of the phase diagram of copper-oxygen systems by a coordinated research effort. Both for the SFB 631 and the FOR 538 the spokesperson and coordinator of the coordinated research programs are members of the WMI. Beyond the SFB 631 and the FOR 538, the WMI has started a new research project on ***New Functional Thin Film Systems Based on Artificial Heterostructures of Transition Metal Oxides*** within the Priority Programme 1157 of the DFG on ***Integrated Electroceramic Functional Systems***. Finally, a new DFG project on the ***Development of a High Precision Rotation Sensor Based on Superfluid*** ^{3}***He*** has been started in 2004.

In 2004, the WMI was organizing several international conferences and workshops. The ***International Workshop on Fluctuating Charge Order in High Temperature Superconductors*** in May was followed by the ***International Workshop on Solid State Based Quantum Information (QIP 2004)*** at Herrsching from September 13 – 17, 2004. During this workshop the results obtained within SFB 631 have been discussed with leading international experts. The WMI also was chairing the ***NATO Advanced Research Workshop on Nanoscale Devices - Fundamentals and Applications (NDFA-2004)*** held at Kishinev, Moldova, from September 18 – 22, 2004. Finally, the WMI was organizing the ***International Workshop on Ordering Phenomena in Cuprate Superconductors*** from November 4 – 5, 2004, at the Munich Residence.

The research at the WMI has been very successful in 2004 as demonstrated by a large number of scientific papers, invited presentations at national and international conferences as well as seminar talks and colloquia. Throughout 2004, an average of 13 scientific staff members, 18 members of the administrative and technical staff, 16 doctorate candidates, 20 diploma/master students as well as a large number of short and long–term guests belonged to the institute. Of course, also in 2004 the scientific productivity of the WMI would not have been possible without the collaborative atmosphere, the high motivation of our research and technical staff and the support of various funding agencies. In particular, we acknowledge the financial support from the Bavarian Academy of Sciences, the German Science Foundation, the Bavarian Ministry for Science and Arts, the BMBF and the EU. Unfortunately, in the same way as in 2003 the WMI has to suffer a cut-back of its annual total budget by more than 15% in 2004. Since it is impossible to reduce the running costs of the institute (electricity, heating, water etc.) by this

amount, a much larger reduction of the "research budget" was caused. This reduction could be partly compensated by the successful acquisition of additional research money from various funding agencies. However, on the long term similar cut-backs as in the years 2002 – 2004 will cause severe problems with respect to the apparative and technological basis of the WMI and in turn its competitiveness in acquiring external research projects.

This Annual Report gives an overview on the scientific results of the WMI, which in many cases have been obtained within joint national and international research projects and in close collaboration with international guests. Our 2004 Annual Report is intended to provide an overview on our work to our friends and partners in research and industry and thereby to intensify our numerous collaborations. I would be particularly pleased, if the report would stimulate new collaborations. In order to be useful also for our numerous international partners the report is written in English.

I finally would like to thank all the colleagues, guests, students, post–docs and cooperating partners, who contributed to the success of our work within the last year, and last but not least all our friends and sponsors for their interest, trust and continuous support.

Rudolf Gross

Garching, December 2004

Contents

Preface **1**

The Walther–Meißner–Institute **7**

Reports: **9**

Basic Research **9**

The New Research Unit 538:
Doping Dependence of Phase Transitions and Ordering Phenomena in Cuprate Superconductors 9

New Low Temperature Scanning Probe Division at the WMI 12

Hall effect, magnetization, and conductivity of Fe_3O_4 epitaxial thin films 14

Anisotropic transport behavior in Sr_2CrWO_6 thin films 18

Magnetic polarization of W in the double perovskites Sr_2CrWO_6 and Ca_2CrWO_6 . . . 21

Angle-dependent magnetoresistance probing the electronic state of the charge-density-wave organic conductor α-(BEDT-TTF)$_2$KHg(SCN)$_4$ 24

Magnetization Studies of the Nuclear Spin Ordered Phases of Solid ^{3}He in Silver Sinters 27

Impurity–limited transport in unconventional superconductors 31

Doping and lattice effects in the half-metallic double perovskite Sr_2CrWO_6 33

Effect of rare earth ion substitution on the magnetic and transport properties of $Pr_{0.7}RE_{0.04}Sr_{0.26}MnO_3$ (RE = Er^{3+}, Tb^{3+}, Ho^{3+}) 37

Application Oriented Basic Research **42**

The Persistent-Current Quantum-Bit in a Microwave Cavity 42

TMR effect and spin polarization of thin films of magnetite (Fe_3O_4) 50

Ferromagnetism in Mn-doped ZnO due to impurity bands 56

Ferromagnetism in thin films of Co-doped ZnO 59

Dynamics of Inter-Layer Water Molecules in Graphite Oxide 62

Materials and Experimental Techniques **64**

Single crystal growth of cuprate superconductors 64

Superconducting qubits: setup for experimental characterization 67

Automatization of the Pulsed Laser Deposition Process 71

Epitaxial growth of electron doped double perovskites $La_xSr_{2-x}CrWO_6$ 73

Cryogen-free dilution refrigerator precooled by pulse-tube cooler with non-magnetic regenerator 76

The New Helium-Liquifier at the WMI 80

Experimental Facilities **83**

Publications **95**

Theses, Appointments, Awards **99**

Research Projects and Cooperations **101**

Invited Conference Talks and Seminar Lectures **109**

Seminars, Courses, Lectures and other Scientific Activities **113**

Staff of the Walther-Meissner-Institute **121**

Guest Researchers **123**

Commission for Low Temperature Physics **125**

The Walther–Meißner–Institute

The Walther–Meißner–Institute for Low Temperature Research (WMI) is operated by the Commission for Low Temperature Research of the Bavarian Academy of Sciences (BAdW). The Commissions (Research Groups) of the Bavarian Academy are set up in order to carry out long–term projects, which are too ambitious for the lifetime or capacity of any single researcher, or which require the collaboration of specialists in various disciplines. At present, the Bavarian Academy of Sciences consists of 36 Commissions with more than 300 employees. The WMI also is the host institute of the chair for Technical Physics (E 23) of the Technical University of Munich. The director of the WMI at the same time is ordinarius at the Faculty of Physics of the Technical University of Munich.

The research at the Walther–Meißner–Institute is focused on low temperature physics (see reports below). The WMI also develops systems and techniques for low and ultra–low temperature experiments. As typical examples we mention a dry mK-system that can be operated without liquid helium by using a pulse-tube refrigerator for precooling, a nuclear demagnetization cryostat for temperature down to below 100 μK, or very flexible dilution refrigerator inserts for temperatures down to about 20 mK fitting into a 2 inch bore. These systems have been engineered and fabricated at the WMI. Within the last years, several dilution refrigerators have been provided to other research groups for various low temperature experiments. The WMI also operates a helium liquifier with a capacity of more than 150.000 liters per year and supplies both Munich universities with liquid helium. To optimize the transfer of liquid helium into transport containers the WMI has developed a pumping system for liquid helium that is commercialized in collaboration with a company.

The individual research groups of the WMI offer a wide range of attractive research opportunities for diploma (graduate) students, PhD students and postdoctoral fellows. The WMI is equipped with state of the art facilities for the preparation and characterization of superconducting and magnetic materials as well as for various low and ultra–low temperature experiments. The main experimental and technological resources of the WMI are listed in the following.

Materials Preparation and Fabrication of Nanostructures

- Laser Molecular Beam Epitaxy system for oxide heterostructures (equipped with in–situ RHEED, AFM/STM system, atomic oxygen source, laser heating system, metallization)
- UHV magnetron sputtering systems for metals (e.g. Nb, Al, NiPd, ...)
- magnetron sputtering system for oxide heteroepitaxy (equipped with four sputtering guns and an oxygen ion gun)
- ion beam sputtering system
- UHV metallization system (equipped with e–gun and thermal evaporators)
- ion beam etching system equipped with a LN_2 cooled sample holder
- polishing machine for substrate preparation
- ultrasonic bonding machine
- 50 m^2 class 1000 clean room facility
- optical lithography (Süss maskaligner MJB 3, projection lithography)
- electron beam lithography (based on Philips XL 30 SFEG scanning electron microscope and Raith Elphy Plus lithography system including a laser stage)
- four-mirror image furnace for crystal growth

Characterization

- 2–circle x–ray diffractometer (Bruker D8 Advance, sample temperature up to 1 600°C)
- high resolution 4–circle x–ray diffractometer (Bruker D8 Discover)
- scanning electron microscope with EDX analysis
- UHV room temperature AFM/STM system
- 2048 u high resolution mass spectrometer (Fa. Pfeiffer, cross beam ion source, SEM)
- Low Energy Electron Diffraction (SPECTA-LEED, Fa. Omicron)
- two Raman spectroscopy systems (1.5 to 300 K, in-situ sample preparation)
- SQUID magnetometer (1.5 to 700 K, up to 7 Tesla)
- several high field magnet systems (up to 17 Tesla)
- experimental set–ups for the measurement of noise including low noise SQUID amplifiers and signal analyzers
- high frequency network analyzer (up to 40 GHz) for the determination of high frequency parameters

Low temperature systems and techniques

- 5 K-Scanning Tunnelling Microscope (low temperature STM, Fa. Omicron)
- several ^{3}He/^{4}He dilution refrigerator inserts for temperatures down to 10 mK
- "dry" mK-cooler based on a dilution refrigerator with pulse-tube precooling
- ultra–low temperature facility for temperatures down to below 100 μK based on a nuclear demagnetization cryostat
- experimental set–ups for the measurement of specific heat, magnetization, thermal expansion as well as electrical and thermal transport properties as a function of temperature, magnetic field and pressure

The New DFG Research Unit 538: Doping Dependence of Phase Transitions and Ordering Phenomena in Cuprate Superconductors

R. Hackl, A. Erb, R. Gross [1]

In February 2004 the German Science Foundation (Deutsche Forschungsgemeinschaft: DFG) has established the Research Unit 538 (Forschergruppe 538: FOR 538) which is devoted to the study of high-temperature superconductors. The main focus is directed towards the *Doping Dependence of Phase Transitions and Ordering Phenomena* (Fig. 1).

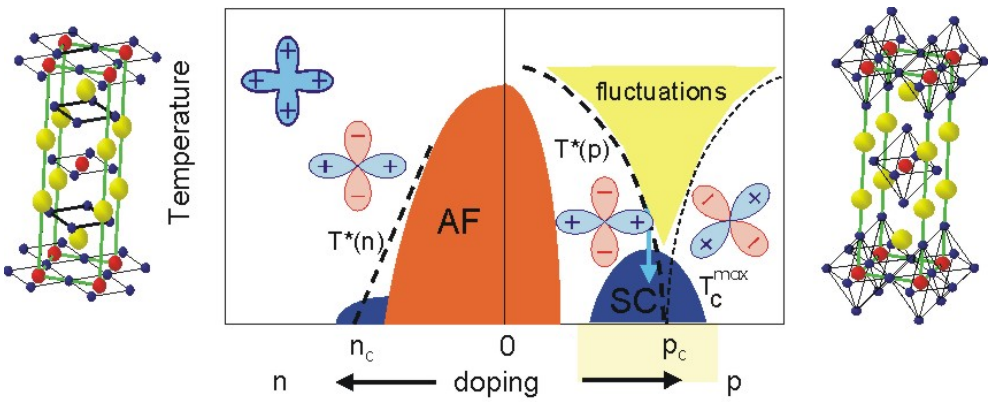

Figure 1: Typical crystal structures and global phase diagram of electron (n) and hole (p) doped copper-oxygen systems. The antiferromagnetic and the superconducting phases are labeled by AF and SC, respectively. T^* is the crossover temperature to the so-called pseudogap state. Possible symmetries for the superconducting gap at different doping levels are indicated symbolically.

The purpose is to arrive at a detailed understanding of the phase diagram of copper-oxygen systems with superconducting transition temperatures T_c up to 160 K and to disentangle general and sample related properties. As an example, while the copper-oxygen planes as the relevant structural units (see Fig. 1) and henceforth the electronic structure is essentially the same in all material classes there is a difference by an order of magnitude in the maximal T_c.

The Walther-Meißner-Institute (WMI) initiated this activity and coordinates the research program. The spokesperson and coordinator of the Unit is at the WMI. The research program is subdivided into seven interlinked projects located at the WMI and the Technical University Munich (3), as well as at the University of Würzburg (1), the Leibniz Institute for Solid State and Materials Research at Dresden (1), and at the Max-Planck-Institute for Solid State Research at Stuttgart (2) (see Fig. 2). In the meantime, two projects partially moved to Austria (Vienna University of Technology and Graz University of Technology) due to recent appointments of group leaders at Austrian universities.

The Research Unit includes a theory project, sample preparation and five spectroscopic methods, i.e. angle-resolved photoemission (ARPES), neutron and Raman scattering, optical conductivity and electron tunneling. The combination of single and two-particle methods allows a better understanding of the relevant interactions in highly correlated systems. One of the main innovations of the work is the use of a common basis of samples for all spectroscopic methods and the simultaneous analysis of the results (see Fig. 3).

The main questions to be addressed within FOR 538 include:

[1] This work is supported by the DFG.

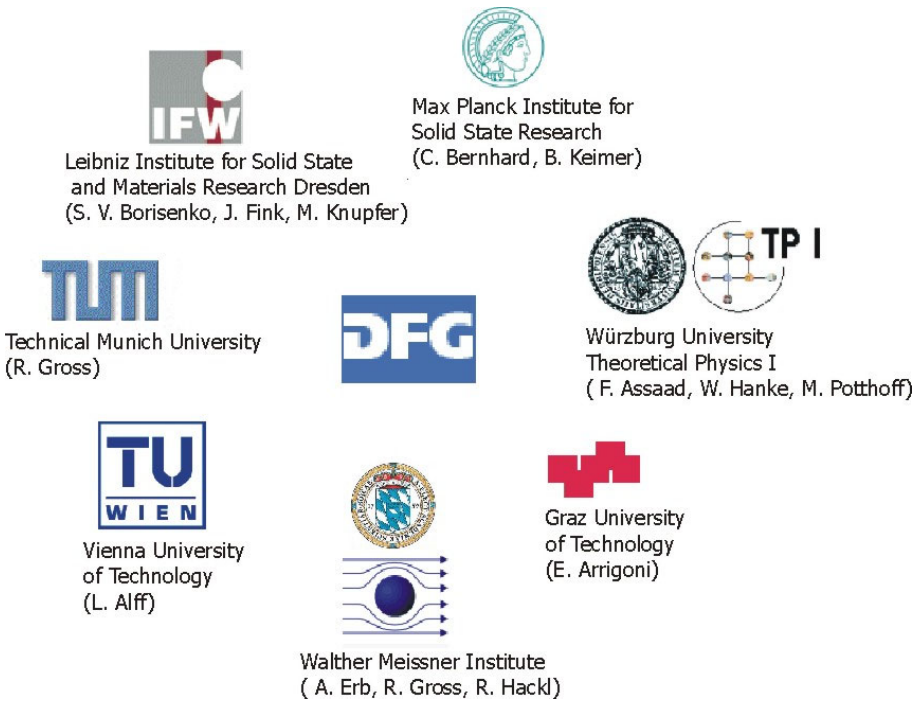

Figure 2: Institutions participating in Research Unit 538.

- Properties of electron- and hole-doped cuprates as a function of carrier concentration
- Separation of general and sample-specific properties
- Study of the various phase and metal-insulator transitions
- Charge and spin ordering
- Competing order
- Quantum criticality
- Study of the interactions relevant for superconductivity

In order to find answers to these questions coordinated activities became increasingly important after almost two decades of intense work worldwide. Therefore, the DFG decided to support this coordinated research in spite of the substantial knowledge already accumulated. The main purpose is to *combine* activities devoted to a better understanding of a rather complicated subject. In addition, young scientists should be attracted and get in touch with interesting open problems of modern solid state physics. The DFG provides also funding for national and international workshops to communicate the results. In 2004, there were already two meetings. The first one (May 27/28) took place at the WMI, the second one (November 4/5), supported generously by the Bavarian Academy of Sciences, was organized at the Munich Residence.

Three out of the seven projects of FOR 538 are located at the WMI. In addition, there is a separate coordination project which is mainly to foster communication. The projects at the WMI (TP 3–5) are devoted to sample preparation and basic characterization, tunneling studies of the symmetry of the superconducting energy gap and Raman spectroscopy of anisotropic electron properties.

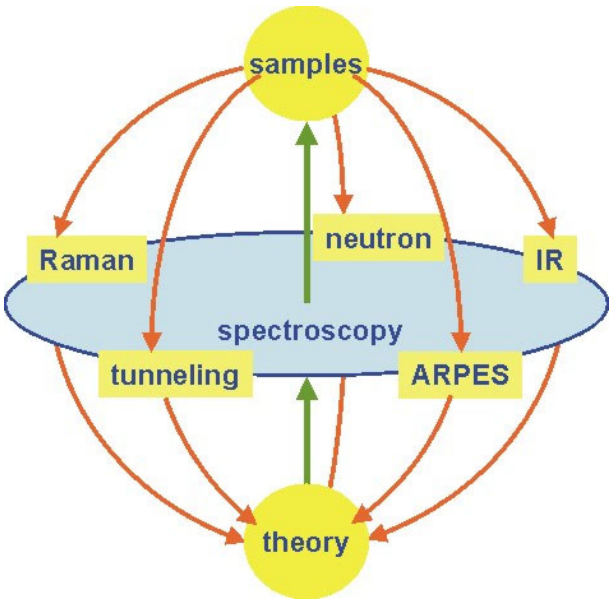

Figure 3: Interactive research within FOR 538. The samples for all experiments are prepared and pre-characterized in one place. The experimental results will be analyzed and interpreted simultaneously. There is a feedback process for reiteration and refinement.

For the preparative part (TP 3) the WMI succeeded to install a new mirror furnace and several modern facilities for characterization. The main support is allocated to starting materials of high purity. In addition to ultra-high-purity single crystal of $(Y_{1-y}Ca_y)Ba_2Cu_3O_{6+x}$ the preparation of Bi-based crystals ($Bi_2Sr_2CaCu_2O_{8+ffi}$) with various dopants (Pb, Dy, Ni, Y, Zn) has been optimized until now. The growth of $La_{2-x}Sr_xCuO_4$ and $(RE)_{2-x}Ce_xCuO_4$ (RE = La, Nd, Pr) is in progress.

The purpose of the tunneling project (TP 4) is to get more insight into the pseudogap state and to develop an improved understanding of the the symmetry of the order parameter as a function of doping. To this end the tunneling conductance will be measured above and below T_c partially in high magnetic fields. As to the symmetry of the order parameter the zero-bias anomaly allows for phase sensitivity. This activity includes the preparation of thin-film samples of $(RE)_{2-x}Ce_xCuO_4$ (in collaboration with Michio Naito, NTT). The group leader (L. Alff) relocated part of the project to Vienna, where he was appointed professor in October 2004.

Raman scattering from conduction electrons (TP 5) supplements infrared studies of the optical conductivity (Infrared ellipsometry, TP 7, Stuttgart) since momentum resolution can be achieved. At low energies the **k**-dependence of both normal and superconducting electrons will be studied at all doping levels available. One of the main objectives at present is the relation of charge and/or spin ordering and pairing interactions. At high energies the transfers of spectral weight will be investigated. To facilitate these measurements a new CCD detector with substantially improved specifications was installed.

New Low Temperature Scanning Probe Division at the WMI

B. Hermann [1]

Towards the end of the year 2004, the acceptance procedure for the main apparatus of the new WMI division on scanning probe microscopy was finished and we could take over the low temperature (5 K) scanning tunneling microscope with preparation chamber, low energy electron diffraction (LEED) and mass spectrometer analysis.

Why Scanning Probe Microscopy at Low Temperatures

At low temperatures the mobility of single atoms, molecules, or weakly bound clusters on a surface is strongly reduced allowing a more detailed analysis of the chemical and physical interactions as well as the diffusive behavior. Most quantum phenomena, like superconductivity, only occur at temperatures far below ambient. Additionally, it is possible to investigate temperature dependent 2-D ordering phenomena as phase changes or e.g. freezing of rotations. On top of that the performance of the equipment is considerably improved concerning instrument noise and thermal drift. Following, the low temperature scanning tunneling microscope (STM) is described as well as other analytic and preparation possibilities.

Low Temperature STM

At the Walther-Meißner-Institute now a low temperature scanning tunneling microscope (top picture) is operated for the investigation of low dimensional systems such as self-organized molecules, superconductor, magnetic and heterostructure surfaces. The STM has been designed to meet the special requirements of a wide variety of collaborations. It comprises:

- in-situ sample and tip exchange.
- optimal vibration isolation ensured by a spring suspension system with eddy current damping and pneumatic damping legs.
- variable temperatures from 5 K (pumped 2 K) up to room temperature ($\sim$ 300 K).
- fast system cool-down (5 K within $\sim$ 6 hours).
- fast sample cool-down (5 K within $\sim$ 2 hours).
- UHV condition.
- optical access.
- four terminal transport measurements.
- RHK open scan electronic system.

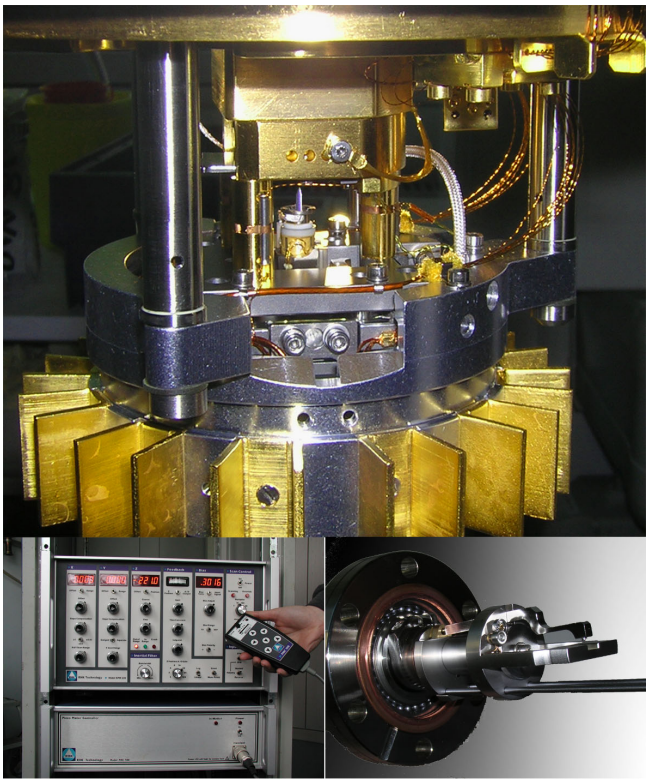

Figure 1: Top: low temperature STM, bottom left: scan electronics , bottom right: manipulator

[1]The new research equipment is supported by the Center for Nano Science (CeNS), Ludwig-Maximilians-University and the Bavarian State as well as the German State Government. The laboratory infrastructure comes from the WMI. The ongoing work in Basel is supported through the Swiss National Science Program NRP 47.

Preparation and Further Analysis
Docked to the analysis chamber containing the Omicron-STM (top picture: the tower to the left) is a preparation chamber (top picture: to the right and bottom picture). Inside this separate chamber clean single crystalline substrates can be prepared by ion-sputtering and subsequent thermal annealing, which is controlled by a three grid LEED (bottom picture) in a vacuum of 10^{-11} mbar.
The surface ordering of (reconstructed) substrate/single crystal surfaces or molecular ad-layers can be analyzed by low energy electron diffraction (LEED).
Samples can be additionally characterized by desorption spectroscopy with a quadrupole mass spectrometer. The desorbing molecules are ionized in a crossbeam ion source and accelerated in the quadrupole mass spectrometer, which either uses a Faraday cup or secondary electron multiplier (SEM) as detector with a mass resolution up to 2048 amu. The preparation facilities allow a direct current and indirect heating of the sample up to 800°C and sample cooling down to 50 K on the manipulator (top picture: far right).
Multiple additional vacuum ports allow further extensions in the future.

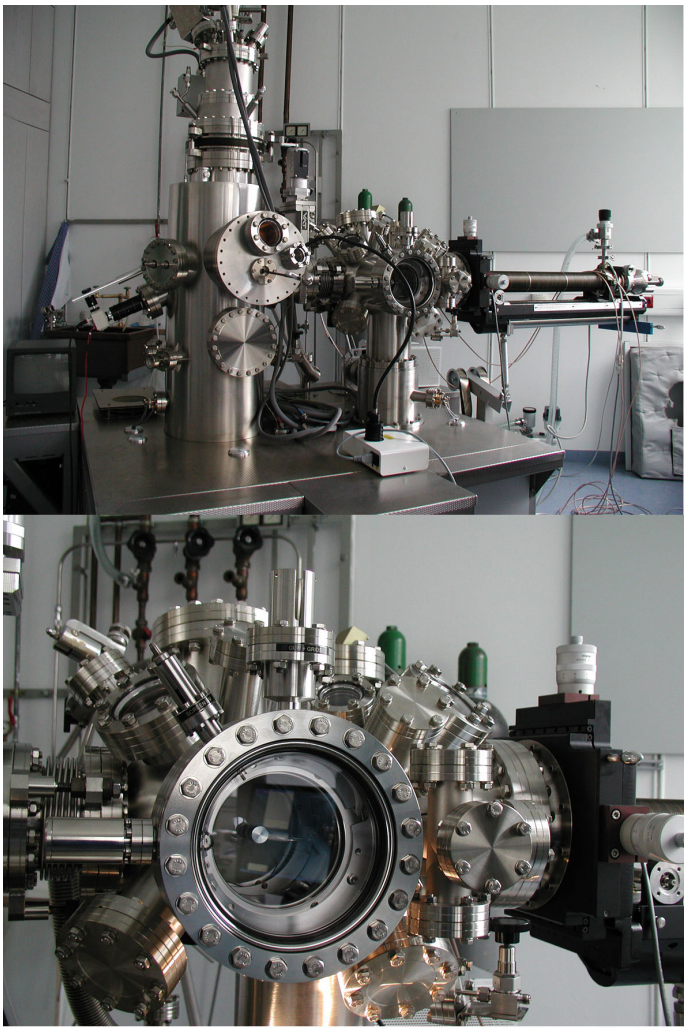

Figure 2: top: entire setup viewed from the main operation side, bottom: LEED system enlarged.

Ongoing Research

While the new lab at the WMI was built up, a collaborate research effort continued in the Basel facilities (instruments kindly supplied by H.-J. Güntherodt) within the framework of the NRP47 Swiss National Program on "Supramolecular Functional Materials". We found that the two-dimensional structure formed from self-assembling, weakly bound metallosupramolecular squares observed by STM depends very much on the nature of the surface [2]. The near atomic resolution on smaller Fréchet-type dendrons allowed assigning molecular conformers, which spontaneously and rapidly form molecular domains under ambient conditions [1]. Within a molecular domain, only one conformer is present and domains of different conformers are observed side by side. No preference for one conformer was observed.

References

[1] Constable C., Hermann B.A., Housecroft C., Merz L., Scherer L., Chemical Communication 928-929, (2004).
[2] Safarowski C., Merz L., Rang A., Broekmann P., Hermann B.A., Schalley C.A., Angewandte Chemie **116**, 1311-1314 (2004).

Hall Effect, Magnetization, and Electrical Transport Properties of Fe_3O_4 Epitaxial Thin Films

D. Reisinger, P. Majewski, S. Qureshi, E. Menzel, A. Erb, L. Alff, M. Opel, and R. Gross [1]

Half-metallic materials with 100% spin polarization of the charge carriers at the Fermi level are under intensive investigation due to their potential application in spintronics. One promising candidate with a theoretically predicted half-metallicity and also a high Curie temperature of $T_C \simeq 860$K is magnetite (Fe_3O_4) [1]. Moreover, magnetite has a low magneto-crystalline anisotropy. For the use in spintronic devices, the growth of high quality thin films is required. Recently, Fe_3O_4 thin films have been grown by different techniques including sputtering, molecular beam epitaxy, and pulsed laser deposition [2, 3, 4] on various substrates (MgO, $MgAl_2O_4$, $SrTiO_3$, sapphire, and Si). Here, we report on electrical transport, magnetization, and Hall effect measurements in high quality epitaxial magnetite thin films grown on MgO and Si substrates by pulsed laser deposition [5]. The key result is that for the high quality epitaxial films the same properties can be achieved as for bulk samples [6].

The 40 to 50 nm thick magnetite thin films were deposited from a stoichiometric target by pulsed laser deposition [7] at a substrate temperature of typically 340°C on MgO(001) or Si(001) substrates. In-situ reflection high energy electron diffraction (RHEED) was used to monitor the block-by-block growth mode of magnetite. Four RHEED intensity oscillations have been observed during the growth of a single unit cell of Fe_3O_4 corresponding to four charge neutral blocks of composition $Fe(A)_2^{3+}Fe(B)_2^{3+}Fe(B)_2^{2+}O_8^{2-}$ [8]. Here, A and B refer to the tetrahedral and octahedral sites of the inverse spinel structure, respectively, where the B site is equally occupied by Fe^{3+} and Fe^{2+} ions. A more detailed discussion of the thin film growth process on Si, which involves a buffer layer system, is given in [4]. In order to prevent surface oxidation, the magnetite films were covered by an about 10 nm thick MgO cap layer, grown also at 340°C. X-ray analysis gives a *c*-axis lattice constant of 8.39 Å and a typical mosaic spread of 0.02° for MgO substrates. No impurity phases could be observed in the diffraction pattern. The rms surface roughness was determined by AFM. Typical values averaged over an area of 1 mm^2 ranged between 2 and 5 Å. The film thickness was evaluated by counting the RHEED intensity oscillations and also was verified by x-ray reflectometry.

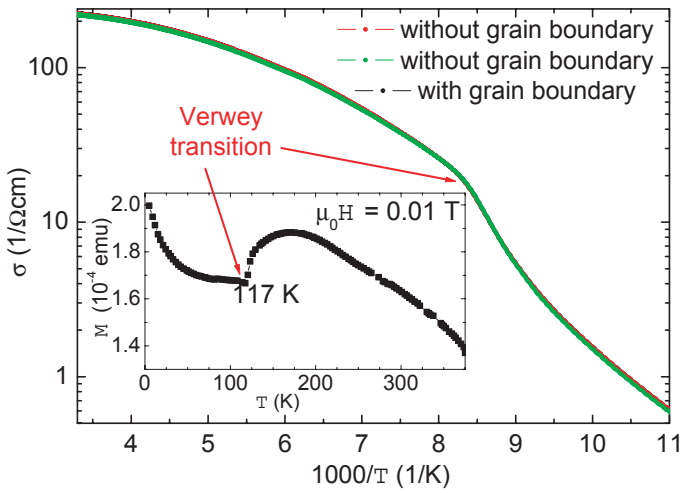

Figure 1: Electrical conductivity σ of a 45-nm-thick epitaxial Fe_3O_4 film grown on a MgO bicrystal plotted vs $1/T$. The curves for bridges with and without grain boundary are indistinguishable. The Verwey transition around 120 K can be best seen in the inset, where the magnetic moment measured in a field of 100 Oe is plotted vs. temperature.

In Fig. 1, the electrical conductivity σ of an epitaxial Fe_3O_4 thin film grown on a MgO(001) symmetrically [001] tilt bicrystal substrate with a misorientation angle of 24.8° is plotted versus $1/T$. First, it is evident that the $\sigma(T)$ curve obtained for a bridge crossing the grain boundary

[1] This work is supported by the BMBF (project no. 13N8279).

is the same as for bridges without grain boundary. That means that the grain boundary resistance is much smaller than the resistance of the adjacent film part of the bridge. A similar effect has been observed for grain boundaries in doped manganites, where only a high-temperature annealing process in oxygen atmosphere produces a grain boundary with sufficiently high resistance [9]. Second, the absolute value of the conductivity of about 225 $\Omega^{-1}\mathrm{cm}^{-1}$ at room temperature is comparable to the best values of about 250 $\Omega^{-1}\mathrm{cm}^{-1}$ reported for bulk samples [10] and of about 190 $\Omega^{-1}\mathrm{cm}^{-1}$ reported for films of the same thickness [11]. Third, the Verwey transition at $T_V \simeq 117$ K is smeared out in the $\sigma(T)$ curve of the film as compared to single crystals, where a sharp jump is observed. We note that also the magnetic moment (see inset of Fig. 1) gradually decreases with decreasing temperature starting already above 150 K. Again, this is in contrast to bulk samples where a sharp jump is observed at T_V. However, the data show a clear kink structure at $T_V = 117$ K, which is also reported in literature [13]. The physics of this Verwey transition and its relation to a possible charge/orbital order is still under discussion.

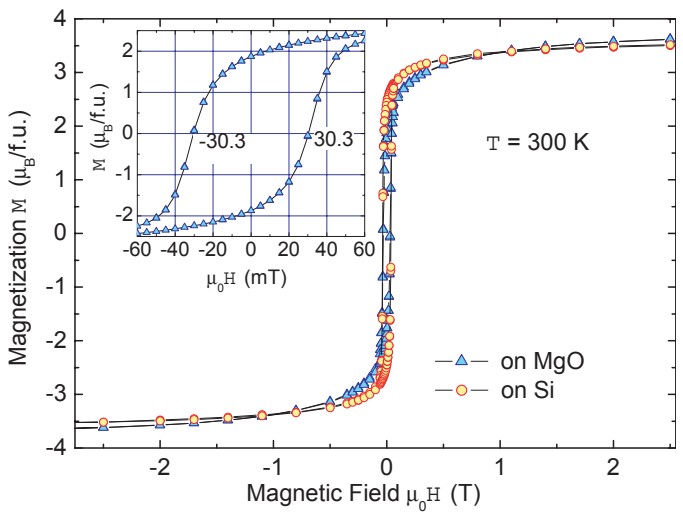

Figure 2: Magnetization M versus applied magnetic field H at 300 K for epitaxial Fe_3O_4 films grown on MgO and Si substrates. The field was applied in-plane. The inset shows a blow-up of the low field part of the hysteresis curve for the film grown on MgO.

Fig. 2 shows the magnetization versus applied field dependence for Fe_3O_4 thin films grown on MgO and Si [4]. The diamagnetic signal of the substrate, which was determined by a linear fit of the high field data between 5 and 7 T has been subtracted. At 300 K, the saturation magnetization M_S is about 3.6 and 3.5 μ_B/formula unit for the film grown on MgO and Si, respectively. At 150 K, this value increases to 3.8 μ_B/f.u.. The coercive field is about 30 mT at room temperature. The magnetization data show that the M_S values obtained for our epitaxial films with a thickness ranging between 40 and 50 nm are close to the theoretically expected bulk value of 4 μ_B/f.u.. Our M_S is among the highest values reported for thin films so far [2, 12]. We also note that our room temperature value of 453 emu/cm^3 is close to the value of 471 emu/cm^3 reported for a single crystal [14], i.e. for our thin films about 96% of the bulk value is reached. We attribute the high M_S values from our films to their good structural properties and to the fact that surface oxidation is prevented using a MgO cap layer. Due to the good lattice match between the film and the substrate (for the Si substrate the lattice mismatch is relaxed using a TiN/MgO double buffer layer system [4]) also strain effects play no important role.

In Fig. 3, the Hall resistivity is plotted versus the applied magnetic field at $T = 290$ K. It is well known that in nonmagnetic metals the regular Hall current arises when electrons moving in crossed electric (**E**) and magnetic fields (**H**) are deflected by the Lorentz force. However, in a ferromagnet subject to **E** alone, an anomalous Hall current appears transverse to **E**. This anomalous Hall effect (AHE) in itinerant ferromagnets is still discussed controversially. In an AHE experiment the observed Hall resistivity ρ_H comprises two terms,

$$\rho_H = R_0 \mu_0 H + R_A \mu_0 M \qquad (1)$$

where R_0 and R_A are the normal and anomalous Hall coefficient, respectively, and M is the sample magnetization. It is evident that at sufficiently high H the sample magnetization saturates and the change of ρ_H is only due to the regular Hall effect. From the linear high field dependence of the Hall effect data we derive $R_0 \simeq -2.12 \cdot 10^{-9} \mathrm{m}^3/\mathrm{C}$ at 300 K. Using the relation $R_0 = 1/en$, we obtain an electron density of $n = 2.95 \cdot 10^{21}$ cm^{-3}. With the density $\rho = 5.185$ g/cm^3 of magnetite, we obtain the number of electrons per formula unit as 0.22. This value is comparable to that observed in bulk single crystals [6]. The negative sign of the regular Hall coefficient suggests electron conduction. We also note that R_0 is slightly larger at 160 K as compared to 300 K due to the increase in the Hall mobility. The Hall mobility μ_H is given by the product of the regular Hall coefficient and the conductivity. At 300 K, we obtain $\mu_H = 0.48$ cm^2/Vs. The anomalous Hall coefficient at 300 K is determined to $R_A \simeq -2.5 \cdot 10^{-7} \mathrm{m}^3/\mathrm{As}$ using the measured $M_S = 3.6\ \mu_B$/f.u. We note that R_A shows a positive sign for the half-metallic double perovskite Sr_2FeMoO_6, while R_0 is negative [9]. This is in contrast to magnetite, where both R_0 and R_A have negative sign. Within a simple model the different signs of R_A for different materials can be understood in terms of asymmetric scattering due to different densities of states available for positive and negative orbital orientations [15].

Discussing σ and n we can state that in a simple physical picture one would expect that the minority spin electron that is shared by the two octahedrally coordinated B sites gives rise to electronic conductivity above the Verwey transition. Below the Verwey transition, charge ordering of the B-site ions leads to an insulating state. The observation that only 0.22 electrons per formula unit contribute to the conductivity could be explained by localization effects due to electronic correlations. Recently, in an ab-initio study of charge order in magnetite the local spin density has been calculated as a function of symmetry (or structural distortion). This calculation yields 100% spin polarization, a total spin magnetic moment of about 4.0 μ_B and about 0.24 electronic states per formula unit at the Fermi level [16]. Although these values have been calculated for the charge ordered ground state, they are remarkably consistent with the results obtained in our study above the Verwey transition.

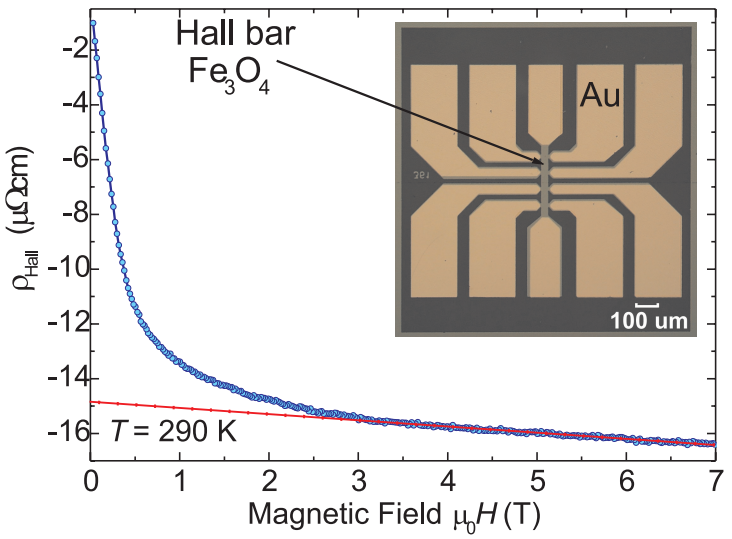

Figure 3: Hall resistivity ρ_H for a Fe_3O_4 thin film grown on MgO(001). The red line is a fit to the high field data where the magnetization saturates. The inset shows an optical micrograph of the Hall bar geometry. At the Au contact pad areas the MgO cap layer was removed by ion-beam etching prior to Au deposition.

In summary, we have grown high quality epitaxial thin films of magnetite with properties comparable to those of best bulk samples. We report Hall effect measurements for thin films, indicating that only 0.22 electrons per formula unit contribute to the electrical conductivity [5].

References

[1] Z. Zhang and S. Satpathy, Phys. Rev. B **44**, 13319 (1991).
[2] D.T. Margulies, F.T. Parker, F.E. Spada, R.S. Goldman, J. Li, R. Sinclair, and A.E. Berkowitz, Phys. Rev. B **53**, 9175 (1996).

[3] F.C. Voogt, T.T.M. Palstra, L. Niesen, O.C. Rogojanu, M.A. James, and T. Hibma, Phys. Rev. B **57**, R8107 (1998).
[4] D. Reisinger, M. Schonecke, T. Brenninger, M. Opel, A. Erb, L. Alff, and R. Gross, J. Appl. Phys. **94**, 1857 (2003).
[5] D. Reisinger, P. Majewski, M. Opel, L. Alff, and R. Gross, Appl. Phys. Lett. **85**, 4980 (2004).
[6] J. M. Lavine, Phys. Rev. 114, 482 (1959).
[7] R. Gross, J. Klein, B. Wiedenhorst, C. Höfener, U. Schoop, J. B. Philipp, M. Schonecke, F. Herbstritt, L. Alff, Yafeng Lu, A. Marx, S. Schymon, S. Thienhaus, W. Mader, in *Superconducting and Related Oxides: Physics and Nanoengineering IV*, D. Pavuna and I. Bosovic eds., SPIE Conf. Proc. **Vol. 4058** (2000), pp. 278–294.
[8] D. Reisinger, B. Blass, J. Klein, J. B. Philipp, M. Schonecke, A. Erb, L. Alff, and R. Gross, Appl. Phys. A: Mater. Sci. Process. **77**, 619 (2003).
[9] J. B. Philipp, C. Höfener, S. Thienhaus, J. Klein, L. Alff, and R. Gross, Phys. Rev. B 62, R9248 (2000).
[10] B. A. Calhoun, Phys. Rev. 94, 1577 (1954).
[11] W. Eerenstein, T. T. M. Palstra, T. Hibma, and S. Celotto, Phys. Rev. B 66, 201101 (R) (2002).
[12] S. Soeya, J. Hayakawa, H. Takahashi, K. Ito, C. Yamamoto, A. Kida, H. Asano, and M. Matsui, Appl. Phys. Lett. 80, 823 (2002).
[13] M. Ziese, R. Höhne, N. H. Hong, J. Dienelt, K. Zimmer, and P. Esquinazi, J. Magn. Magn. Mater. 242, 450 (2002).
[14] Magnetic and Other Properties of Oxides and Related Compounds, edited by K.-H. Hellwege and A. M. Hellwege, Landolt-Börnstein, New Series, Group III, Vol. 4, Pt. b (Springer, Berlin, 1970).
[15] A. Fert and O. Jaoul, Phys. Rev. Lett. 28, 303 (1972).
[16] Z. Szotek, W. M. Temmermann, A. Svane, L. Petit, G. M. Stocks, and H. Winter, Phys. Rev. B 68, 054415 (2003).

Anisotropic Transport Behavior in Epitaxial Sr_2CrWO_6 Thin Films

A. Boger, P. Majewski, S. Geprägs, A. Erb, M. Opel, L. Alff and R. Gross [1]

The double perovskite Sr_2CrWO_6 (see Fig. 1) is predicted to show a high spin polarization of 100% [1]. Furthermore, in polycrystalline samples a high Curie temperature of more than 420 K was found [2]. This combination makes Sr_2CrWO_6 interesting for applications in spinelectronics. On the other hand, the material can be grown epitaxially on $SrTiO_3$ substrates giving rise to thin film of high crystalline quality [3]. Due to the non-vanishing lattice mismatch between the film and the substrate the compressive strain causes a reduction of the *in-plane* lattice parameters (a, b), while the c parameter is expanded. To get information on the effect of the biaxial strain on the magnetotransport properties, the in-plane and out-of-plane current-voltage characteristics (IVCs) have been studied.

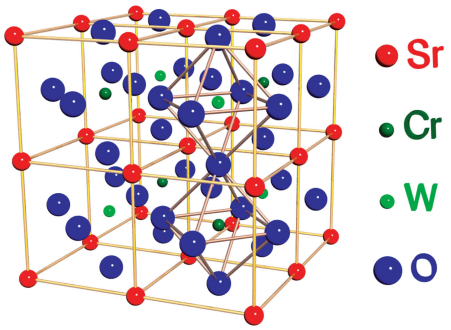

Figure 1: Cubic unit cell of Sr_2CrWO_6. Each Cr^{3+} and W^{5+} ion is surrounded by an octahedron of O^{2-}.

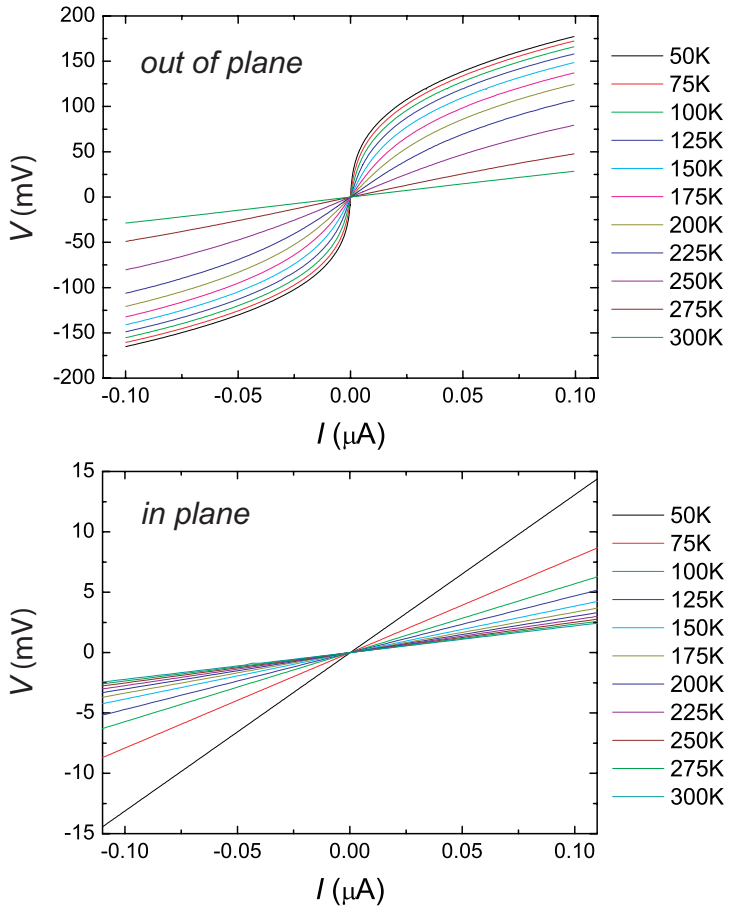

Figure 2: IVCs obtained for Sr_2CrWO_6 thin films with the current direction *out-of-plane* (top) and *in-plane* (bottom) for temperatures between 50 K and 300 K.

Here, we report on the anisotropy of the electrical transport behavior of Sr_2CrWO_6 (SCWO) thin films [4]. The surface of $SrTiO_3$ substrates becomes conducting under the the growth conditions of the SCWO films and thereby affects the electrical transport measurements performed on the films [3]. Therefore, a thin insulating buffer layer of $NdGaO_3$ has been grown epitaxially between the substrate and the Sr_2CrWO_6 thin film, which prevents oxygen loss of the $SrTiO_3$ substrate. This $NdGaO_3$ buffer layer grows coherently on the $SrTiO_3$ substrate and has the same in-plane lattice constants as the substrate.

We have grown several SCWO thin film samples using UHV pulsed laser deposition [5, 6]. The thin films were deposited from stoichiometric targets of $NdGaO_3$ and Sr_2CrWO_6 (for details see Tab. 1). For the in- and out-of-plane transport experiments the samples have been

[1] This work is supported by the DFG via SPP 1157 (project no. GR 1132/13-1).

Table 1: Deposition parameters during PLD growth

material	substrate temperature	pressure (Torr)	atmosphere
$NdGaO_3$	900°C	$7 \cdot 10^{-2}$	O_2
Sr_2CrWO_6	800°C	$6 \cdot 10^{-4}$	Ar+1%O_2

patterned using optical lithography and Ar ion beam etching. Whereas in the *in-plane* configuration the current is flowing along the *ab*-plane, for the *out-of-plane* configuration predominantly the *c*-axis transport is probed. Details of the sample geometry and fabrication techniques are given in [4]. Electrical transport measurements were performed for the in-plane and out-of-plane configuration in an Oxford continuous flow cryostat in the temperature range of $T = 2 \ldots 300$ K.

For the *out-of-plane* configuration nonlinear IVCs have been measured in the temperatures range between 50 K and 300 K (see Fig. 2). In contrast, the IVCs obtained for the *in-plane* configuration are linear over the whole temperature range. In addition, the absolute resistance obtained for the *out-of-plane* transport is much larger than that measured for the *in-plane* configuration. This large anisotropy of the electrical transport properties in our Sr_2CrWO_6 films is in good agreement with the recent theoretical predictions by Petrone *et al.* for Sr_2FeMoO_6 [7]. This double perovskite has an electronic structure that is similar to Sr_2CrWO_6 studied in our experiments. Therefore, it is tempting to conclude that the predictions made for Sr_2FeMoO_6 may also apply for the system Sr_2CrWO_6.

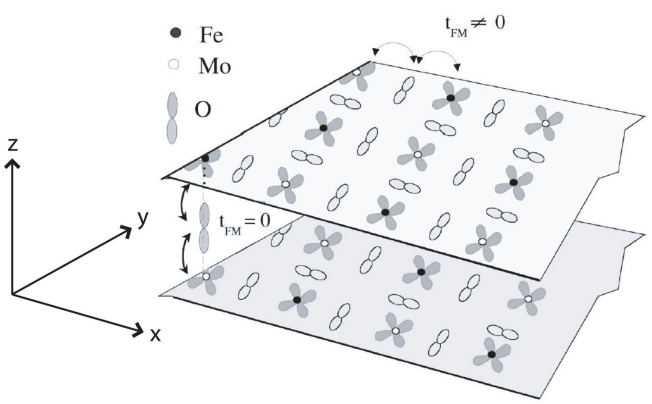

Figure 3: In Sr_2FeMoO_6 the hopping amplitude between the *d*-orbitals is large only *in-plane* and vanishingly small *out-of-plane* (taken from [7]).

Sr_2FeMoO_6 is theoretically predicted to be close to a metal-insulator-transition, which can be induced by pressure. In addition, by assuming an orbital ordering as shown in Fig. 3, for Sr_2FeMoO_6 the hopping amplitude is large within the *ab*-plane but is small in *c*-axis direction (*z*-direction in Fig. 3) due to the symmetry of the O^{2-} *p*-orbitals. That is, a large anisotropy in the electrical transport properties is expected with a much larger resistivity in *c*-axis direction. Applying this model to our Sr_2CrWO_6 films the orbital ordering shown in Fig. 3 could account for the nonlinear IVCs observed for the *out-of-plane* transport and also the strongly increased *c*-axis resistivity. We furthermore emphasize that the Sr_2CrWO_6 films are slightly strained. A very likely effect of the biaxial (compressive) coherency strain for the Sr_2CrWO_6 films grown on $SrTiO_3$ is to support (or even force) an orbital ordering effect as shown in Fig. 3. Whether or not this is indeed the case has to be clarified by further experiments.

It is known that the magnetic properties of the double perovskites can be influenced by subtle changes in stoichiometry, site ordering, steric effects or electronic doping. For example, electron doping can be used to increase the Curie temperature of the double perovskites by more than 100 K [2]. The results of this study show that strain effects may be used to strongly change the electrical transport properties of this material class. Interestingly, our results on strained

Sr_2CrWO_6 thin films indicate that they still have a high Curie temperature above 400 K although their electrical transport properties have been varied significantly.

In conclusion, the materials properties of the double perovskites can be tuned by several parameters. Besides the interesting physics involved in this aspect, this opens the possibility to design the materials parameters for applications. However, to realize spin electronic applications, more basic research has to be done to get a better understanding on the rich physics of this materials class.

References

[1] J. B. Philipp, P. Majewski, D. Reisinger, S. Geprägs, M. Opel, A. Erb, L. Alff and R. Gross, Acta Phys. Pol. A **105**, 7 (2004).
[2] S. Geprägs, diploma thesis, TU München (2004).
[3] J. B. Philipp, D. Reisinger, M. Schonecke, M. Opel, A. Marx, A. Erb, L. Alff and R. Gross, J. Appl. Phys. **93**, 6853 (2003).
[4] A. Boger, diploma thesis, TU München (2004).
[5] R. Gross, J. Klein, B. Wiedenhorst, C. Höfener, U. Schoop, J. B. Philipp, M. Schonecke, F. Herbstritt, L. Alff, Yafeng Lu, A. Marx, S. Schymon, S. Thienhaus, W. Mader, in *Superconducting and Related Oxides: Physics and Nanoengineering IV*, D. Pavuna and I. Bosovic eds., SPIE Conf. Proc. **Vol. 4058** (2000), pp. 278–294.
[6] J. Klein, C. Höfener, L. Alff, and R. Gross, Supercond. Sci. Technol. **12**, 1023 (1999); see also J. Magn. Magn. Mater. **211**, 9 (2000).
[7] P. Petrone and A. A. Aligia, Phys. Rev. B **66**, 104418 (2002).

Magnetic Polarization of W in the Double Perovskites Sr_2CrWO_6 and Ca_2CrWO_6

P. Majewski, S. Geprägs, A. Boger, A. Erb, M. Opel, L. Alff, R. Gross, F. Wilhelm[a], and A. Rogalev[a] [1]

[a] ESRF, Grenoble, France

The double perovskite Sr_2CrWO_6 is an interesting material both due to its rich physics and its interesting properties with respect to applications in spintronics. A high Curie temperature (458 K) has been found for ceramic samples and 100% spin polarization was predicted by band structure calculations [1].

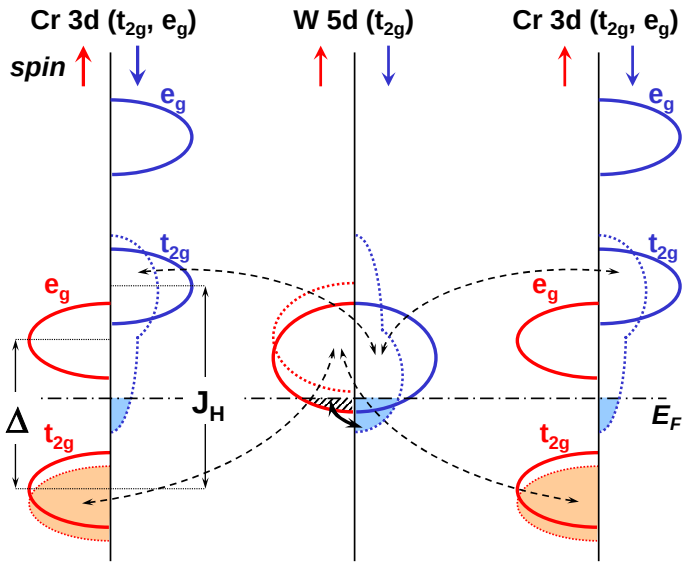

Figure 1: Sketch of the band structure for the illustration of the mechanism stabilizing the ferrimagnetic state in the double perovskite Sr_2CrWO_6 in the SFKT model [1]. The Fermi level lies in the crystal-field split Cr 3*d* spin-up band in between the t_{2g} and e_g levels. The solid lines mark the bands without hybridization, whereas the dashed lines denote the bands with hybridization. The arrows connect the hybridizing bands.

In the double perovskite Sr_2CrWO_6 the magnetic Cr ions are have a large distance ($\sim$ 6). Therefore, the question arises how the magnetic interaction is mediated between these ions so that such a high T_C can be stabilized. A model which explains the magnetic interaction in the double perovskite system is the Sarma-Fang-Kanamori-Terakura (SFKT) model [2, 3]. The basic ingredient of this generalized double exchange model (see Fig. 1) is the hybridization of bands of the same symmetry and spin direction, that is, in the case of Sr_2CrWO_6 of the W 5*d* t_{2g} and Cr 3*d* t_{2g} spin-up and spin-down bands [1]. The resulting shifts (level repulsion) of the W 5*d* t_{2g} and Cr 3*d* t_{2g} bands are shown in Fig. 1. Furthermore, significant hopping is only possible for the spin-down bands resulting in a broadening of only the spin-down bands as sketched in Fig. 1. As a result, only states in the t_{2g} spin-down bands are available at the Fermi level and the material is expected to be a half-metal. The itinerant spin-down electrons at the Fermi level, which are coupled antiferromagnetically to the core spins of the localized Cr 3*d* t_{2g} spin-up electrons due to a large on-site Hund's coupling, mediate a ferromagnetic interaction between the Cr sites. An important consequence of the SKFT-model is the fact that a local magnetic moment is induced on the W site due to the itinerant spin-down electrons. Since the spin-down electrons couple antiferromagnetically to the Cr 3*d* t_{2g} core spins a *ferrimagnetic* ordering is expected between the Cr 3*d* t_{2g} core spins and the induced moment on the W-site.

In order to validate this crucial prediction of the SFKT model, we investigated the magnetic moment on the W-site of the double perovskite Sr_2CrWO_6 by x-ray magnetic circular dichroism

[1] This work is supported by the BMBF (project no. 13N8279).

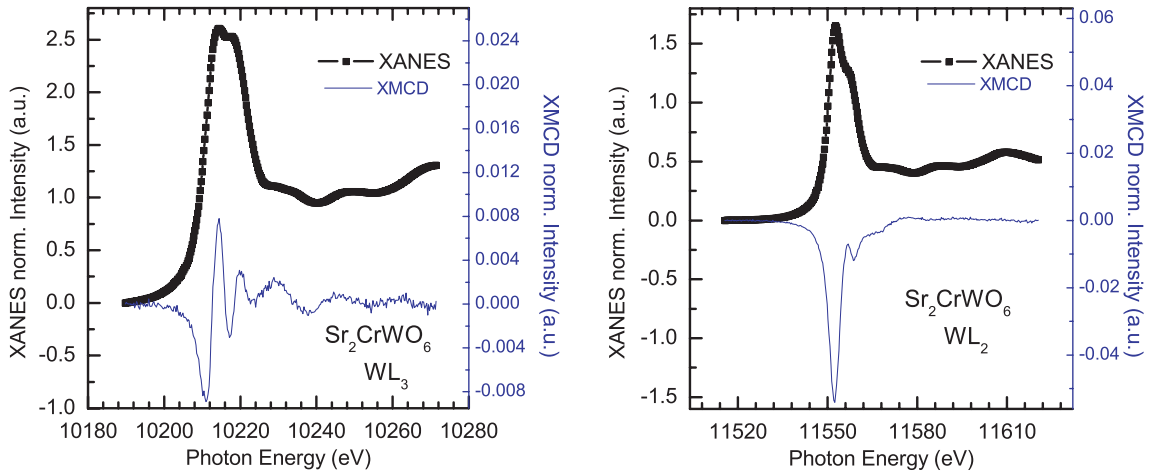

Figure 2: XANES spectra measured at the W L_3 absorption edge (left) and W L_2 absorption edge (right). A simple step-like function has been subtracted from the experimental data to take into account only the $2p$-$3d$ transitions (compare e.g. [8]). Also shown is the XMCD signal (blue lines), which is the difference signal of the XANES spectra measured with right- and left-hand circular polarized X-rays [5].

(XMCD). The measurements were performed at the ESRF (European Synchrotron Radiation Facility, beam line ID12) in Grenoble. XANES (x-ray absorption near-edge spectrum) spectra were recorded using the highly efficient total flourescence yield detection method. As for a magnetic element the absorption due to the selection rules is dependent on the helicity of the circularly polarized x-ray beam, the magnetic moment can be determined from XMCD spectra, which are calculated as direct difference between consecutive XANES scans recorded with opposite helicities of the incoming x-ray beam.

The preparation of the polycrystalline bulk samples is described in detail in [4]. The XANES and XMCD measurements were performed at the L_2 and the L_3 edges of W at 300 K. These edges (Fig. 2) show a rich fine structure sensitive to the valency and the spin state of the W, which is in turn related to the crystal field and exchange splitting. From Fig. 2 it is clear without any assumption, that W atoms bear a *non-negligible* magnetic moment, since strong XMCD signals are detected. For the evaluation of the XMCD spectra, the number of holes in the W d-band is assumed to be ≈ 6.3, according to new, fully relativistic band structure calculations with FP-LMTO [6]. Using the sum rules [7], the W spin moment is calculated to be $m_{\mathrm{spin}} = (-0.37 \pm 0.04)\mu_B$, which is in good agreement with the predicted moment of $m_{\mathrm{spin}} = -0.3\mu_B$ from band structure calculations [6].

We also investigated the related material Ca_2CrWO_6 with XMCD, where we found a reduced spin moment $m_{\mathrm{spin}} = (-0.22 \pm 0.02)\mu_B$ on the W site. This is expected, since the replacement of Sr^{2+} by Ca^{2+} causes a structural change from cubic to monoclinic, so that the O-W-O-Cr-O bonding angles differ from the ideal value of 180°. As a consequence, the electron on the W site is less delocalized and the magnetic interaction is reduced explaining the measured decrease in the spin moment. Our XMCD results are in good agreement with those measured for the related double perovskite Sr_2FeMoO_6 [8], where a spin magnetic moment of $m_{\mathrm{spin}} = (-0.32 \pm 0.05)\mu_B$ was detected on the Mo site.

In summary, we have investigated the magnetic moment on the W site of the double perovskite Sr_2CrWO_6 by XMCD on the L_2 and L_3 absorbtion edges. The observed spin magnetic moment is about $-0.37\mu_B$. This result is in agreement with the prediction of the SFKT model. The reduced moment found for the related compound Ca_2CrWO_6 confirms that a change in the bonding angles an, in turn, in the hopping amplitudes has a strong impact on the magnetic

interaction in these materials.

References

[1] J.B. Philipp, P. Majewski, L. Alff, A. Erb, R. Gross, T. Graf, M.S. Brandt, J. Simon, T. Walther, W. Mader, D. Topwal, and D.D. Sarma, Phys. Rev. B **68**, 144431 (2003).
[2] D.D. Sarma, E.V. Sampathkumaran, S. Ray, R. Nagarajan, S. Majumdar, A. Kumar, G. Nalini, T.N.G. Row, Sol. State Comm. **114**, 465 (2000).
[3] Z. Fang, K. Terakura, J. Kanamori, Phys. Rev. B **63**, 180407 (2001).
[4] S. Geprägs, Diploma Thesis, TU München (2004).
[5] P. Majewski, S. Geprägs, A. Boger, A. Erb, M. Opel, L. Alff, R. Gross, F. Wilhelm, and A. Rogalev, in preparation.
[6] Vaitheeswaran et al., private communication.
[7] F. Wilhelm, PhD Thesis, FU Berlin (2000).
[8] M. Besse, V. Cros, A. Garthélémy, H. Jaffrès, J. Vogel, F. Petroff, A. Mirone, A. Tagliaferri, P. Bencok, P. Decorse, P. Berthet, Z. Szotek, W.M. Temmerman, S.S. Dhesi, N.B. Brookes, A. Rogalev, and A. Fert, Europhys. Lett. **60**, 608 (2002).

Angle-dependent Magnetoresistance Probing the Electronic State of the Charge-Density-Wave Organic Conductor α-(BEDT-TTF)$_2$KHg(SCN)$_4$

D. Andres, M. V. Kartsovnik, and W. Biberacher [1]

The extremely high anisotropy of the electronic system in organic conductors is responsible for numerous exciting phenomena in high magnetic fields (see [1] for a review). In particular, strong periodic oscillations of the semiclassical magnetoresistance arise due to the cyclotron motion of the charge carriers on a slightly warped cylindrical [2] or planar [3, 4] Fermi surface when the sample is rotated in a constant magnetic field. These angle-dependent magnetoresistance oscillations (AMRO) have proved to be a very efficient tool for studying Fermi surfaces of layered metals [1].

The organic conductor α-(BEDT-TTF)$_2$KHg(SCN)$_4$ is an illustrative example of how the AMRO phenomenon can be used for exploring the electronic states in low-dimensional materials. The charge-density-wave (CDW) transition at $T_c \simeq 8.5$ K in this compound is accompanied by a dramatic change in the magnetoresistance anisotropy: above T_c it exhibits the "2D" AMRO originating from the cylindrical part of the Fermi surface whereas at lower temperatures the "1D" AMRO indicate a new plane of open electron orbits to arise in k-space [5]. In this work we have carried out a detailed investigation of the effects of the magnetic field orientation on the interlayer magnetoresistance of the title compound at different points of its "magnetic field – temperature – pressure" (B–T–P) phase diagram.

The experiment was done using a home-built insert allowing a variable-rate in-situ rotation of the sample around two mutually orthogonal axes with respect to the external magnetic field. The insert can be operated down to liquid ^{3}He temperatures in conventional superconducting magnets available at the WMI as well as in the high-field 10 MW and 20 MW resistive magnets at the Grenoble High Magnetic Field Laboratory. The measurements under high pressure were performed by using a home-made miniature pressure cell specially designed to fit in the rotating insert.

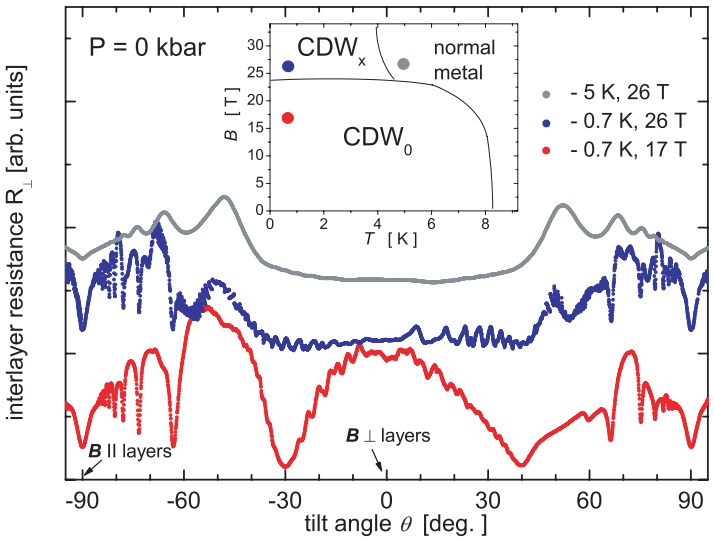

Figure 1: Ambient-pressure interlayer resistance of α-(BEDT-TTF)$_2$KHg(SCN)$_4$ as a function of tilt angle θ, at different fields and temperatures. The curves are offset for clarity. The points on the B–T phase diagram at which the data are taken are indicated in the inset.

Fig. 1 shows typical traces of the ambient-pressure magnetoresistance as a function of the angle θ between the direction normal to the highly conducting layers and the magnetic field recorded at different temperatures and field strengths. The corresponding points on the ambient-pressure B–T phase diagram are indicated in the inset. The upper curve taken at $T = 5$ K, $B = 26$ T demonstrates the "2D" AMRO characteristic of the normal metallic state. The interlayer resistance exhibits peaks at the field orientations at which the average of the electron velocity over the cyclotron period becomes nearly zero. Such orientations

[1] In collaboration with I. Sheikin, GHMFL, Grenoble, France

repeat periodically in the scale of $\tan\theta$, the period being determined by the in-plane Fermi wave vector k_F and the interlayer spacing d: $\Delta(\tan\theta) \approx \pi/k_F d$ [1, 2].

At lower fields and temperatures the compound is in the CDW_0 groundstate and shows the "1D" AMRO [6, 7]. This is illustrated by the lower curve in Fig. 1 corresponding to $T = 0.7$ K, $B = 17$ T. Here the characteristic features of the semiclassical magnetoresistance are rather sharp dips at the commensurate field orientations (i.e. when the field projection on the plane of open orbits in k-space is perpendicular to a translation vector in this plane). The smaller, rapid oscillations in the low-temperature angular sweeps are due to the Shubnikov-de Haas effect which will not be considered in this paper. Note that at the field perpendicular to the layers the magnetoresistance is high and decreases upon tilting the field, in contrast to the case of the normal state where the magnetoresistance is at its minimum at $\theta = 0$.

An increase of the magnetic field above ≈ 23 T leads to the suppression of the low-field CDW_0 ground state; however, at $T \leq 4$ K the CDW ordering survives by means of adding a small ($< 2\mu_B B/\hbar v_F$) field-dependent shift to the modulation wave vector [8]. As a result a hybrid of a charge- and spin-density waves, designated by CDW_x in the inset in Fig. 1, emerges at high fields. The corresponding energy gap is considerably smaller than that of the CDW_0 state [9]. This leads to strongly enhanced magnetic breakdown effects at moderate tilt angles, $|\theta| < 60°$. In particular, the angular dependence of the magnetoresistance looks practically the same as that in the normal metallic state at these angles. Indeed, the $R(T)$ curve recorded at $T = 0.7$ K, $B = 26$ T (middle curve in Fig. 1) shows a minimum at $\theta = 0°$ and peaks at $\theta \approx \pm 50°$, exactly as in the normal state (the upper curve). However, with increasing the tilt angle, the magnetic breakdown probability exponentially diminishes, so that at $60° < |\theta| < 90°$ sharp dips characteristic of the CDW state appear again in the angular sweep. Besides the regular sharp dips, additional features are clearly resolved at high tilt angles. These features are only observed in the CDW_x state and originate from the novel type of field-induced transitions between quantized CDW subphases [10].

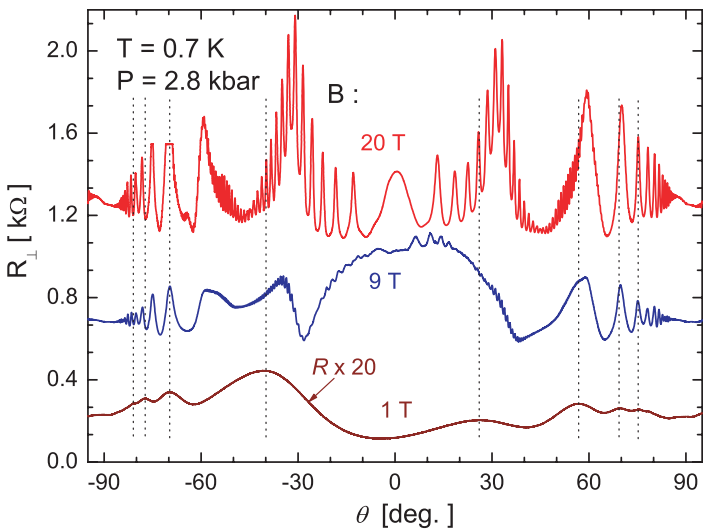

Figure 2: Angular sweeps of the interlayer resistance of α-(BEDT-TTF)$_2$KHg(SCN)$_4$ at the pressure of 2.8 kbar. The curves are offset for clarity; additionally, the 1 T resistance is multiplied by the factor of 20. The vertical dotted lines are plotted through the positions of "2D" AMRO peaks in the 1 T curve.

Thus, we conclude that the angle-dependent magnetoresistance of α-(BEDT-TTF)$_2$KHg(SCN)$_4$ is fully consistent with the phase diagram and can be used as a probe of the electronic state of this material.

Whilst the phase transitions taking place in the present compound at ambient pressure have been established by means of thermodynamic magnetization measurements [11], only resistive experiments have so far been available under high pressure. The resistance data, involving various temperature and field dependent scattering processes, is obviously more difficult to interpret in terms of phase transitions. Nevertheless, the B–T–P diagram of α-(BEDT-TTF)$_2$KHg(SCN)$_4$ has recently been proposed [12] based on detailed studies of Kohler plots of

the magnetoresistance. Here we have verified the proposed phase diagram by measuring the angle-dependent magnetoresistance under pressure.

Fig. 2 displays angular sweeps of the interlayer magnetoresistance made at a low temperature, under the pressure of 2.8 kbar. According to our previous studies [12, 13], the CDW is completely suppressed at this pressure in the absence of the magnetic field. Indeed, the angular dependence of the magnetoresistance measured at the low magnetic field, $B = 1$ T, shows the typical "2D" AMRO and the anisotropy characteristic of the normal state (cf. the upper curve in Fig. 1: the overall behaviour is the same although the positions of the resistance peaks differ due to different orientations of the rotation axis with respect to the in-plane crystallographic axes).

At increasing the field up to 9 T the behaviour drastically changes. The magnetoresistance is now maximum at $\theta \simeq 0^\circ$ and two sharp dips, at $\theta \approx -28^\circ$ and $+38^\circ$ are observed, indicating that the material is in the CDW state at these conditions. This perfectly agrees with the earlier suggested stabilization of the CDW due to the enhanced orbital effect of the magnetic field under pressure [12]. In the present compound the orbital effect is determined by the magnetic field component perpendicular to the layers. With tilting the field, this component decreases and eventually becomes lower than the threshold value necessary to induce the CDW. This is, apparently, the reason for switching from the "1D" to the "2D" AMRO regime in the 9 T curve in Fig. 2 at the tilt angles above $\simeq 60^\circ$.

Finally, at the highest field of 20 T the Pauli paramagnetic effect of the field overwhelms the orbital effect, resulting in the suppression of the low-field CDW state. The 20 T curve in Fig. 2 clearly demonstrates "2D" AMRO, pointing that at this high field the CDW gap is either strongly reduced (as in the CDW_x state) or completely suppressed. Further analysis is needed in order to figure out which of the latter two possibilities is realized. Here we only note that the positions of the "2D" AMRO peaks at 9 and 20 T clearly do not coincide with those at the lowest field, 1 T, at which the compound is believed to be in the normal state. More detailed AMRO measurements should clarify the reason for such a difference and provide important information on the electronic structure of this fascinating material under high pressure.

References

[1] M. V. Kartsovnik, Chem. Rev. **104**, 5737 (2004).

[2] R. Yagi, Y. Iye, T. Osada, and S. Kagoshima, J. Phys. Soc. Jpn. **59**, 3069 (1990); V. G. Peschansky, J. A. Roldan Lopes, and T. Gnado Yao, J. Phys. I **1**, 1469 (1991); M. V. Kartsovnik, V. N. Laukhin, S. I. Pesotskii, I. F. Schegolev, and V. M. Yakovenko, J. Phys. I **2**, 89 (1992).

[3] T. Osada, S. Kagoshima, and N. Miura, Phys. Rev. B **46**, 1812 (1992); A. G. Lebed, N. N. Bagmet, and M. J. Naughton, Phys. Rev. Lett. **93**, 157006 (2004).

[4] G. M. Danner, W. Kang, and P. M. Chaikin, Phys. Rev. Lett. **72**, 3714 (1994).

[5] M. V. Kartsovnik and V. N. Laukhin, J. Phys. I France **6**, 1753 (1996).

[6] M. V. Kartsovnik, A. E. Kovalev, and N. D. Kushch. J. Phys. I France **3**, 1187 (1993); A. E. Kovalev, M. V. Kartsovnik, R. P. Shibaeva, L. P. Rozenberg, I. F. Schegolev, and N. D. Kushch, Solid State Commun. **89**, 575 (1994).

[7] T. Sasaki and N. Toyota, Phys. Rev. B **49**, 10120 (1994); Y. Iye, R. Yagi, N. Hanasaki, S. Kagoshima, H. Mori, H. Hujimoto, and G. Saito, J. Phys. Soc. Jpn., **63**, 674 (1994).

[8] D. Zanchi, A. Bjelis, and G. Montambaux, Phys. Rev. B **53**, 1240 (1996).

[9] R. H. McKenzie, G. J. Athas, J. S. Brooks, R. G. Clark, A. S. Dzurak, R. Newbury, R. P. Starrett, A. Skougarevsky, M. Tokumoto, N. Kinoshita, T. Kinoshita, and Y. Tanaka, Phys. Rev. B **54**, R8289 (1996).

[10] D. Andres, M. V. Kartsovnik, P. D. Grigoriev, W. Biberacher, and H. Müller, Phys. Rev. B **68**, 201101(R) (2003).

[11] P. Christ, W. Biberacher, M. V. Kartsovnik, E. Steep, E. Balthes, H. Weiss, and H. Müller, JETP Lett. **71**, 303 (2000).

[12] D. Andres, M. V. Kartsovnik, W. Biberacher, H. Weiss, E. Balthes, H. Müller, and N. Kushch, Phys. Rev. B **64**, 161104(R) (2001).

[13] D. Andres, M. V. Kartsovnik, W. Biberacher, K. Neumaier, and H. Müller, J. Phys. IV France **12**, PR9–87 (2002).

Magnetization Studies of the Nuclear Spin Ordered Phases of Solid ^{3}He in Silver Sinters

Erwin Schuberth, Matthias Kath and Carmen Millan-Chacartegui [1]

The spin structures of the nuclear magnetically ordered phases of solid ^{3}He, commonly denoted as low field phase (lfp) and high field phase (hfp) above 0.4 T, are still not known exactly. While the low field phase in bulk material most probably has the U2D2 structure proposed by Osheroff et al. [1], the spin structure of the "weak ferromagnetic" high field phase is only inferred from its magnetization. The theoretical description of the magnetic phase diagram is based on multiple spin exchange processes which lead to competing quantum mechanical exchange interactions. Three and four spin exchange is favored in the dense lattice (body centered cubic structure below 100 bar and hexagonal closed package structure above) since two particle exchange requires too much deformation of the lattice. Although this theory has been worked out in a very elaborate way by Roger et al. [2], quantitative details of the experimental phase diagram [3] are still not reproduced.

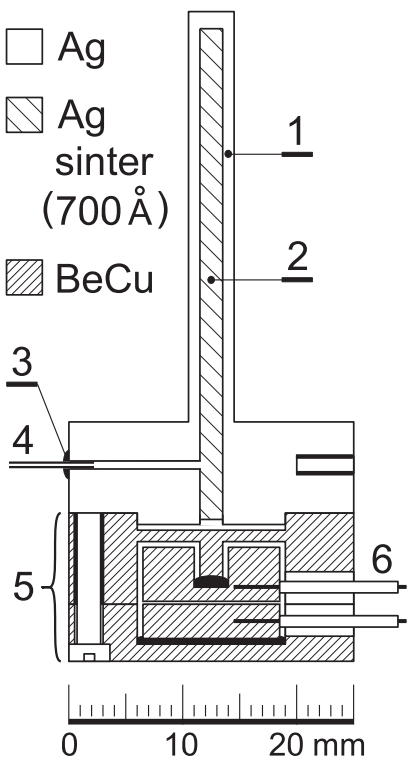

Figure 1: Drawing of pressure cell with capacitive Straty-Adams pressure transducer for use in SQUID magnetometer.

To clarify experimentally the spin structures of the two phases in the sinters needed for cooling and absorbing the heat released from the neutron absorption in ^{3}He, we started neutron scattering experiments in collaboration with the Hahn-Meitner Institut in Berlin and other European and US groups, see footnote, ultimately to reach even the high pressure hcp ordered phase below 20μK [4].

Crucial requirements for neutron scattering from solid ^{3}He are that a single crystal can be formed in the sinter and that the sample remains in the ordered state long enough to perform neutron scattering experiments. Also it has to be considered that possibly in the small pores of a sinter solid ^{3}He orders differently than in the bulk.

In the first part of the work NMR spectra from solid ^{3}He were taken with a copper coil around a Ag sinter through which the solid is cooled.

The most remarkable result was that the intensity of the NMR Lamor line decreased to nearly zero in the U2D2 phase. A line splitting, although not as distinct as in Osheroff's work [1], indicating a sample with some favorably oriented crystallites could be observed but also with very low intensity. We wanted to check if the low NMR intensity reflects the true magnetization of the ordered solid with an independent method, the dc magnetization measured with a SQUID magnetometer. And by varying the sinter fabrication and the crystal growth times we tried to find the optimal way to grow single crystals in sinters.

[1]This work was supported by the the EU in collaboration with HMI Berlin, Royal Holloway Univ. London, CNRS Grenoble, Univ. Paris, Saclay, and Univ. Florida, Gainesville.

The dc magnetization was measured with a homemade rf SQUID detection system, see e.g. [5] consisting of an astatic pair of pickup coils with 6 mm inner diameter into which the extension of a pressure cell was mounted. This extension was filled with initially 700 Å silver powder ("Japanese powder") which was pressed and annealed in different ways. The solid ^{3}He inside the pickup coil is cooled through this sinter. The cell body itself was again cooled by a Ag rod coming from the nuclear stage. The cell design is shown in Fig. 1.

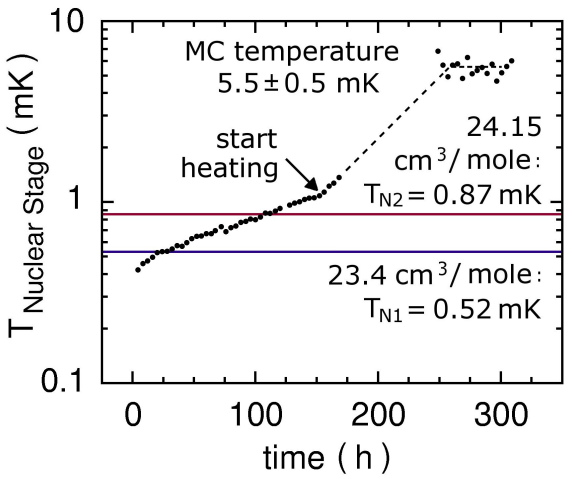

Figure 2: Typical warmup of solid ^{3}He vs time. The two T_{Neel} are shown for the two different molar volumes used in this run: 23.4 cc/mole and 24.15 cc/mole. The temperature of the nuclear stage was determined by pulsed NMR on ^{63}Cu. The residual heat leak following from this curve is 7 nW, the faster warming after 150 h is due to extra heating.

Cooling was provided by a 0.9 mole $PrNi_5$ nuclear demagnetization stage whose temperature and warm-up behavior after demagnetization, see Fig. 2, was monitored by pulsed NMR on the ^{63}Cu isotope in a high purity Cu sample screwed to the nuclear stage. Here a measuring field of 45 mT was used, big enough that the two Cu isotope lines are well separated in the spectrum.

We performed several runs to grow single crystals in different sinters, all with the blocked capillary method starting around 58 bar at 4.2 K. They ended at cell pressures between 34.4 bar and 41.58 bar. In the last attempts care was taken to stop the solidification just after reaching the melting curve and then to continue slowly (6h) to obtain full growth and additionally 4h to cool the sample to sub-mK temperatures.

SQUID magnetization signals were then measured with several solid ^{3}He samples. The final pressures in the SQUID experiments were around 34.4 bar within a limited range of molar volumes around 24.24 cm^3/mole, the value at the melting curve. In the first two sinters which were not heat treated, the nuclear ordering to the low field phase could hardly be reached, in fact only in one case with an elaborate demagnetization procedure. In this case, the ordering was only partly and precise data on the magnetization could not be obtained. Only after heat treatment (2 h at 142 °C) of the third sinter with a packing fraction of 50 %, the magnetization of the fully ordered solid could be determined, see Figs 4 and 5. The sample remained in the ordered state for 90 h and reached full thermal equilibrium after some 5 h, see Fig. 6 which shows the calculation of the solid ^{3}He

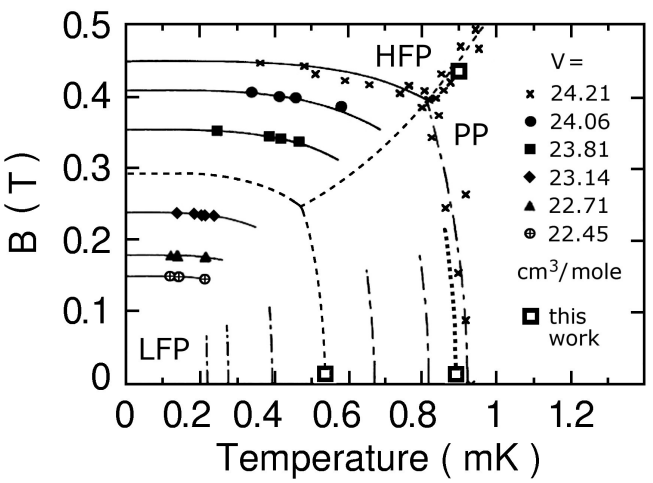

Figure 3: Pressure diagram at various molar volumes after Fukuyama et al. [6] The dash-dotted lines indicate their scaled phase boundaries at low fields. Our proposed transition lines at the molar volumes used in this work (dotted and dashed lines) are shown together with our observed transition temperatures (large open squares).

from the known temperature of the nuclear stage.

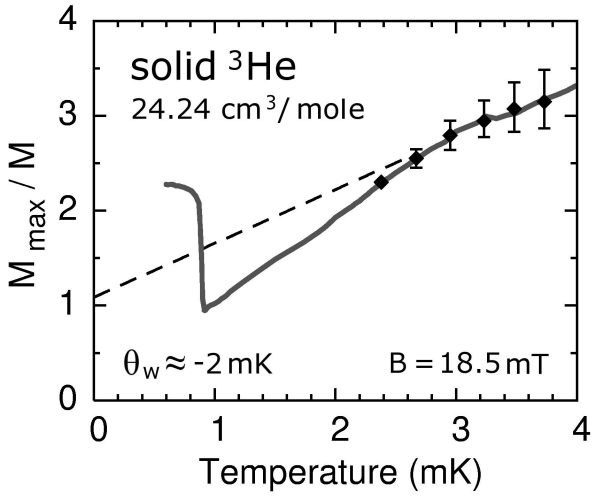

Figure 4: Normalized magnetization through the nuclear ordering transition of solid ^{3}He vs inverse temperature in sinter #3. The pressure was just above the melting pressure, molar volume 24.24 cm^3/mole. Here the sample is fully in the ordered state.

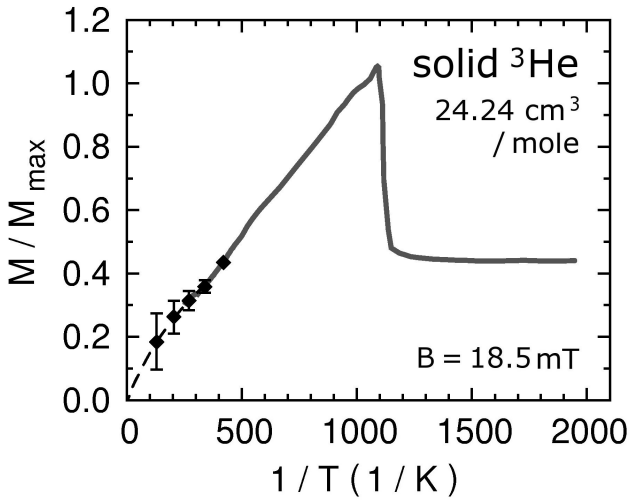

Figure 5: Data of Fig. 10 plotted as inverse magnetization of solid ^{3}He vs temperature.

The sinter fabrication results can be summarized as follows: measurements of the specific area of our sinters gave 5.2 m^2/cm^3 for the "presintered" nominally 700 Å powder and 3.3 m^2/cm^3 for the annealed sinter #3 in the cell. A simple estimate, assuming that for a packing fraction of 50 % half of the cell volume is filled with spheres of radius r and that 20 % of the surface area is lost due to contact regions, gives about 15 m^2/cm^3 nominal specific area for 700 Å particles. 5.2 m^2/cm^3 would be reached with 2700 Å spheres, and 3.3 m^2/cm^3 is provided by 4200 Å ones. So, obviously, in our presinter process we cluster the 700 Å particles to 2700 Å ones. The additional annealing of our third sinter increases this value to 4200 Å. The first sinter with 40% packing fraction had additionally large empty regions so that large parts of the solid did not become cold and ordered. The second sinter with 70% packing fraction was pressed too tight so that solid was not well formed inside and no useful results could be obtained. Finally, the third sinter with 50% packing fraction and annealed finally was most suitable for obtaining cold and well ordered solid. In the NMR case a 47% packed sinter, un-annealed, was used which allowed cooling into the ordered state but with long time constants. Probably again, no well ordered (although cold) solid was obtained and thus no distinct splitting of the NMR lines.

In both the NMR cell and the SQUID cell, the most successful attempt to grow "good" crystals was to stop the solidification just after reaching the melting curve and then to continue cooling very slowly to obtain full solidification and reaching mK temperatures. The final cell pressure was always somewhat below the value at which the sample left the melting curve. This is obviously due to recrystallization, of solid ^{3}He in the heat sink of the filling line since it coincided with the drop in temperature of the final heat exchanger as the phase boundary wandered through it during startup of the dilution refrigerator when the first cooling is done. This effect had to be taken into account for the initial pressure in the cells.

Our dc magnetization results show the expected decrease of the solid magnetization in the low

field ordered phase, consistent with the U2D2 spin structure. The antiferromagnetic exchange interaction tends to order the spins perpendicular to the external field and the longitudinal magnetization should drop to zero, but the torque of the external field adds a component along its direction. In Roger's original work [2] this parallel component is given by the strength of the ring exchange contributions in relation to the external torque of the magnetic field on the sublattice magnetization. A drop to 40% of the maximum magnetization is fully consistent with the ring exchange parameters used by Roger et al. to construct their magnetic phase diagram and thus with the U2D2 structure.

Furthermore, the plots of M^{-1} vs T and of M vs T^{-1} show a Curie-Weiss law between 10 mK and 3 mK with a small Θ_{Weiss} of - 2.0(5) mK, consistent with the antiferromagnetic U2D2 state. Why there is a pure Curie dependence between 3 mK and 1 mK is not clear at present.

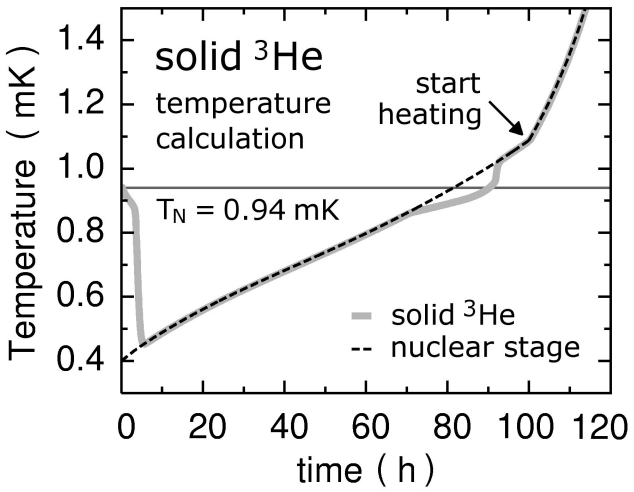

Figure 6: Calculated solid ^{3}He temperatures for the data of Figs. 4 and 5 vs time after the end of the demagnetization. The initial plateau and the one between 70 and 90 h are due to the latent heat at the first order phase transition from the paramagnetic to low field phase and out of it respectively.

As for the growth and cooling ^{3}He crystals for neutron scattering experiments, our present result with the annealed third sinter gives us some encouragement that with even slower growth and cooling rates, a single crystal with a small number of magnetic domains can be grown which is suitable for this purpose. Indeed, the Berlin group was successful in finding sharp structural reflexes with similarly grown samples. Cooling into the ordered states has still to be done there.

References

[1] D. D. Osheroff, M. C. Cross, and D. S. Fisher *Phys. Rev. Lett.* **44**, 792 (1980)
[2] M. Roger, J. H. Hetherington, and J. M. Delrieu *Rev. Mod. Phys.* **55**, 1 (1983)
[3] J. S. Xia, W. Ni and E. D. Adams *Phys. Rev. Lett.* **70**, 1481 (1993)
[4] T. Lang, P. L. Moyland, D. A. Sergatskov, E. D. Adams, and Y. Takano *Phys. Rev. Lett.* **70**, 1481 (1993)
[5] Erwin A. Schuberth *Intern. Journ. Modern Physics B* **10**, 357 (1996)
[6] H. Fukuyama, T. Okamoto, T. Fukuda, H. Akimoto, H. Ishimoto, and S. Ogawa *Phys. Rev. Lett.* **67**, 1274 (1991)

Impurity–limited Transport in Unconventional Superconductors

Dietrich Einzel

Unconventional pairing correlations occur in a large class of Fermi systems including heavy fermion superconductors, hole doped high–T_c cuprate superconductors, the Ruddlesden–Popper system Sr_2RuO_4, the superfluid phases of ^{3}He and others. They are defined through the vanishing Fermi surface average of the energy gap $\langle\Delta_{\mathbf{p}}\rangle_{\rm FS}\equiv 0$ and manifest themselves by the sensitivity of thermodynamic, response and transport properties to the presence of even small concentrations of nonmagnetic impurities. Motivated by the recent observation of an impurity–limited viscosity in ^{3}He–B [1], we explore in this contribution quite generally the impurity–limited transport in these systems for arbitrary scattering phase shifts and can eventually describe the route from weak (Born) to strong (unitary) scattering.

A general transport parameter can be defined through the constitutive relation that connects a generalized current $\mathbf{j}^a$ with the gradient of its thermodynamically conjugate field δu^a:

$$\mathbf{j}^a \;=\; -\mathbf{T}^{aa}\cdot\nabla\delta u^a \;;\; \left(T^{aa}_{\mu\nu}\right)_{\rm e,i} = N_{\rm F}\left\langle 2\int_0^\infty dE_{\mathbf{p}}\left(-\frac{\partial\nu_{\mathbf{p}}}{\partial E_{\mathbf{p}}}\right)a^2_{\mathbf{p}}v_{\mathbf{p}\mu}v_{\mathbf{p}\nu}\tau_{\rm e,i}(\tilde{E}_{\mathbf{p}})\right\rangle_{\rm FS} \tag{1}$$

Here $a_{\mathbf{p}}$ is a general vertex which classifies the transport process of interest. In the cases of the diffusive thermal conductivity, $a_{\mathbf{p}}=E_{\mathbf{p}}$, $\mathbf{j}^a$ is the entropy current and δu^a the temperature change $\delta T/T$. In the case of the shear viscosity $a_{\mathbf{p}}=\mathbf{p}$, $\mathbf{j}^a$ is the momentum current and δu^a the normal velocity field $\mathbf{v}^{\rm n}$. In eq. (1) $N_{\rm F}$ denotes the density of states for both spin projections, $E_{\mathbf{p}}$ is the Bogoliubov quasiparticle (bogolon) energy, $\nu_{\mathbf{p}}=[\exp(E_{\mathbf{p}}/k_{\rm B}T)+1]^{-1}$ the bogolon momentum distribution and $\langle\ldots\rangle_{\rm FS}$ denotes the Fermi surface (angular) average. In (1) the index e(i), refers to elastic (inelastic) scattering, respectively. The impurity–limited transport time $\tau_{\rm e}(\tilde{E}_{\mathbf{p}})$ is defined by

$$\tau_{\rm e}(\tilde{E}_{\mathbf{p}}) \;=\; \frac{\hbar}{\Im\sqrt{\tilde{E}^2_{\mathbf{p}}-\Delta^2_{\mathbf{p}}}}\frac{1}{2}\left(1+\frac{|\tilde{E}^2_{\mathbf{p}}|-\Delta^2_{\mathbf{p}}}{|\tilde{E}^2_{\mathbf{p}}-\Delta^2_{\mathbf{p}}|}\right) \tag{2}$$

Here $\tilde{E}_{\mathbf{p}}$ is the bogolon energy renormalized by the impurity self–energy (computed within the T–matrix approximation [2]):

$$\tilde{E}_{\mathbf{p}} \;=\; E_{\mathbf{p}}+\Sigma_{\rm e}(\tilde{E}_{\mathbf{p}}) \;;\; \Sigma_{\rm e}(\tilde{E}_{\mathbf{p}}) = i\Gamma_{\rm N}\frac{f_0(\tilde{E}_{\mathbf{p}})(1+c^2)}{c^2+f_0^2(\tilde{E}_{\mathbf{p}})} \;;\; f_0(\tilde{E}_{\mathbf{p}}) = \left\langle\frac{\tilde{E}_{\mathbf{p}}}{\sqrt{\tilde{E}^2_{\mathbf{p}}-\Delta^2_{\mathbf{p}}}}\right\rangle_{\rm FS} \tag{3}$$

In eq. (3) $\Gamma_{\rm N}=1/\tau_{\rm N}=2n_i/\pi N_{\rm F}(1+c^2)$ represents the normal state scattering rate, with n_i the impurity concentration and the parameter $c=\cot\delta_0$ is related to the s–wave scattering phase shift δ_0. The impurity self energy has the following low energy behavior:

$$\begin{aligned}\Sigma_{\rm e}(\tilde{E}_{\mathbf{p}}) \;&=\; \Sigma'_{\rm e}(\tilde{E}_{\mathbf{p}})+i\Sigma''_{\rm e}(\tilde{E}_{\mathbf{p}}) \\ \Sigma'_{\rm e}(\tilde{E}_{\mathbf{p}}) \;&\overset{E_{\mathbf{p}}\to 0}{=}\; 0 \;;\; \Sigma''_{\rm e}(\tilde{E}_{\mathbf{p}}) \overset{E_{\mathbf{p}}\to 0}{=} \Sigma''_{\rm e}(0)\end{aligned} \tag{4}$$

The transport $\tau_{\rm e}(\tilde{E}_{\mathbf{p}})$ time can be evaluated analytically in the limits $E_{\mathbf{p}}\ll\Delta_0$ and $E_{\mathbf{p}}\gg\Delta_0$ (with Δ_0 the gap maximum):

$$\tau_{\rm e}(\tilde{E}_{\mathbf{p}}) \;=\; \begin{cases}\frac{\hbar\Sigma''^2_e(0)}{[\Delta^2_{\mathbf{p}}+\Sigma''^2_e(0)]^{\frac{3}{2}}} & ;\; \tilde{E}_{\mathbf{p}}\ll\Delta_0 \\ \tau_{\rm N}\frac{E_{\mathbf{p}}}{\sqrt{E^2_{\mathbf{p}}-\Delta^2_{\mathbf{p}}}}\frac{1+c^2[f_0(E_{\mathbf{p}})]^{-2}}{(1+c^2)f_0(E_{\mathbf{p}})}\Theta(E_{\mathbf{p}}-\Delta_{\mathbf{p}}) & ;\; \tilde{E}_{\mathbf{p}}\gg\Delta_0\;;\;\Gamma_{\rm N}\ll\Delta_0\end{cases} \tag{5}$$

Eq. (5) can be used to calculate both the zero temperature limit and the temperature dependence of $T^{aa}_{\mu\nu}$. In the zero temperature limit we may define a dimensionless quantity $C^{aa}_{\mu\nu}$ through

$$C^{aa}_{\mu\nu} = \frac{\hbar\Gamma_{\rm N}}{\langle a^2(\hat{\mathbf{p}})\hat{\mathbf{p}}_\mu\hat{\mathbf{p}}_\nu\rangle_{\rm FS}}\left\langle \frac{\Sigma_e''^2(0)}{[\Sigma_e''^2(0)+\Delta^2_{\mathbf{p}}]^{\frac{3}{2}}}a^2(\hat{\mathbf{p}})\hat{\mathbf{p}}_\mu\hat{\mathbf{p}}_\nu\right\rangle_{\rm FS} \tag{6}$$

Here $a(\hat{\mathbf{p}})$ denotes the $\hat{\mathbf{p}}$–dependent part of the vertex $a_{\mathbf{p}}$. The tensor $C^{aa}_{\mu\nu}$ describes a normal–like low T contribution to the quasiparticle transport induced by resonant pair–breaking as a consequence of strong impurity scattering in the unitary limit. The pair breaking parameter $C^{aa}_{\mu\nu}$ will decrease rapidly with δ_0 deceasing from $\pi/2$ and vanish for a critical value δ_{0c} which depends on the gap symmetry. Note that in the unitary limit $C^{aa}_{\mu\nu}/\Gamma_{\rm N}$ turns out to be independent of the parameter $\Gamma_{\rm N}$ under certain conditions. This phenomenon is known as *universal transport* in unconventional (nodal) superconductors. It has been proposed for the first time by P. A. Lee [2] and was observed in various experiments. The temperature dependence of $T^{aa}_{\mu\nu}$ can be estimated by observing, that the self–consistent solution of eq. (3) is relevant only for low energies. At high energies one may use the asymptotic form of $\tau_{\rm e}(\tilde{E}_{\mathbf{p}})$ for $E_{\mathbf{p}} \gg \Delta_0$. This gives rise to the definition of T–dependent generalized Yosida functions

$$Y^{aa(n)}_{\mu\nu}(T) = \frac{1}{\left\langle\int_{-\infty}^{\infty}d\xi_{\mathbf{p}}\left(-\frac{\partial n_{\mathbf{p}}}{\partial\xi_{\mathbf{p}}}\right)a^2_{\mathbf{p}}\hat{\mathbf{p}}_\mu\hat{\mathbf{p}}_\nu\right\rangle_{\rm FS}}\left\langle 2\int_{\Delta_{\mathbf{p}}}^{\infty}\frac{dE_{\mathbf{p}}E_{\mathbf{p}}}{\sqrt{E^2_{\mathbf{p}}-\Delta^2_{\mathbf{p}}}}\left(-\frac{\partial\nu_{\mathbf{p}}}{\partial E_{\mathbf{p}}}\right)\frac{a^2_{\mathbf{p}}\hat{\mathbf{p}}_\mu\hat{\mathbf{p}}_\nu}{|f_0(E_{\mathbf{p}})|^n}\right\rangle_{\rm FS} \tag{7}$$

From (6) and (7) one may construct the following interpolation procedure for the transport coefficient $T^{aa}_{\mu\nu}(T)$:

$$\left(T^{aa}_{\mu\nu}\right)_{\rm e}/\left(T^{aa}_{\mu\nu}\right)^{\rm N}_{\rm e} = C^{aa}_{\mu\nu}+(1-C^{aa}_{\mu\nu})\frac{Y^{aa(1)}_{\mu\nu}(T)+c^2\,Y^{aa(3)}_{\mu\nu}(T)}{1+c^2} \tag{8}$$

The interpolation (8) has the following virtues. (i) It is exact in the limit $T\to 0$ (for arbitrary values of the impurity scattering phase shifts δ_0) and just below the transition temperature. (ii) It is, though approximate, a physically transparent representation of the behavior of $T^{aa}_{\mu\nu}$ at intermediate temperatures in terms of generalized Yosida functions $Y^{\mu\nu}_{ab(n)}(T)$. The latter can be evaluated even analytically along the lines of ref [3]. (iii) The treatment is valid for a general vertex $a_{\mathbf{p}}$ and hence unifies the description of the shear viscosity, the (diffusive) thermal and electric conductivity. (iv) It is applicable even to dirty Fermi superfluids like ^{3}He in aerogel [1]. Finally, inelastic scattering can be accounted for within Matthiessen's rule approximation:

$$T^{aa}_{\mu\nu} = \left(\frac{1}{\left(T^{aa}_{\mu\nu}\right)_{\rm e}}+\frac{1}{\left(T^{aa}_{\mu\nu}\right)_{\rm i}}\right)^{-1} \tag{9}$$

The inelastic contributions to $T^{\mu\nu}_{aa}$ have to be discussed for every system separately. An extension of the theory to incude Raman relaxation as well as an application eq. (8) and (9) to various unconventional superconductors and the superfluid phases of ^{3}He in aerogel will be subject to a series of forthcoming publications.

References

[1] A. I. Golov, D. Einzel, G. Lawes, K. Matsumoto, and J. M. Parpia, Phys. Rev. Lett. **92**, 105301-1 (2004)
[2] P. J. Hirschfeld, P. Wölfle, and D. Einzel, Phys. Rev. **B 37**, 83 (1988)
[3] D. Einzel, Journal of Low Temp. Phys. **130**, 493 (2003)
[4] P. A. Lee, Phys. Rev. Lett. **71**, 1887 (1993)

Doping and Lattice Effects in the Half-metallic Double Perovskite Sr_2CrWO_6

S. Geprägs, O. Sanganas, P. Majewski, C. Ritter[a], J. Simon[b], W. Mader[b], A. Erb, M. Opel, L. Alff, and R. Gross [1]

[a] Institut Laue-Langevin, Grenoble
[b] Institut für Anorganische Chemie, Bonn

In the field of spin electronics, the search for new materials with half-metallicity and high Curie-temperatures T_C represents an important challenge. Recently, it has been reported that ferromagnetic double perovskites such as Sr_2CrWO_6 [1] are suitable candidates due to the theoretically predicted high spin polarization and a Curie-temperature well above room temperature [2]. Furthermore, in the double perovskite Sr_2FeMoO_6 the Curie-temperature has been increased by substitution of the divalent Sr^{2+} by trivalent La^{3+}, i.e. by electron doping [3]. On the other hand, in Sr_2CrWO_6 the same substitution has been reported [4] to lead to a clear decrease of T_C. With respect to the mechanism of ferromagnetism in the double perovskites, it is of interest to resolve this controversy. Moreover, it is known that the Curie-temperature and the saturation magnetization of double perovskites depend strongly on structural and disorder effects. In order to study these effects in detail, we have fabricated a series of polycrystalline samples of La-doped and isovalent substituted $A_{2-x}La_xCrWO_6$ (A = Ca, Sr) compounds. All samples were characterized by x-ray powder diffraction, neutron scattering, as well as magnetization and transport measurements.

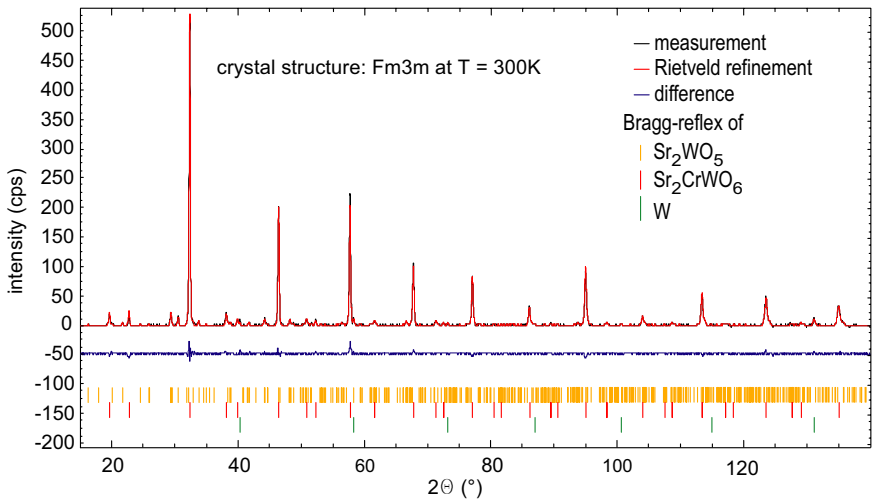

Figure 1: Powder x-ray diffraction measurement of Sr_2CrWO_6 and Rietveld refinement. The crystal structure is the ideal cubic $Fm\bar{3}m$ symmetry at room temperature.

Ceramic samples have been synthesized by a solid state reaction described in [2]. As the whole process is not performed in evacuated silica tubes, one can assume that due to the relatively high volatility of chromium oxide our samples are slightly Cr deficient. A deviation from the ideal 1:1 ratio of Cr and W obviously influences the magnetic properties. On the other hand, this might be compensated by the fact that only W oxide parasitic phases are detected.

Fig. 1 shows a powder x-ray diffraction measurement and a simulation with the Rietveld method of the undoped Sr_2CrWO_6 sample. Residual parasitic phases of Sr_2WO_5 and W are present. In a phase analysis we obtain 91% of the main Sr_2CrWO_6 phase, 7.7% of Sr_2WO_5, and 1.3% of W. In the La-doped compounds the amount of these parasitic phases is much higher

[1] This work is supported by the Deutsche Forschungsgemeinschaft within the coordinated program SPP 1157 (project no. GR 1132/13-1).

than in the undoped Sr_2CrWO_6 sample due to the formation of $LaCrO_3$. That is, the preferential formation of $LaCrO_3$ prevents the desired formation of $Sr_{2-x}La_xCrWO_6$. Further evidence for this comes from energy dispersive x-ray (EDX) analysis. The major part of randomly chosen microcrystals seems to consist of a mixture of $LaCrO_3$ and a $Sr_2Cr_{1-x}W_{1+x}O_6$ phase with reduced Cr content. We consider that this Cr deficiency is the main reason of the T_C reduction in the La doped $Sr_{2-x}La_xCrWO_6$ samples shown in Fig. 2(a). Another indication is the development of the lattice parameter of $Sr_{2-x}La_xCrWO_6$ as a function of La doping. For successful doping, a change of the lattice parameter is expected [3] both due to electronic and steric effects. We find that the lattice constant in the $Sr_{2-x}La_xCrWO_6$ samples remains constant (after a slight initial drop) as a function of doping [5]. This is strong indication that the La-doped compound does not form. Therefore, the reduction of the Curie-temperature T_C is an *ex*trinsic effect [5].

In contrast to the Sr_2CrWO_6 material system La doping can be achieved in the compound Ca_2CrWO_6. Fig. 2(b) shows that the Curie-temperature T_C is increased as a function of La doping as it is the case for $Sr_{2-x}La_xFeMoO_6$. These results prove the fact that electron doping in the double perovskites is a way to increase the ferromagnetic transition temperature and pave the way to obtain materials with even higher Curie temperatures.

From band structure calculations one can estimate the limit of this electron doping. Unfortunately, the number of La-ions needed to destabilize ferromagnetism in the double perovskites is about the limit that can be doped without destabilizing the crystal structure. Therefore it is difficult at present to use the current experiments to validate theoretical models of magnetism in double perovskites.

Furthermore, La doping is associated with lattice distortions and increased anti-site disorder. In order to study these effects in more detail, neutron powder diffraction experiments were carried out in the high-intensity powder diffractometer D20 at the Institute Laue Langevin in Grenoble. The new high take-off angle option of the diffractometer was used giving high neutron flux and high resolution at the same time. Neutron powder diffraction certainly is the most straightforward tool to determine the magnetic structure of polycrystalline samples.

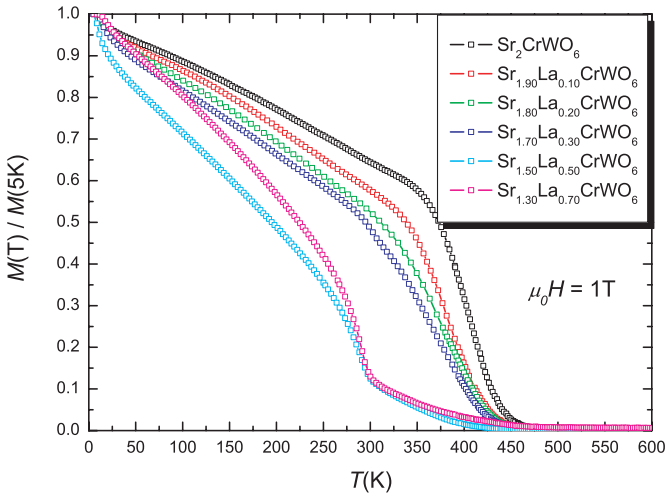

(a) $Sr_{2-x}La_xCrWO_6$

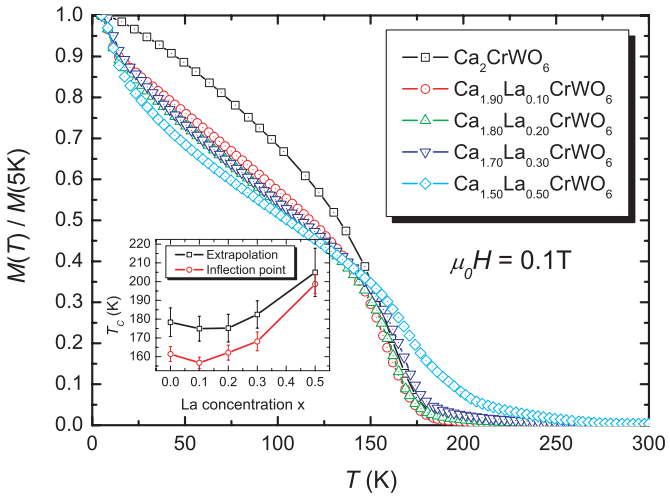

(b) $Ca_{2-x}La_xCrWO_6$

Figure 2: Normalized magnetization of $Sr_{2-x}La_xCrWO_6$ and $Ca_{2-x}La_xCrWO_6$ for different La concentration. The inset shows directly the Curie-temperature T_C versus the La concentration x. Two different methods have been used to determine the Curie-temperature T_C: linear extrapolation of the magnetization to zero and a determination of the inflection point.

Neglecting the weak temperature dependence of the Debye-Waller factor, only the magnetic scattering depends strongly on temperature, and of course vanishes at T_C. Fig. 3(a) shows the intensity of the magnetic and nuclear (111) reflection of the Sr_2CrWO_6 phase as a function of temperature from neutron diffraction. The predominantly nuclear scattering at the (200) reflection depends only weakly on temperature. From the magnetic scattering pattern shown in Fig. 3(a) the magnetization of the sample can be calculated. The result is plotted in Fig. 3(b).

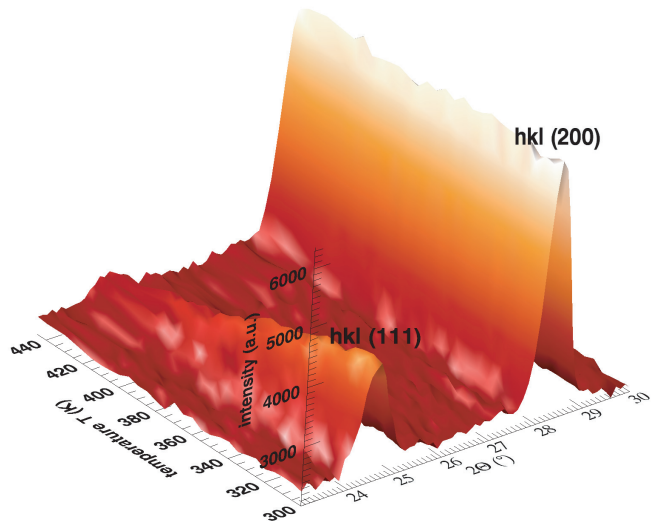

(a) Intensity as a function of temperature and diffraction angle

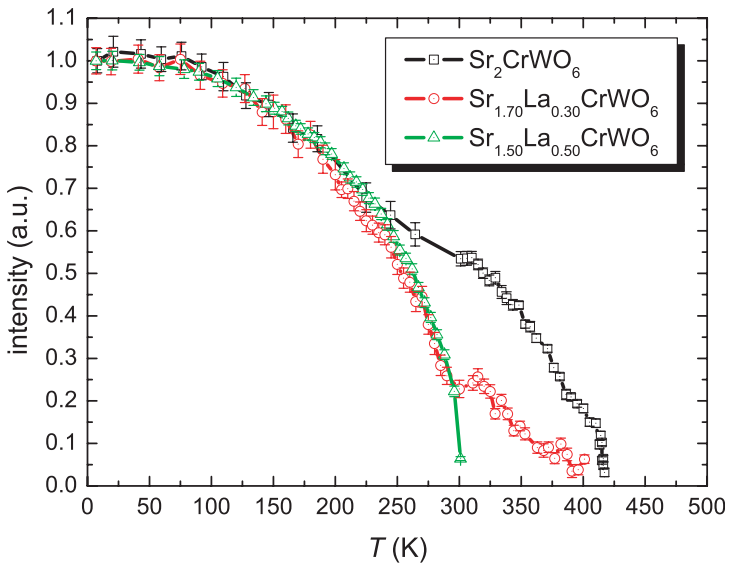

(b) Intensity of the (111) reflection as a function of temperature for different La concentrations.

Figure 3: Neutron powder diffraction from $Sr_{2-x}La_xCrWO_6$ samples with different La concentration.

It is interesting to note that there seem to be two different transition temperatures: One located at 300 K, and one around 420 K. When we compare the magnetization from the SQUID measurement to the neutron data, we observe a strong deviation in the relative magnetic signals. While in the SQUID data the magnetization *de*creases with increasing the La content, the neutron signal indeed *in*creases. This fact indicates that an additional antiferromagnetic phase was detected by neutron diffraction. Furthermore, the amount of this antiferromagnetic correlations increases with higher La concentration. To explain this effect, we have to consider anti-site defects, which lead to Cr and W pairs. We believe that the magnetic scattering from this antiferromagnetic phase originates from antiferromagnetic coupling between neighboring Cr cations via Cr-O-Cr paths, which is the case in anti-site defects. The transition temperature of this antiferromagnetic phase (nearly 300 K) indicates, that the Cr-O-Cr magnetic interaction are by far more similar to those present in the antiferromagnetic $LaCrO_3$ ($T_N = 290$ K) perovskite than in the paramagnetic $SrCrO_3$. The delocalized W electron assures the charge neutrality across the crystal, keeping the nominally trivalent valence for Cr. Increased La content leads to an increased number of antisite defects and to an enhancement of the antiferromagnetic coupling of the Cr pairs.

This observation is a verification of the antiferromagnetic coupled Cr pairs due to superexchange via Cr-O-Cr paths reported in [6] which lead to a reduction of the saturation magnetization. In agreement with our observation, Monte Carlo calculations predicted that disorder may lead to antiferromagnetic coupling between neighboring Cr pairs, instead of ferromagnetic coupling proposed for an ideal crystal [7].

In summary, we have studied the electron doping and the structural effects of the ferromagnetic double perovskite Sr_2CrWO_6. We have shown that electron doping generically increases T_C as demonstrated in the system $Ca_{2-x}La_xCrWO_6$ and $Sr_{2-x}La_xFeMoO_6$. As the limit for this electron doping has not yet been reached there is plenty of room for pushing the limits further for the critical temperatures in ferromagnetic double perovskite systems. This result is promising with respect to the potential application of the double perovskites in spintronic devices, where half-metallic materials with high T_C values are required.

References

[1] J.B. Philipp, D. Reisinger, M. Schonecke, A. Marx, A. Erb, L. Alff, and R. Gross, Appl. Phys. Lett. **79**, 3654 (2002).
[2] J.B. Philipp, P. Majewski, L. Alff, A. Erb, R. Gross, T. Graf, M.S. Brandt, J. Simon, T. Walther, W. Mader, D. Topwal, and D.D. Sarma, Phys. Rev. B **68**, 144431 (2003).
[3] J. Navarro, C. Fontera, Ll. Balcelss, B. Martínez, and J. Fontcuberta, Phys. Rev. B **64**, 092411 (2001).
[4] J.B. Philipp, P. Majewski, D. Reisinger, S. Gepraegs, M. Opel, A. Erb, L. Alff, R. Gross, Acta Physica Polonica A **105**, 7 (2004).
[5] S. Gepraegs, P. Majewski, M. Opel, A. Erb, L. Alff, R. Gross, C. Ritter, J. Simon, and W. Mader, to be published
[6] J. Navarro, Ll. Balcelss, F. Sandiumenge, M. Bibes, A. Roig, B. Martínez, and J. Fontcuberta, J. Cond. Mat. **13**, 8481 (2001).
[7] C. Frontera, and J. Fontcuberta, Phys. Rev. B **69**, 014406 (2004)

Effect of Rare Earth Ion Substitution on the Magnetic and Transport Properties of $Pr_{0.7}RE_{0.04}Sr_{0.26}MnO_3$ (RE = Er^{3+}, Tb^{3+}, Ho^{3+})

N. Rama[a,b], J.B. Philipp, M. Opel, A. Erb, V. Sankaranarayanan[b], M.S. Ramachandra Rao[a,b], and R. Gross [1]

[a] Materials Science Research Centre, Indian Institute of Technology Madras, Chennai - 600 036, India

[b] Department of Physics, Indian Institute of Technology Madras, Chennai - 600 036, India

The perovskite type Colossal Magnetoresistive (CMR) manganites of general composition $RE_{1-x}A_xMnO_3$, where RE is a rare earth ion and A is a divalent alkaline earth ion, exhibit an unusually strong interplay between orbital, lattice and spin degrees of freedom. At temperatures below their Curie temperature (T_C), optimally substituted ($x = 0.3 \ldots 0.4$) manganites are ferromagnetic metals, while at higher temperatures, i.e. above T_C, they exhibit a paramagnetic insulating behavior [1]. This generic behavior, as well as the large magnetoresistive effect which occurs near the metal-insulator transition (MIT), has been explained within the framework of the Zener double exchange (ZDE) model [2, 3]. In this model, the creation of mixed valency of Mn (Mn^{3+}/Mn^{4+}) by hole doping at the rare-earth (RE) site plays an important role. The transfer (hopping) of an e_g electron between the neighboring Mn^{3+} and Mn^{4+} ions through the Mn-O-Mn path, results in an effective ferromagnetic interaction due to strong on-site Hund's coupling.

When the parent compound $LaMnO_3$ is doped with aliovalent alkaline earth ions (valency 2+) like Ca^{2+}, Sr^{2+}, etc. on the A-site, the carrier concentration as well as the average A-site ionic radius changes. On the other hand when isovalent rare earth ions (valency 3+) like Er^{3+}, Tb^{3+}, or Y^{3+} are substituted on the A-site, only the average A-site ionic radius changes. This change affects the ferromagnetic exchange which causes a change in the ferromagnetic transition temperature as well as the resistivity and magnetoresistance [4, 5]. The above scenario is related to the change of the tolerance factor t and the increase in A-site disorder causing a tilt and/or rotation of the oxygen octahedra around the Mn ions. This in turn results in a change of the Mn-O-Mn bond angles away from 180° and hence a reduction of the hopping matrix element of the e_g electrons and narrowing of the effective electronic bandwidth [6, 7, 8, 9]. The average A-site disorder is characterized by a parameter $\langle\sigma^2\rangle$ given by [10]

$$\langle\sigma^2\rangle = \sum_i y_i r_i^2 - (\sum_i y_i r_i)^2 \quad (1)$$

where r_i is the ionic radii of the A site ion of concentration y_i.

In our recent work [11], we have shown that the substitution of La^{3+} by Ho^{3+} and Y^{3+} in $La_{0.7}Ca_{0.3}MnO_3$ (LCMO) yields interesting results. Upon substitution of Ho^{3+} ions at the La-site in LCMO, the resistivity decreases dramatically compared to that of Y^{3+} substituted LCMO for similar concentration levels. Ho^{3+} and Y^{3+} ions have the same ionic radii and hence, the observed change in resistivity for the same concentration of the dopant was attributed to the magnetic nature of the Ho^{3+} ion. Magnetization studies unequivocally proved an increase in magnetic moment per formula unit in the Ho^{3+} substituted compounds indicating a coupling between the Ho^{3+} and $Mn^{3+/4+}$ moments.

[1] This work was done within a German-Indian science and technology cooperation project funded by the BMBF (project IND 01/009).

Table 1: Lattice parameter, average A site disorder, maximum resistivity value, activation energy (from high temperature fits) and the low temperature fit parameters; non-sub: non-substituted; Tb^{3+}sub: Tb^{3+} substituted sample; Ho^{3+}sub: Ho^{3+} substituted sample and Er^{3+}sub: Er^{3+} substituted sample.

Compound	a (Å)	$\langle\sigma^2\rangle$ (10^{-3} Å^2)	ρ_{max} (Ωcm)	E_A (eV)	p	ρ_{LT} (Ωcm)
non-sub PSMO(0.26)	3.87	3.66	1.00	0.14	2.56	0.02
Tb^{3+}sub	3.86	4.06	15.14	0.15	3.58	0.47
Ho^{3+}sub	3.86	4.34	18.74	0.19	3.24	0.75
Er^{3+}sub	3.86	4.44	312.76	0.21	3.40	9.87

Here, we present the effect of the substitution of Er^{3+}, Ho^{3+}, and Tb^{3+} ions on the magnetic properties of $Pr_{0.74}Sr_{0.26}MnO_3$ (PSMO(0.26)), which already has a magnetic ion (Pr^{3+}) in its lattice [12]. Since within the framework of the ZDE model the Mn^{4+} concentration is one of the factors that determines T_C, we have substituted the PSMO(0.26) system such that the resulting compounds have the same Mn^{4+} concentration, but differ with respect to their $\langle\sigma^2\rangle$ values (see Tab. 1).

In order to exclusively study the effect of A-site disorder on magnetic and electrical transport properties, it is desirable that the tolerance factor of the RE-substituted PSMO(0.26) compositions is kept constant. This was achieved in the following way. The tolerance factor t of $Pr_{0.7}Er_{0.04}Sr_{0.26}MnO_3$ was calculated (0.917) and the concentrations of the other two substituents (Ho^{3+} and Tb^{3+}) were adjusted such that all three RE-substituted PSMO compositions had the same tolerance factor equal to $t = 0.917$. Thus, the nominal compositions of the (Ho^{3+} and Tb^{3+}) are $Pr_{0.699}Ho_{0.041}Sr_{0.26}MnO_3$ and $Pr_{0.697}Tb_{0.043}Sr_{0.26}MnO_3$, respectively. Polycrystalline samples of these compounds were prepared along with the non-substituted PSMO(0.26) ($t = 0.919$) composition by the conventional solid-state method. Stoichiometric amounts of preheated Pr_6O_{11}, Er_2O_3, Ho_2O_3, Tb_4O_7, $SrCO_3$, and MnO_2 were weighed and mixed thoroughly in an agate mortar and calcined in an alumina crucible at 950°C for 24 h. The calcined powders were reground and heated again at 1250°C for another 24 h. The resultant powder was then pressed into pellets of 10 mm diameter and sintered in air at 1350°C for 24 h.

X-ray diffraction (XRD) of the samples was performed using Cu-K_α radiation and a two-circle diffractometer (Rich-Seifert). The diffraction patterns of the samples showed a pseudo-cubic structure [12]. The corresponding lattice constants are listed in Table 1.

The electrical resistivity of the samples was measured in the standard linear four-probe technique in the temperature range of 2 . . . 400 K using an Oxford continuous flow cryostat. The temperature dependence of electrical resistivity of the four samples showed the metal-insulator transition (MIT), a characteristic feature of the substituted manganites, for all samples (Fig. 1). Furthermore, it is evident that all RE substituted samples show much higher resistivity

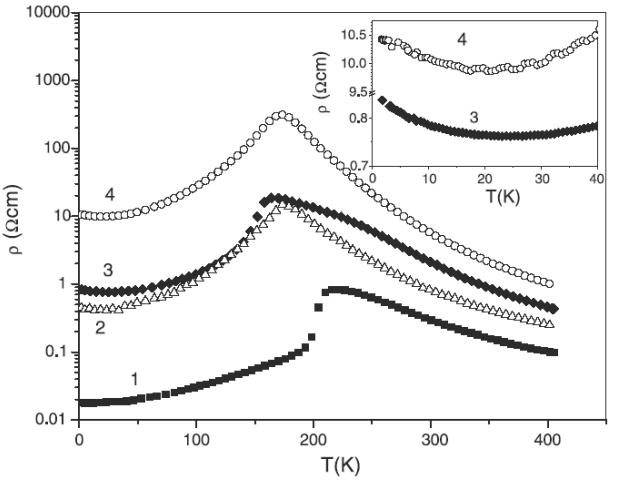

Figure 1: Resistivity versus temperature curves for $Pr_{0.74}Sr_{0.26}MnO_3$ (1) and $Pr_{0.7}RE_{0.04}Sr_{0.26}MnO_3$ (RE = Tb(2), Ho(3), and Er(4)). The inset shows the low temperature resistivity upturn in Ho^{3+} and Er^{3+} substituted samples.

over the entire temperature range compared to non-substituted PSMO(0.26). We find that the resistivity value at the maximum (corresponding to a temperature referred to as T_P) in the resistivity versus temperature curve of the substituted samples is largest for the Er^{3+} substituted PSMO(0.26) (maximum $\langle\sigma^2\rangle$), and lowest for the Tb^{3+} substituted PSMO (0.26) sample (minimum $\langle\sigma^2\rangle$) thus scaling with A-site disorder as calculated using equation (1) (Tab. 1). The sharp drop in the resistivity with temperature that is observed for the pure PSMO(0.26) just below the MIT is absent in the substituted samples. This suggests that the MIT in the substituted samples is much more gradual than in the pure sample. This gradual transition may occur due to the onset of percolative transport behavior [13]. At temperatures above T_P, the temperature dependence of resistivity can be described within the adiabatic polaron hopping model [14]

$$\rho(T) = \rho_0(T)\exp(\frac{E_A}{k_B T}). \tag{2}$$

The values of activation energy (E_A) obtained for various substituted compounds by fitting the experimental data with equation (2) (tab. 1) is found to increase with increase in A-site disorder [12].

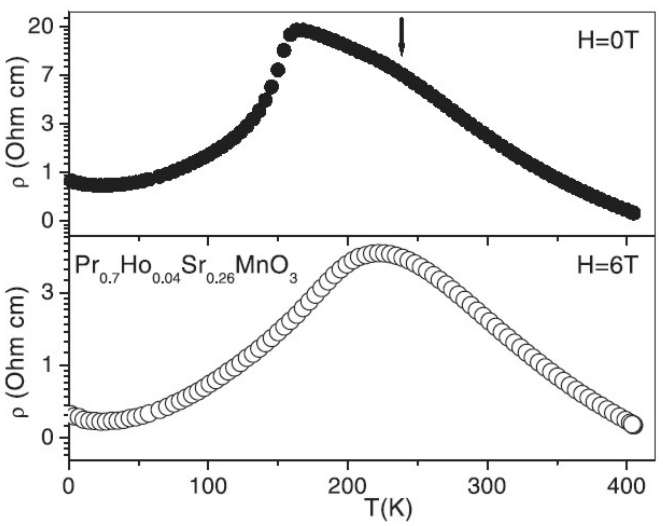

Figure 2: Resistivity at 0 T (upper panel) and at 6 T (lower panel) for $Pr_{0.7}Ho_{0.04}Sr_{0.26}MnO_3$ sample. The kink in the resistivity is indicated by the arrow. It is seen that the kink is suppressed on application of a magnetic field possibly pointing towards its magnetic origin.

It is interesting to note that among the rare earth substituted compounds, the fitting range (274 . . . 400 K) is lower for $Pr_{0.7}Ho_{0.04}Sr_{0.26}MnO_3$ substituted sample than that (248 . . . 400 K) for the $Pr_{0.7}Tb_{0.04}Sr_{0.26}MnO_3$ substituted sample due to the presence of a kink in the high temperature resistivity (marked by a vertical arrow in figure 2 in the plot corresponding to the $Pr_{0.7}Ho_{0.04}Sr_{0.26}MnO_3$ data). It is observed that this kink is suppressed upon application of a magnetic field (Fig. 2) pointing to the presence of magnetic correlations even above T_C for the Ho^{3+} sample.

All the samples show a minimum in low temperature resistivity around 30 K. The upturn below 30 K was found to be insensitive to the substitutions at the rare earth ion site and occurs more or less at the same temperature in all the samples including the non-substituted compound. This behavior could be due to intergranular tunneling between grains [15, 16]. The low temperature dependence of the resistivity could be fitted to an expression of the form

$$\rho(T) = \rho_{LT} + \rho_1 T^p \tag{3}$$

from 40 K to 100 K [12]. It is seen that the exponent p is higher for the substituted samples as compared to the non-substituted samples (Tab. 1). For the non-substituted sample p is found to be 2.5, which is usually observed for conventional manganites and is attributed to half-metallic behavior [17, 18]. However, for the substituted samples we obtain an exponent ranging between 3 . . . 4. This suggests a more complex nature of the electrical transport in the RE substituted samples. It is also seen that the fitting parameter ρ_{LT} increases with increase in A-site disorder (see Tab. 1).

Magnetization measurements were carried out using a SQUID magnetometer in the temperature range of 2 . . . 400 K in a field cooled mode of 1000 Oe. Fig. 3 shows the M versus T plots for all the four samples. It is seen that the $M(T)$ curves show a minimum around 60 K, which is attributed to the Pr^{3+} sublattice ordering induced by the molecular field of Mn ions [19] as seen from neutron diffraction [20]. However, in the Er^{3+} substituted PSMO(0.26) sample the magnetization minimum is not seen even though it is clearly seen in the Ho^{3+} substituted sample although they have comparable $\langle\sigma^2\rangle$ values. Below 25 K, it is seen that the magnetization of the Ho^{3+} substituted sample and the Er^{3+} substituted sample increases while that of the Tb^{3+} substituted sample decreases (inset in Fig. 3). A similar behavior is also seen in $La_{0.625}Ho_{0.075}Ca_{0.3}MnO_3$ [11] and Tb^{3+} and Ho^{3+} doped $Pr_{0.7}Sr_{0.3}MnO_3$. Hence, this behavior may be attributed to the polarization of the magnetic rare earth sublattice induced by the molecular field of Mn ions. The decrease in magnetization observed in the Tb^{3+} substituted compound may also be due to the magnetic anisotropy of Tb usually observed at low temperatures [21] or due to a canting of Mn spins as observed in $Nd_{0.7}Sr_{0.3}MnO_3$ [22].

From the discussion above, it is seen that although the peak resistivity values of all the samples scale with $\langle\sigma^2\rangle$, the resistivity of the Ho^{3+} substituted sample is nearly the same as that of the Tb^{3+} substituted sample even though it has higher A-site disorder. This observation together with the presence of the kink in the high temperature resistivity for the Ho^{3+} substituted sample alone, possibly due to the existence of magnetic clusters above T_C, suggests an anomalous behavior of the Ho^{3+} substituted sample. Recent high field magnetization measurements have revealed a coupling between the moments of the Ho and Mn ions [11] in $La_{0.7}Ca_{0.3}MnO_3$. Moreover, neutron diffraction measurements show that Pr moments order ferromagnetically, possibly due to a coupling between Pr and Mn moments [20, 22]. This coupling may be weakened by the increase in A-site disorder (higher $\langle\sigma^2\rangle$) as suggested by the absence of the magnetization minimum around 60 K for the Er^{3+} substituted sample. The magnetization minimum however, is observed in the Ho^{3+} substituted sample though it has a $\langle\sigma^2\rangle$ comparable to that of the Er^{3+} substituted sample. In this case the effect of A-site disorder may be offset by the tendency of Ho moments to couple with those of Mn [12].

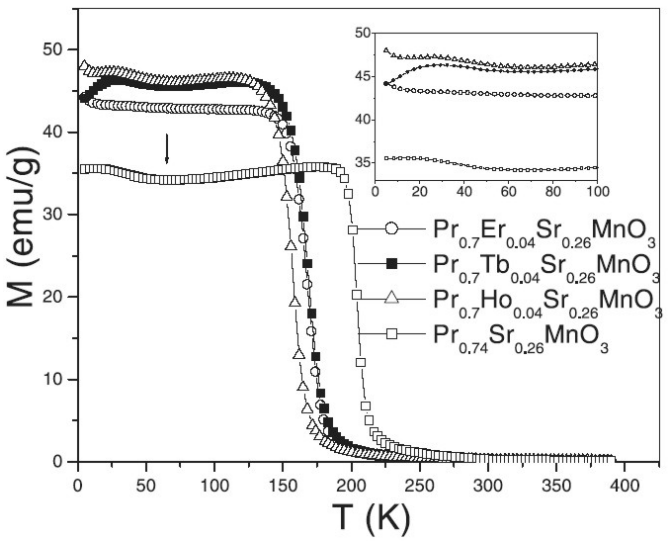

Figure 3: Temperature dependence of magnetization in a field of 1000 Oe. The arrow indicates the onset of Pr sublattice ordering induced by the molecular field of Mn. Inset shows the low temperature $M(T)$ curves.

References

[1] R. von Helmolt, J. Wecher, B. Holzapfel, L. Schultz, K. Samwer, Phys. Rev. Lett. **71**, 2331 (1993).
[2] C. Zener, Phys. Rev. B **82**, 403 (1951); P.-G. de Gennes, Phys. Rev. **118**, 141 (1960).
[3] P.W. Anderson, H. Hasegawa, Phys. Rev. **100**, 675 (1955).
[4] C.N.R. Rao, A.K. Cheetham, R. Mahesh, Chem. Mater. **8**, 2421 (1996).
[5] A.P. Ramirez, J. Phys: Condens. Matter **9**, 8171 (1997).
[6] H.Y. Hwang, S.-W. Cheong, P.G. Radaelli, M. Marezio, B. Batlogg, Phys. Rev. Lett. **75**, 914 (1995).
[7] J.R. Sun, G.H. Rao, J.K. Liang, Appl. Phys. Lett. **70**, 1900 (1997).

[8] J. Fontcuberta, B. Martinez, A. Seffar, S. Pinol, J.L. Garcia-Munoz, X. Obradors, Phys. Rev. Lett. **76**, 1122 (1996).
[9] Z.B. Guo, N. Zhang, W.P. Ding, W. Yang, J.R. Zhang, Y.W. Du, Solid State Commun. **100**, 769 (1996).
[10] L.M. Rodriguez-Martinez, P. Attfield, Phys. Rev. B **54**, R15622 (1996).
[11] V. Ravindranath, M.S. Ramachandra Rao, G. Rangarajan, Yafeng Lu, J. Klein, R. Klingeler, S. Uhlenbruck, B. Büchner, R. Gross, Phys. Rev. B **63**, 184434 (2001).
[12] N. Rama, J.B. Philipp, M. Opel, A. Erb, V. Sankaranarayanan, R. Gross, and M.S. Ramachandra Rao, Eur. Phys. J. B **38**, 553 (2004).
[13] E. Dagotto, H. Takashi, A. Moreo, Phys. Rep. **344**, 1 (2001).
[14] T. Holstein, Ann. Phys. **8**, 343 (1959).
[15] E. Rozenberg, M. Auslender, I. Felner, G. Gorodetsky, J. Appl. Phys. **88**, 2578 (2000).
[16] M.I. Auslender, E. Rozenberg, A.E. Karkin, B.K. Chaudhuri, G. Gorodetsky, J. Alloys Compounds **326**, 81 (2001).
[17] X. Wang, X.G. Zhang, Phys. Rev. Lett. **82**, 4276 (1999)
[18] P. Schiffer, A.P. Ramirez, W. Bao, S.-W. Cheong, Phys. Rev. Lett. **75**, 3336 (1995).
[19] J.G. Park, M.S. Kim, H.-C. Ri, K.H. Kim, T.W. Noh, S.-W. Cheong, Phys. Rev. B **60**, 14804 (1999).
[20] Z. Jirak, S. Vratislav, J. Zajicek, phys. stat. sol. (a) **52**, K39 (1979).
[21] *Ferromagnetic Materials*, edited by E.P. Wohlfarth, Vol. 1 (North-Holland, 1980).
[22] Junghwan Park, M.S. Kim, J.-G. Park, I.P. Swainson, H.-C. Ri, H.J. Lee, K.H. Lee, K.H. Kim, T.W. Nohm, S.W. Cheong, Changhe Lee, J. Korean Phys. Soc. **36**, 412 (2000).

The Persistent-Current Quantum-Bit in a Microwave Cavity

M. Mariantoni, M. J. Storcz, W. D. Oliver, F. K. Wilhelm, A. Marx, and R. Gross [1]

The symbiosis of cavity-Quantum-ElectroDynamics (cQED) [1, 2] and superconducting Quantum-Bits (QuBits) [3, 4] has gained great interest lately [5, 6]. In this report the basic elements for realizing a cQED experiment making use of superconducting devices will be presented and analyzed. In section I some of the main reasons why cQED is a more advantageous scheme compared to existing read-out and control architectures will be summarized. In section II a brief introduction to cQED will be given. The Persistent-Current (PC) QuBit will be introduced in section III and the Microwave-Cavity (MC) in section IV. section V will be devoted to a short analysis of the QuBit-MC interaction. The final remarks and outlook will be presented in section VI.

I: cQED as a Favourable Measurement Tool

Realizing a cQED experiment would provide a deeper understanding of the concept of quantum measurement [7] (as it will be shown in the next section), giving rise to a number of novel experimental and theoretical investigations within the field of superconducting QuBits. Besides the possibility for a single-shot read-out of the state of the QuBit, it would be feasible to perform Quantum-Non-Demolition (QND) measurements (for more details see [8]).

The MC will provide an excellent protection of the QuBit from its environment, filtering out most of the noise due to the bosonic-heat bath (see [8]), which is the predominant source for energy relaxation in the system. Moreover, since both the QuBit and the MC will be operated in the superconducting state, the generation of quasi-particles - a well known source of dephasing in superconducting QuBits - will be strongly suppressed. This should certainly decrease the non-radiative decay rate of the PC-QuBit. As a consequence, useful information on other dephasing channels could be gained.

A possible drawback of a cQED experiment with PC-QuBits has to be mentioned here. As it will be shown in section III, the window for high polarizability of a PC-QuBit is quite limited. Therefore, the region for operating the system is not very wide [8].

II: A Brief Introduction to the Field of cQED

A fundamental process in nature is the interaction between matter and light. This process can be practically realized in an optical or microwave cavity where a single atom interacts with a single photon. In the last decade, many experimental and theoretical efforts have been pursued in this direction, particularly in quantum optics, enriching the already stimulating field of cQED.

In order to understand the working principle of cQED, it is worthwhile making a *Gedanken* experiment. An atom is produced in an oven (in reality several atoms are usually produced, but for the sake of simplicity only one of them will be taken into account for here). In quantum optics the atoms typically used are alkali atoms (like cesium) or circular Rydberg atoms (like rubidium). For the experiment proposed in this report an artificial two-level system will play the

[1] This work has been done in collaboration with the Ludwig-Maximilians-Universität München and MIT Lincoln Laboratory. This work is supported by the Deutsche Forschungsgemeinschaft through SFB 631.

role of the atom, more precisely a three-Josephson-Junctions PC QuBit. The atom considered in this *Gedanken* experiment can be assumed to be characterized by two energy levels only, the ground-state $|g\rangle$ and the excited state $|e\rangle$. The $|g\rangle$-$|e\rangle$ transition will be called Ω (here, and in all the rest of this discussion, the transition is defined as the energy gap between the two levels divided by $\hbar$). The time within which the atom decays from its excited state to its ground-state will be equal to a quantity $1/\gamma$, called atomic lifetime, which simply represents the decay rate associated with energy relaxation.

The atom is then directed into a cavity (which can be an optical cavity, a 3D MC, or a planar on-chip circuit resonator). It is possible to regard the cavity as a quantum harmonic oscillator with transition ω_0. If the black-body radiation from the environment is negligible and no field is driven into the cavity, the quantum harmonic oscillator will be in its ground-state $|0\rangle$ (also called vacuum state). The decay rate associated with the cavity (the cavity lifetime) will be $1/\kappa$ and will strongly depend on the cavity quality factor.

At some point the atom will pass through the cavity and interact with it. Two distinguished regimes are possible. Interaction on resonance, meaning the atom and the cavity transitions are equal ($\Omega = \omega_0$), or interaction off resonance, meaning atom and cavity are detuned by a quantity Δ (where $\Delta = \Omega - \omega_0$). The two different regimes will be discussed in more detail in section V. Here, only the on resonance case will be further analyzed, whereas just a few words will be spent for the off resonance one.

Assuming for simplicity that the transit time of the atom through the cavity is very long compared to all the other characteristic time scales of the system, it is possible to regard the atom statically positioned inside the cavity. In the case $\Omega = \omega_0$ the atom will decay into its ground-state after some time (which is not directly related to its lifetime!) emitting a photon with energy $\hbar\Omega$ if it is initially in the excited state. On resonance, the decay is strongly enhanced since the atom can easily emit a photon, which will then be rapidly absorbed by the cavity. If the atom and the cavity lifetimes are not too short (γ and κ are small enough), the photon will eventually re-excite the atom to $|e\rangle$. This process (a non-relativistic quantum-electrodynamics) will keep on going at a rate which is called vacuum Rabi frequency and is indicated with g. Summarizing, g/π is the frequency (in Hz) at which the atom-cavity entangled state $(g, 1)$ is changed into the entangled state $(e, 0)$, where $|0\rangle$ and $|1\rangle$ represent zero or one photon in the cavity, respectively.

It is worth stressing that $\gamma/2$, $\kappa/(2\pi)$, and g/π are all measured in hertz and can thus be compared. In particular, it is easy to figure out that the interesting regime requires that $g/\pi \gg (\gamma/2; \kappa/(2\pi))$. In this case it is possible to observe several Rabi flops before the atom relaxes or the photon is emitted out of the cavity.

Off resonance (the important case actually is when $g/\Delta \ll 1$, *i.e.* large detuning) it is clear that an atom in the excited state will not easily decay into its ground-state because of the large detuning with respect to the cavity. Thus, the atom lifetime will be thus strongly enhanced (this phenomenon is known as Purcell effect).

III: The PC-QuBit: An Artificial Two-Level System

The atom or, being more precise, the artificial two-level system that has been chosen for the experiment proposed in this report is the so called PC-QuBit. Superconducting PC-QuBits have been introduced and studied for the first time by J.E. Mooij *et al.* [4] in 1999. In these flux-based circuits small a superconducting loop is interrupted by three Josephson junctions (see Fig. 1). Typically, the geometric self-inductance of the loop is of the order of 10-50 pH. The Josephson

junctions usually have areas of a few hundred nanometers squared and critical currents below 1 μA.

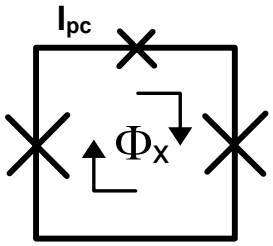

Figure 1: A three Josephson junction PC-QuBit.

With this architecture it is possible to shape the potential landscape of the QuBit during fabrication making one of the three junctions smaller than the other two by a factor α. Neglecting the potential energy contribution due to the small self-inductance of the loop, and considering low temperature (the QuBit is typically cooled down below 100 mK), it is possible to show (see Ref. [4]) that the PC-QuBit is characterized by a double-well potential, where only the two lowest states of each well are populated. In the rest of this report these two states will be referred to as $|L\rangle$-state and $|R\rangle$-state, respectively. These Left and right states correspond to clockwise or counterclockwise persistent circulating currents in the superconducting loop. Thus, a PC-QuBit can also be regarded as a pseudo-spin up or down system. Its Hamiltonian reads

$$\hat{H}_q = \frac{\hbar\Omega}{2}\hat{\sigma^z}\ , \tag{1}$$

where σ^z is the Pauli matrix in the z-direction with eigenvalues ± 1. This Hamiltonian is written in the $|L\rangle$ and $|R\rangle$ basis. Each of these two up or down states is characterized by a certain magnetic dipole moment, μ_q. To gain further insight, it is convenient to look at the energy eigenvalues of the system

$$E_\pm = \pm\sqrt{(\hbar\Omega)^2 + \left[I_{pc}\left(\Phi_x - \frac{1}{2}\Phi_0\right)\right]^2}\ , \tag{2}$$

where I_{pc} is the persistent circulating current flowing in the loop, Φ_x is the external applied magnetic flux (which can be used to change the state of the QuBit and bias it at the most desirable point), and Φ_0 is the flux quantum. The first derivative of the energy eigenvalues with respect to Φ_x gives the mean value of I_{pc}, $\langle I_{pc}\rangle$. The second derivative represents the difference in flux polarizability of the PC-QuBit. The mean value of the persistent circulating current and the difference in polarizability are plotted as a function of Φ_x in figs. 2 and 3, respectively.

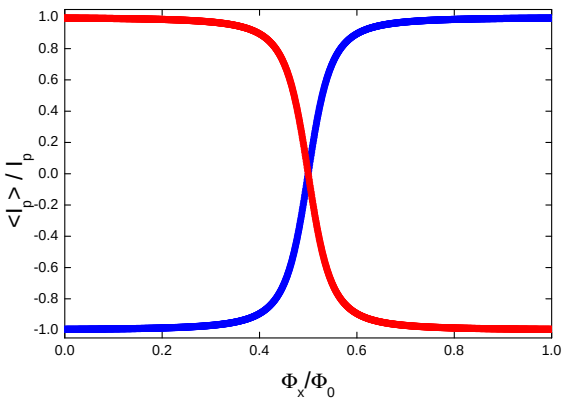

Figure 2: The mean value of the persistent circulating current plotted as function of Φ_x.

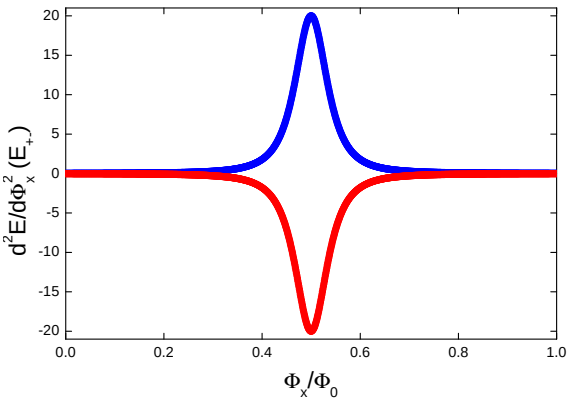

Figure 3: The difference in polarizability for a PC-QuBit plotted as function of Φ_x.

In Ref. [8] the maximal difference in flux polarizability for the PC-QuBit (which is also related to its magnetic dipole moment μ_q) is calculated in detail. From fig. 3 it is clear that this maximal value is obtained right at the degeneracy point (*i.e.* for a value of $\Phi_x = (1/2)\Phi_0$). It is also clear that the polarizability, and thus μ_q, drastically drops moving away from the degeneracy point. This is the main drawback of using a PC-QuBit as an artificial two-level system for cQED experiments. In fact the polarizability directly enters the expression for the coupling strength g (see section V). On the other hand, a PC-QuBit has many favorable features (*e.g.*, large decoherence times, possibility of shaping the tunneling amplitude - namely the potential landscape - at will during fabrication, and so forth) which make it very attractable for this kind of experiments. In particular, the typical energy relaxation rate of a PC-QuBit, $\gamma/2$, has been found to be between 0.5 and 1 MHz ([9]), meaning that the QuBit lifetime can be pretty large.

IV: The Microstrip Resonator: An on-Chip Cavity

The second "ingredient" for realizing a cQED experiment is a microwave cavity. For this discussion the so called Microstrip-Resonator (MR) will be analyzed. Figure 4 shows a possible MR (this picture has been taken from Ref. [10]). In this architecture, both ground-plane and top strip-line are made of superconducting materials - like Aluminum or Niobium. Si or SiO_x can be used as dielectric substrate. The ground-plane is fabricated in a square-washer geometry with a slit (see Ref. [10]). The length of the top strip-line sets the wavelength of the electromagnetic wave standing in the resonator, thus fixing its resonance frequency (of course the resonator will have several modes, but in this report only the first mode will be considered). In the real experiment the resonance frequency will be of the order of 10 GHz, and it will be tuned *in situ* by means of a mechanically adjustable screw placed on top of the chip or a piezoelectric device positioned at the input of the resonator. The MR can also be utilized for dc flux-biasing any device placed into it using input and output bias tees (for technical details about the bias tees see [8]).

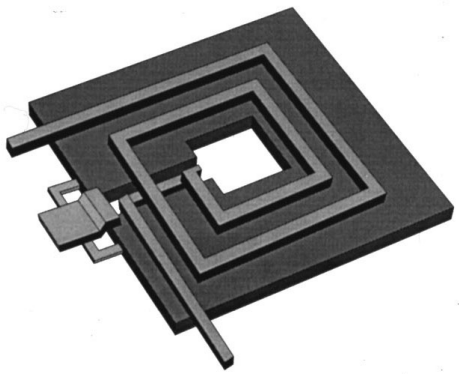

Figure 4: Three dimensional sketch of a microstrip resonator. Both ground-plane and top strip-line are made of superconducting materials - like Aluminum or Niobium. The dielectric substrate can be made of Si or SiO_x. This picture has been taken from Ref. [10]

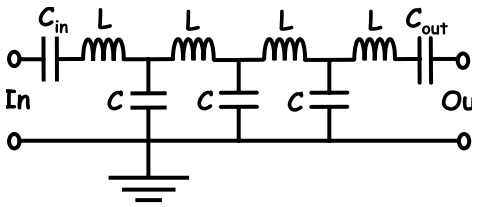

Figure 5: Approximation of a MR with a ladder network made of series inductors and capacitors shunting to ground (neglecting any sort of losses).

Two crucial parameters of a MR are the internal and external (or loaded) quality factors, Q_i and Q_e respectively.

The internal quality factor strictly depends on all intrinsic losses of the resonator. Even a superconducting ground-plane and top strip-line will show a finite surface resistance at microwave frequencies, which of course will lead to losses. The substrate loss tangent will also decrease

Q_i, though the biggest source of loss will certainly be due to geometrical discontinuities in the structure where electromagnetic radiation can leak. Q_i values of the order of $10^5 - 10^6$ could be obtained by good engineering (see [8]) of the MR.

In order to measure the transmission-reflection properties of the system (the scattering matrix), the MR must be connected to input and output transmission lines making use of on-chip finger-capacitors. The dimensions of these capacitors will set the external (also called loaded) quality factor. They are a sort of gates letting more or less microwave photons enter and leave the cavity. It is easy to figure out that the cavity lifetime, $1/\kappa$, will depend on Q_e. So, $Q_e \approx 10^4$ would mean $1/\kappa \approx 160\,\text{ns}$ and $\kappa/2\pi \approx 1\,\text{MHz}$.

The resonance frequency of the MR will be chosen to be about 10 GHz. The main reason for this choice stems from black-body radiation. The electronic temperature at which the MR will be operated is about 100 mK. A 10 GHz microwave photon has an equivalent temperature of roughly 500 mK. Thus, its quantum nature will not be smeared out by environmental black-body radiation due to the finite electronic temperature (which is smaller than 500 mK). This simply means that, if no field is driven into the resonator, the MR will behave as a quantum harmonic oscillator in its ground-state (or vacuum state). The MR Hamiltonian reads at low temperature

$$\hat{H}_r = \hbar\omega_0\left(\frac{1}{2} + a^\dagger a\right), \tag{3}$$

where $a^\dagger$ and a are the creation and annihilation operators of the cavity field. Another way of representing a MR is by means of circuit lumped elements. To some extents, it is possible to approximate the resonator described above (see fig. 4) with a ladder network made of series inductors and capacitors shunting to ground (neglecting any sort of losses). The inductors are due to the presence of the top strip-line and the capacitors to the presence of the two conductors (top strip-line and ground-plane) separated by a dielectric substrate. These circuit elements are substantially distributed elements (inductance L_0 and capacitance C_0 per unit length). Figure 5 is an example of such a ladder network. The resonance frequency of this circuit writes

$$f_0 = \frac{1}{l\sqrt{L_0 C_0}}, \tag{4}$$

where l is the length of the top strip-line. In order to calculate the ac magnetic field inside the cavity, the Lagrangian density of the MR

$$\mathcal{L} = \int_l dl\left(\frac{L_0}{2}j^2 - \frac{1}{2C_0}q^2\right) \tag{5}$$

must be considered, where $j(l;t)$ and $q(l;t)$ are the local current and charge densities, respectively. Eq. (5) accounts for the magnetic energy stored in the inductive elements and for the electric energy stored in the capacitive elements. Using the right boundary conditions it is easy to find an expression for the current density distributed on the MR. This current density can then be utilized for calculating the *rms* magnetic field B all around the resonator and in particular in its center (that is where the QuBit will be placed).

V: The QuBit-Cavity Interaction

As shown in fig. 6, the QuBit is placed in the center of the MR. This ensures a large *rms* magnetic field in the QuBit loop which, together with the high polarizability of this artificial two-level system operated at the degeneracy point, allows for a strong coupling g. The coupling strength is given by

$$g = \frac{2\mu_q B}{\hbar}. \tag{6}$$

The coupling g for the PC-QuBit-MR system considered here has been calculated to be larger than 100 MHz. This means that the interesting limit of strong coupling cQED could be reached $(g/\pi \gg (\gamma/2; \kappa/2\pi))$.

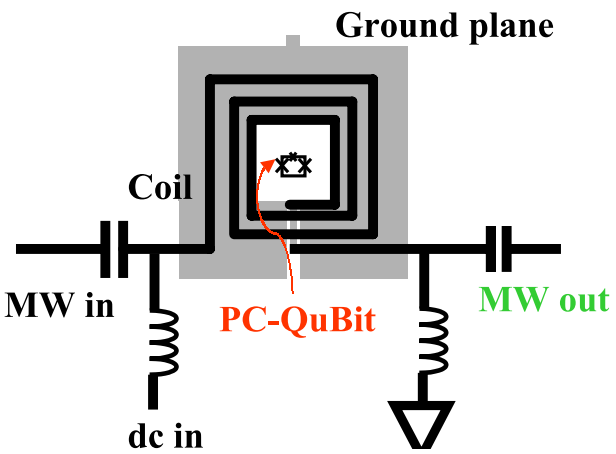

Figure 6: The PC-QuBit is placed in the center of the MR. This ensures a large *rms* magnetic field in the QuBit loop which, together with the high polarizability of this artificial two-level system operated at degeneracy point, allows for a strong coupling g.

As already pointed out in section II, the on resonance regime and the off resonance regime have to be analyzed. To explore these two different cases, the most convenient way is by means of the Jaynes-Cummings formalism. The QuBit-MR interaction Hamiltonian reads

$$\hat{H}_i = \hbar g(a^\dagger \sigma^- + a\sigma^+)\,, \tag{7}$$

where σ^+ and σ^- are Pauli raising and lowering operators. Combining the QuBit Hamiltonian, Eq. (1), the MR Hamiltonian, Eq. (3), and the interaction Hamiltonian, Eq. (7), gives

$$\hat{H} = \frac{\hbar\Omega}{2}\hat{\sigma^z} + \hbar\omega_0\left(\frac{1}{2} + a^\dagger a\right) + \hbar g(a^\dagger\sigma^- + a\sigma^+), \tag{8}$$

which is usually called Jaynes-Cummings Hamiltonian.

The on-Resonance Regime

For the case of zero detuning between QuBit and cavity $\Delta = 0$, exact diagonalization of the Hamiltonian (8) yields the eigenenergies

$$E_{\pm,n} = (n+1)\hbar\omega_0 \pm \frac{\hbar}{2} 2g\sqrt{(n+1)}, \tag{9}$$

where n is the number of photons populating the cavity. Measuring the transmission of the QuBit-MR system will show two peaks, $2g\sqrt{(n+1)}$ apart. The separation between the two peaks represents the vacuum Rabi splitting in the frequency domain. Naturally, it is not possible to infer information on the state, $|L\rangle$ or $|R\rangle$, of the QuBit in this case. To obtain this information, and thus reading-out the QuBit, it is necessary to strongly detune the QuBit and the cavity.

The off-Resonance Regime

The case $g/\Delta \ll 1$ (dispersive regime) allows for reading out the state of the QuBit. More insight into the dispersive regime can be gained by making a unitary transformation of Eq. (8) and expanding to second order in g to obtain ([6])

$$U\hat{H}U^{\dagger} \approx \hbar\left(\omega_0 + \frac{g^2}{\Delta}\hat{\sigma^z}\right)a^{\dagger}a + \frac{\hbar}{2}\left(\Omega + \frac{g^2}{\Delta}\right)\hat{\sigma^z}. \tag{10}$$

In this regime, measuring the transmission of the system will allow for discriminating between the $|L\rangle$ and the $|R\rangle$ state of the QuBit. The cavity works as a read-out device.

VI: Final Remarks and Outlook

Concluding, it has been shown that it is possible to realize a cQED experiment making use of on-chip superconducting devices. The main properties of PC-QuBits have been explored showing in particular that the polarizability of such a system can be very large at degeneracy point and that its energy relaxation rate $\gamma/2$ can be as small as 1 MHz. The characteristics of MR have been discussed as well and it has been shown that in structures of this type high *rms* magnetic fields are achievable. Moreover, microwave resonators can be engineered so that their characteristic decay rates $\kappa/2\pi$ do not exceed 1-2 MHz. The QuBit-MR coupling strength g has been shown to be as large as 100 MHz (meaning much larger than both $\gamma/2$ and $\kappa/2\pi$). The strong coupling regime of cQED can be achieved.

In the next step this theoretical proposal will be realized at the WMI. Most of the equipment (microwave source, high frequency spectrum analyzer and network-vector analyzer, cryogenic and room temperature ultra-low-noise microwave amplifiers, circulator, low heat conductance and high microwave performance coaxial cables, I/Q and microwave-pulse mixers, power dividers, boosting amplifier for operating the mixers, high frequency bias tees, ...) necessary for the experiment has been already prepared and, within the next few months, will be installed into *Old Faithful*, the dilution refrigerator at disposition at the WMI. The design of the samples is in preparation using a home-made 3D microwave software adapted for simulating superconductors. The samples will then be fabricated at MIT Lincoln Laboratory. More details about the experimental set-up can be found in a different section of the WMI Annual Report 2004.

Acknowledgements

The authors would like to acknowledge J.M. Raimond, M. Amin, J. von Delft, A. Wallraff, P. Delsing, P. Lorenz, K. Fichtner, B. Biscontini, and P. Russer, K. Neumaier, and C. Probst, T. Heimbeck, K. Madek, G. Wild, R. Stolle, and B. Huber for useful and fruitful discussions.

References

[1] J. M. Raimond, M. Brune, and S. Haroche, Rev. Mod. Phys. **73**, 565 (2001).
[2] D. Walls and G. Milburn, *Quantum Optics* (Springer-Verlag, Berlin, 1994).
[3] Y. Nakamura, Yu. A. Pashkin, and J. S. Tsai, Nature **398**, 786 (1999).
[4] J. E. Mooij, T. P. Orlando, L. Levitov, L. Tian, C. H. van der Wal, and S. Lloyd, Science **285**, 1036 (1999).
[5] A. Wallraff, D. I. Schuster, A. Blais, L. Frunzio, R.-S. Huang, J. Majer, S. Kumar, S. M. Girvin, and R. J. Schoelkopf, Nature **431**, 162 (2004), cond-mat/0407325.
[6] A. Blais, R.-S. Huang, A. Wallraff, S. M. Girvin, and R. J. Schoelkopf, Phys. Rev. A **69** (2004), cond-mat/0402216.
[7] H. Mabuchi and A. Doherty, Science **298**, 1372 (2002).
[8] M. Mariantoni, M. J. Storcz, W. D. Oliver, F. K. Wilhelm, A. Marx, and R. Gross, in preparation (2004).
[9] I. Chiorescu, Y. Nakamura, C. J. P. M. Harmans, and J. E. Mooij, Science **299**, 1869 (2003).
[10] M. Mück and J. Clarke, J. Appl. Phys. **88**, 6910 (2000).

TMR Effect and Spin Polarization of Thin Films of Magnetite (Fe_3O_4)

S. Qureshi, D. Reisinger, E. Menzel, A. Erb, M. Opel, and R. Gross [1]

Magnetic random access memory (MRAM) devices based on magnetic tunnel junctions (MTJ) using ferromagnetic metals and alloys with limited spin polarization will be implemented in next generation computer memory. Beyond purely storage usage, MTJs can at the same time be used as programmable logic elements [1]. While the device preparation techniques using simple metals and alloys are at least in principle well known, from the point of view of magnetic properties half-metallic materials certainly are superior to classical ferromagnetic transition metals. Magnetite (Fe_3O_4) is an interesting candidate, because it has been predicted to be a half-metal even at room temperature due to its high Curie temperature of 860 K [2]. Indeed, spin-resolved photoelectron spectroscopy in magnetite thin films has recently revealed a spin polarization near the Fermi level of up to 80% at room temperature [3]. In contrast, in MTJs based on magnetite only small TMR effects have been observed with a maximum effect of 14% [4]. Therefore, it is important to understand the behavior of magnetite at the electrode/barrier interface, the influence of the tunneling barrier itself, and the magnetic coupling through thin barrier layers.

Here, we report on measurements of MTJs based on epitaxial magnetite thin films on MgO(001) single crystal substrates. As tunneling barrier five different materials (MgO, $SrTiO_3$, $NdGaO_3$, SiO_2, and AlO_x) have been investigated. As counter-electrodes Ni and Co were used with about 33% and 44% spin polarization as known from tunneling measurements, respectively [5]. The whole thin film structure was grown by pulsed laser deposition (PLD) or electron beam evaporation in an ultra high vacuum system. The magnetic properties, in particular the coupling of the electrodes through the barrier, have been studied by SQUID magnetometry. The tunnel junctions with areas ranging from $10 \times 10 \ldots 20 \times 40^{-}m^2$ were fabricated by optical lithography and ion beam etching. The magnetotransport behavior of these MTJs was measured as a function of temperature and applied magnetic field.

The thin films were fabricated in an ultra high vacuum (UHV) laser deposition system with in-situ electron beam evaporation [6]. The magnetite bottom electrode was grown epitaxially on MgO single crystal substrates, mostly with an underlying epitaxial TiN buffer layer. Details about the whole process including in-situ reflection high energy electron diffraction (RHEED) and laser substrate heating are described elsewhere [7, 8, 9]. The surface quality was probed in-situ with an Omicron atomic force microscope, the crystal properties and film thickness with a Bruker-AXS high resolution X-ray diffractometer, and the magnetic properties with a Quantum Design superconducting quantum interference device (SQUID) magnetometer. The magnetotransport measurements were performed in an Oxford cryostat system with variable temperature insert and a 10 Tesla superconducting magnet. The magnetite thin films achieved nearly the same properties as single crystal bulk material with respect to magnetization on the Verwey transition behavior [10].

On top of the 40 . . . 50 nm thin magnetite films, 2 . . . 7 nm thin insulating layers serving as tunnel barriers are deposited. Five different materials were used: MgO, $SrTiO_3$, and $NdGaO_3$ have been fabricated by PLD from stoichiometric targets, SiO_2 and AlO_x layers were deposited by electron beam evaporation in UHV. During PLD growth the Ar atmosphere was 10.3 mbar, and the substrate temperature was 330°. The only material growing epitaxially on Fe_3O_4 is MgO as confirmed by the corresponding RHEED pattern. Epitaxial growth of MgO is also achieved at room temperature for a pure oxygen atmosphere (10.3 mbar). The SiO_2 and Al layers were

[1] This work is supported by the BMBF (project no. 13N8279).

deposited without breaking the UHV after the magnetite deposition. Both materials are grown at room temperature. Afterwards the Al was oxidized in pure oxygen to form the insulating AlO_x. $SrTiO_3$, $NdGaO_3$, SiO_2, and AlO_x all form polycrystalline layers on magnetite due to the large lattice mismatch. In a further step, a 40 nm Ni or Co layer was deposited in-situ as magnetic counter electrode by electron beam evaporation in UHV at room temperature.

For an ideal switching behavior of a TMR device, it is important that both ferromagnetic electrodes switch their magnetization separately at different applied magnetic fields. Then, within a certain field range, a stable antiparallel configuration of the magnetization of the electrodes can be achieved. The difference in resistance of the stable states with perfect parallel and antiparallel order of the magnetization of the electrodes is a key precondition for high TMR effects [11]. Therefore, the magnetization as a function of the applied magnetic field of the $5 \times 5\text{mm}^2$ multilayer samples has been measured before any lithographic step.

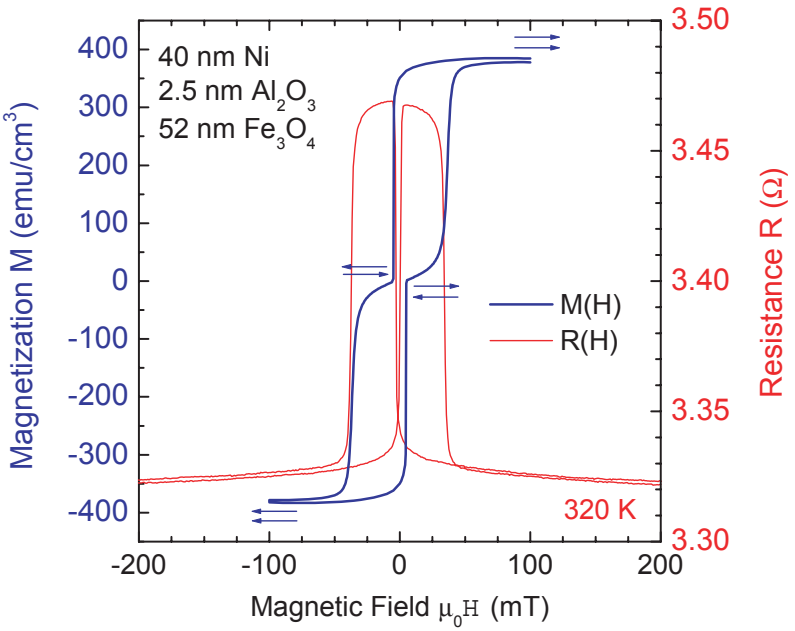

Figure 1: Magnetization at 210 K for a $5 \times 5\text{mm}^2$ multilayer (blue) and TMR effect at 320 K from a $20 \times 40^{-}\text{m}^2$ multilayer (red) of Fe_3O_4(52 nm)/AlO_x(2.5 nm)/Ni(40 nm).

Fig. 1 (blue curve) shows the magnetization $M(H)$ of one samples consisting of 14 nm TiN, 52 nm Fe_3O_4, 2.5 nm AlO_x, and 40 nm Ni at 210 K. This sample clearly shows a separate switching of the electrode magnetization. The coercive fields of the Ni and the Fe_3O_4 layer are 5 mT and 32 mT, respectively. These numbers decrease to 2 mT and 24 mT, respectively, at 380 K. The coercive field of the Ni layer is found to be slightly increased as compared to the value from a single 20 nm thin reference Ni film (0.25 mT at 290 K). This effect is due to residual coupling through the thin insulating barrier. Concerning the other barrier materials we find that for SiO_2 the switching steps are less rounded than for AlO_x indicating that magnetic domains switch more simultaneously within the whole interface region. On the other hand, the film thickness is more difficult to control for SiO_2 than for AlO_x. For MgO barriers, the difference of the coercivities of Fe_3O_4 and Ni is found to be only about 7 mT at room temperature. At lower temperatures (210 K and 150 K) the electrodes switch together at approximately 30 mT. It is evident that for the samples with MgO barriers the ferromagnetic electrodes are strongly coupled through the barrier layer, thus behaving as a single ferromagnetic layer. The origin of this coupling still has to be clarified. Since AlO_x barriers turned out to be optimum with respect to magnetic decoupling and thickness control, we focused on Fe_3O_4/AlO_x/(Ni,Co) multilayers for the realization of MTJs. The clear step-like shape of the hysteresis $M(H)$ (Fig. 1, blue) at all temperatures between 210 K and 380 K is an indication of nearly ideal ferromagnetic order in the electrode layers of these multilayer structures. This is important with respect to the formation of magnetic domains or glass-like behavior which both is unfavorable for the device

performance.

Starting from these multilayers, tunnel junctions have been fabricated using optical lithography and ion beam etching (see Fig. 2). The complex production process consists of roughly 35 critical steps. The measurement current flows from the main bottom electrode path (TiN), up through the turret formed by the ferromagnetic bottom electrode (Fe_3O_4) across the tunnel barrier (AlO_x) and the ferromagnetic counter electrode (Ni or Co), perpendicular to the sample surface, and then back through the Au wiring layer.

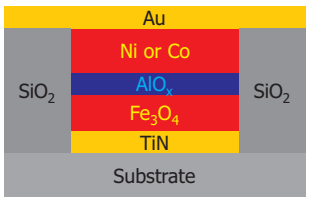

Figure 2: Cross-sectional view of a Magnetic Tunnel Junction (MTJ). The current flows perpendicular to the multilayer structure from the bottom electrode (TiN/Fe_3O_4) across the tunnel barrier (AlO_x) to the top electrode (Ni/Au or Co/Au).

A first crucial test for the reproducibility of the tunnel barrier is the investigation of the product of junction area A and junction resistance. We have listed the measured room temperature values for a sample consisting of four contacts with different size but with the same 2.5 nm AlO_x barrier (see table). The four-point-resistance R_{4p} of the contacts scales inverse to their area, and the resistance-times-area-product $R_{4p} \cdot A$ of all contacts is of the same order of magnitude.

area A	R_{2p} (Ω)	R_{4p} (Ω)	$R_{4p} \cdot A$ (Ωm^2)
$10 \times 10^{-}$m^2	172	66	$6.6 \cdot 10^{-9}$
$10 \times 20^{-}$m^2	292	36	$7.1 \cdot 10^{-9}$
$20 \times 20^{-}$m^2	407	23	$9.1 \cdot 10^{-9}$
$20 \times 40^{-}$m^2	539	5	$4.0 \cdot 10^{-9}$

This shows that all contacts are approximately of the same quality, independent of their size. This implies that the insulating SiO_2 coating at the border of the TMR turrets indeed suppresses leakage currents. The values obtained here for AlO_x barriers are comparable to the results of other groups [12]. The junctions with the higher $R_{4p} \cdot A$ also had a significantly higher TMR effect [12]. This shows that an optimization of the Al oxidation process is a crucial step in the fabrication of a TMR device.

Fig. 3 shows the resistance versus temperature, $R(T)$, curves for MTJs with different tunnel barriers as well as for a magnetite reference film for comparison. All curves are normalized to their room temperature resistance. The absolute resistance values are in the range of 5 $\Omega \ldots 10$ kΩ at room temperature. Due to the Verwey transition, the resistance of the magnetite layer increases by several orders of magnitude at approximately $T_V \simeq 120$ K [13]. For the multilayer systems the resistance increases already at temperatures well above T_V. This effect is most pronounced for the MgO barrier layer where the resistance starts to increase strongly at around 175 K. With respect to the magnetization measurements discussed above it is likely that the MgO barriers prepared in reducing atmosphere have a high density of oxygen defects. Therefore, the increase of resistance is most likely due to the suppression

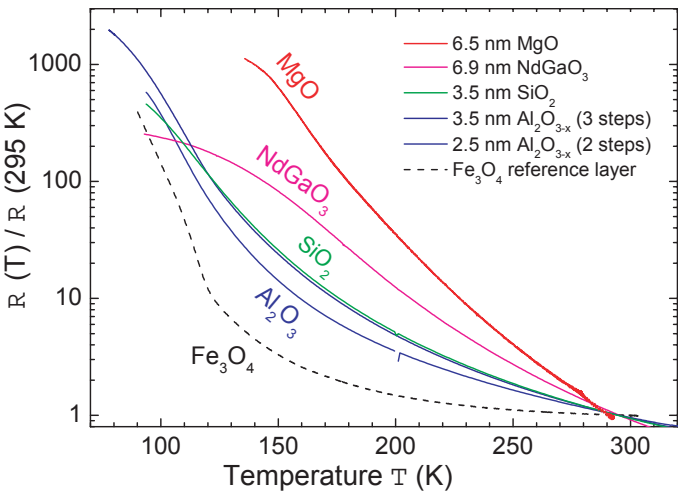

Figure 3: $R(T)$ of TMR-contacts with different tunnel barriers.

of thermally activated hopping conduction through the insulating barrier. Here, we briefly estimate the influence of the magnetite electrode on the resistance of the whole turret structure. Assuming a homogeneous current feed into the turret due to the well conducting TiN buffer layer and knowing the resistivity of magnetite, a resistance of $5.6 \cdot 10^3\ \Omega$ at room temperature is expected for a $20 \times 20^{-}\mathrm{m}^2$ turret. It is evident that the effect of Fe_3O_4 is negligible at least at temperatures not too close to the Verwey transition. However, in the case of an inhomogeneous current feed, the influence of the magnetite electrode can no longer be neglected. In any case, for a precise and reliable determination of the barrier properties it is necessary to have a low resistance buffer layer underneath the Fe_3O_4 electrode.

With $R(H)$ measurements in 4-point-technique the TMR effect

$$TMR = \frac{R_{\mathrm{antiparallel}} - R(H)}{R_{\mathrm{parallel}}} \tag{1}$$

was determined for the different barrier materials at different temperatures between 160 K and 300 K. $R_{\mathrm{antiparallel}}$ is the resistance in the antiparallel magnetization configuration of the electrodes, which corresponds to the maximum resistance. R_{parallel} is the resistance in the parallel magnetization configuration of the electrodes corresponding to the minimum resistance and was measured at 100 mT. The samples reproducibly show a clear positive TMR effect with almost ideal, symmetric switching behavior as shown in Fig. 1 (red). The TMR effect is observable in the whole measured temperature range from 150 K to 350 K. At room temperature, up to 5% resistance change was found. The switching fields correspond very well to the coercive fields of the magnetic electrodes (Fig. 1, blue). Note that the increase of resistance for antiparallel electrode magnetization (positive TMR effect) confirms the negative spin polarization of Fe_3O_4. Since Ni and Fe_3O_4 both have negative spin polarization, the observed behavior is expected. For an electrode with positive spin polarization as the double exchange material $La_{0.7}Sr_{0.3}MnO_3$, a negative TMR effect is expected, and indeed observed [14, 15].

From measurements of the temperature dependence of the TMR effect, we found indication for an additional contribution to the tunneling magnetoresistance. This was identified as a series resistance probably coming from an additional insulating barrier between the Ni and the Au layer. To verify this assumption, we split the Au electrode into two parts to separate the voltage contact from the current feed. Repeating the $M(H)$ measurements we find an increase in the TMR effect from 5 to 11% (Fig. 4, red) [16]. After then replacing Ni by Co, a further increase of TMR up to 16% at room temperature is obtained (Fig. 4, blue). These values are much larger than the best values reported so far for magnetic tunnel junctions based on Fe_3O_4 [4].

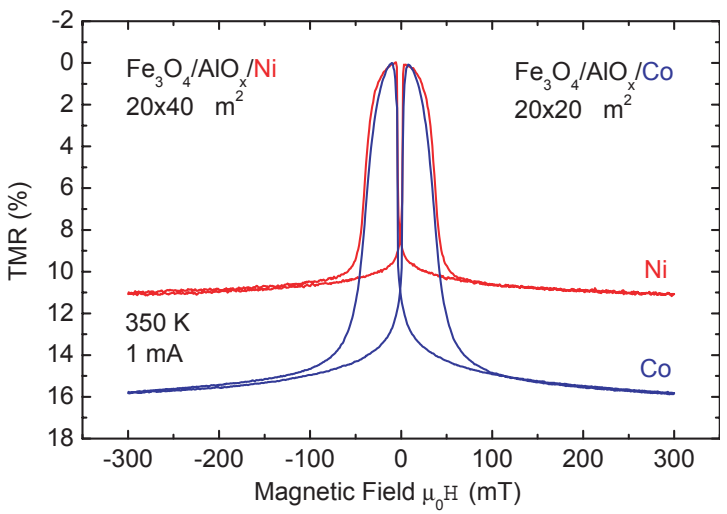

Figure 4: *TMR* at room temperature with splitted Au electrode for two different top electrode materials, Ni (red) and Co (blue).

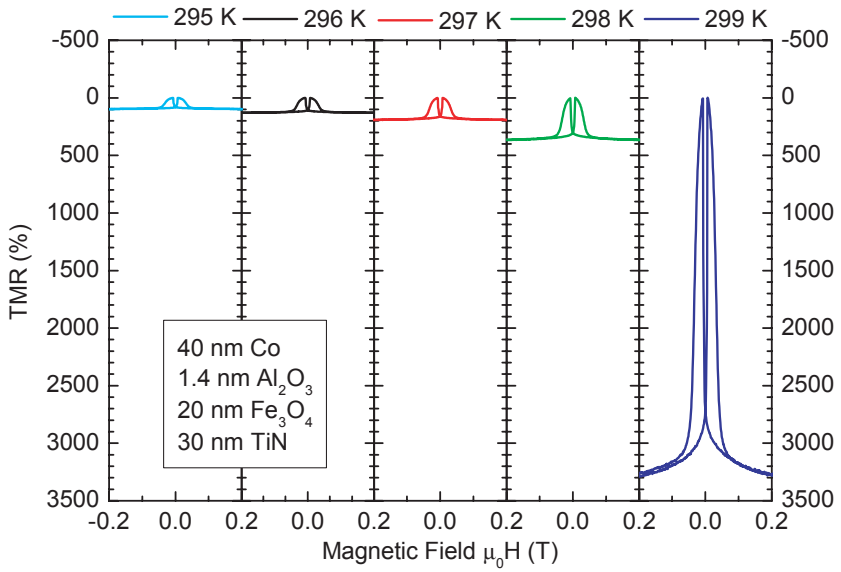

Figure 5: TMR for TiN/Fe_3O_4/AlO_x/Co at different temperatures

According Jullière's model [11] the TMR value is related to the spin polarizations P_1,P_2 of the ferromagnetic electrodes as

$$TMR = \frac{2P_1P_2}{1-P_1P_2} \quad . \tag{2}$$

Since we have used two different top electrode materials (Ni and Co), we can make an estimate for the spin polarization P of magnetite from the ratio $x = \frac{TMR_{Co}}{TMR_{Ni}}$ using

$$P = \frac{1}{P_{Co}P_{Ni}} \frac{xP_{Ni} - P_{Co}}{x-1} \quad . \tag{3}$$

Doing so, we can eliminate effects coming from our experimental setup or the specific preparation of the samples. With the measured value $x = \frac{16\%}{11\%} \approx 1.5$ we obtain a very high spin polarization of 60% for magnetite at room temperature. The difference between this value and the theoretically predicted 100% for half-metallic Fe_3O_4 at $T = 0$ can be understood due to the increase in spin-scattering at defect states in the tunneling barrier. In addition, it is expected that the measured spin polarization reaches higher values at lower temperatures.

Further investigations in different samples showed that the maximum TMR effect can depend very sensitively on temperature. Fig. 5 shows TMR measurements from the same sample of TiN(30nm)/ Fe_3O_4(20nm)/ AlO_x(1.4nm)/ Co(40nm) at different temperatures. We find that the TMR increases up to 3 300% between 295 and 299 K. The reason is that the denominator R_{parallel} in eq. 1 approaches zero (see Fig. 6) leading to an extremely high TMR value. This effect could be reproduced in several samples and seems to depend strongly on the geometry of the layered MTJ structure. Further studies are necessary to clarify this phenomenon and to decide whether this geometrically-enhanced TMR effect can be used for TMR applications.

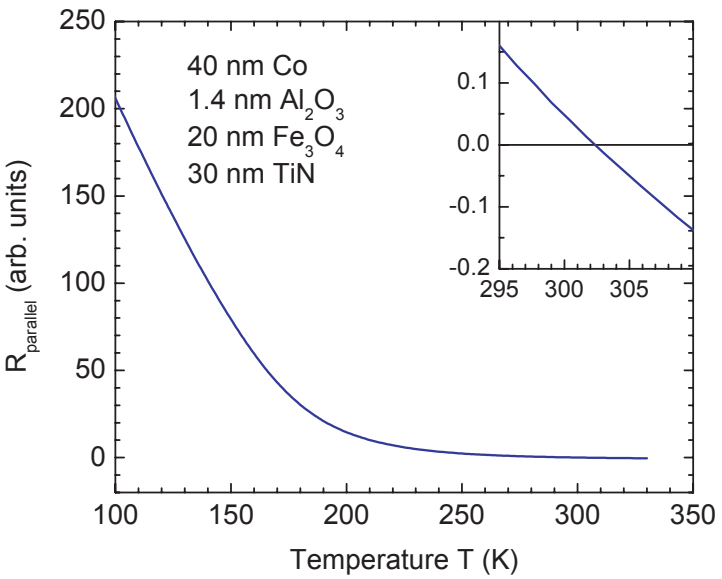

Figure 6: R_{parallel} vs. temperature for the sample presented in Fig. 5

In summary, we have successfully prepared magnetic tunnel junctions (MTJs) with different junction areas using optical lithography and ion beam etching. The bottom electrodes consist

of epitaxial magnetite thin films on MgO substrates using a TiN buffer layer. As tunnel barrier different materials have been investigated. Thin nickel or cobalt films served as counter electrode. The analysis of $M(H)$ curves showed that AlO_x is the optimum barrier material allowing for a clearly separated magnetization switching of the electrodes. The $R(T)$ curves of the MTJs showed a strong decrease of the junction resistance with increasing temperature. This may be due to tunneling via thermal activated defect states in the barrier layer. The MTJs with AlO_x barrier show reproducibly a clear TMR effect with ideal, symmetric switching behavior. The effect was visible in the whole investigated temperature range from 190 K to 380 K. At room temperature a resistance change of up to 16% was found. The spin polarization of magnetite at room temperature was estimated to about 60%. From the presented data, it is obvious that Fe_3O_4 with its high spin polarization is certainly an interesting candidate for spintronic devices at room temperature.

References

[1] A. Ney, C. Pampuch, R. Koch, and K. H. Ploog, Nature **425**, 485 (2003).
[2] Z. Zhang and S. Satpathy, Phys. Rev. B, **44**, 13319 (1991).
[3] Yu. S. Dedkov, U. Rüdiger, and G. Güntherodt, Phys. Rev. B **65**, 064417 (2002).
[4] H. Matsuda, M. Takeuchi, H. Adachi, M. Hiramoto, N. Matsukawa, A. Odagawa, K. Setsune, and H. Sakakima, Jpn. J. Appl. Phys. **41**, L387 (2002).
[5] J.S. Moodera, and G. Mathon, J. Magn. Magn. Mater. **200**, 248 (1999).
[6] R. Gross, J. Klein, B. Wiedenhorst, C. Höfener, U. Schoop, J. B. Philipp, M. Schonecke, F. Herbstritt, L. Alff, Yafeng Lu, A. Marx, S. Schymon, S. Thienhaus, W. Mader, in *Superconducting and Related Oxides: Physics and Nanoengineering IV*, D. Pavuna and I. Bosovic eds., SPIE Conf. Proc. **Vol. 4058** (2000), pp. 278–294.
[7] J. Klein, C. Höfener, L. Alff, and R. Gross, Supercond. Sci. Technol. **12**, 1023 (1999); see also J. Magn. Magn. Mater. **211**, 9 (2000).
[8] D. Reisinger, B. Blass, J. Klein, J.B. Philipp, M. Schonecke, A. Erb, L. Alff, and R. Gross, Appl. Phys. A **77**, 619 (2003).
[9] D. Reisinger, M. Schonecke, T. Brenninger, M. Opel, A. Erb, L. Alff, and R. Gross, J. Appl. Phys. **94**, 1857 (2003).
[10] D. Reisinger, P. Majewski, M. Opel, L. Alff, and R. Gross, Appl. Phys. Lett. **85**, 4980 (2004).
[11] M. Jullière, Phys. Lett. A **54**, 225 (1975).
[12] E.Y. Chen, R. Whig, J.M. Slaughter, D. Cronk, J. Goggin, G. Steiner, and S. Tehrani, J. Appl. Phys. **87**, 6061 (2000).
[13] E.J.W. Verwey, Nature **144**, 327 (1939).
[14] J.M. De Teresa, A. Barthélémy, A. Fert, J.P. Contour, R. Lyonnet, F. Montaigne, P. Seneor, and A. Vaurès, Phys. Rev. Lett. **82**, 4288 (1999).
[15] G. Hu and Y. Suzuki, Phys. Rev. Lett. **89**, 276601 (2002); G. Hu, R. Chopdekar, and Y. Suzuki, J. Appl. Phys. **93**, 7516 (2003).
[16] S. Qureshi, Master Thesis, TU München (2004).

Ferromagnetism in Mn-doped ZnO due to Impurity Bands

K.-W. Nielsen, J. Simon[a], J.B. Philipp, M. Opel, A. Erb, L. Alff, W. Mader[a], and R. Gross [1]

[a] Institut für Anorganische Chemie, Rheinische Friedrich-Wilhelms-Universität Bonn, 53117 Bonn

Diluted Magnetic Semiconductors (DMS) have attracted much interest due to the possibility to use both their interesting electric and magnetic properties. Along this line especially Mn-doped ZnO is a promising candidate for application. According to a theoretical prediction by Dietl *et al.* [1] for this material system of a Curie-Temperature T_C above room temperature should be achievable. However, within the model by Dietl *et al.* the ferromagnetism is assumed to be mediated by holes in the valence band and hole doping is difficult to be realized for ZnO. Nevertheless, there is experimental work reporting ferromagnetism in Mn- and Co-doped ZnO. The high Curie temperature in these electron doped materials cannot be explained by this model.

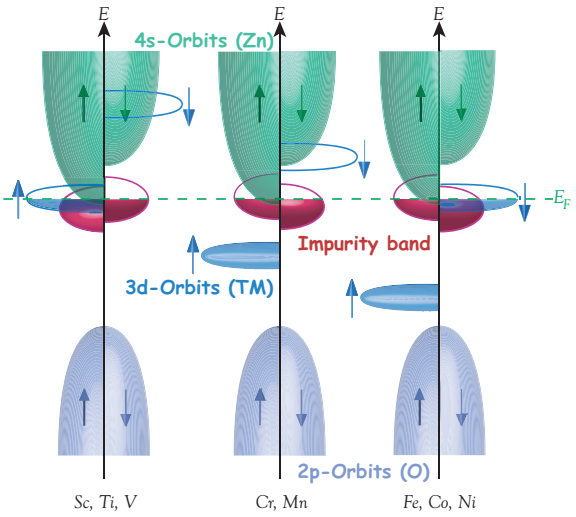

Figure 1: Schematic representation of the spin-split-orbit model (according to [2]).

More recently, Venkatesan and Coey [2] proposed the so called spin-split-orbit model, in which the magnetic interaction is mediated by a narrow spin-split impurity band formed by extended donor states (see Fig. 1). This band hybridizes with the 3*d*-orbitals of the doped transition metal ions. As shown schematically in Fig. 1, for the transition metals Sc, Ti and V the spin-up and for Fe, Co and Ni the spin-down states are aligned with the impurity band resulting in a strong hybridization. In this case the impurity state can mediate a strong ferromagnetic interaction between the 3*d* transition metal states. In contrast, for Mn and Cr there is only weak hybridization, since the impurity band resides in between the 3*d*-states spin-up and spin-down states of these transition metals. Therefore, in this case only weak ferromagnetism is expected.

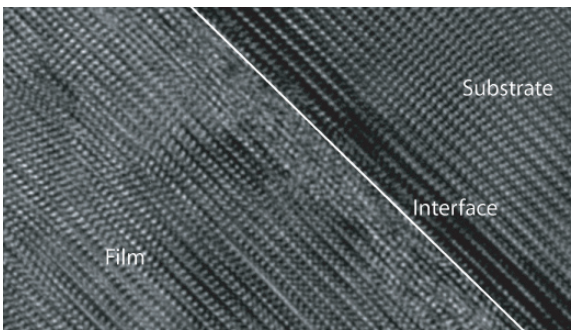

Figure 2: TEM-picture of a $Zn_{0.95}Mn_{0.05}O$-film grown at 200°C.

We have grown thin $Zn_{0.95}Mn_{0.05}O$-films quasi-homoepitaxially on (0001)-oriented ZnO-substrates by pulsed laser deposition (PLD). Two batches of samples were grown. The first batch was deposited at $p = 4.8 \cdot 10^{-3}$ mbar in pure Ar atmosphere and the second at $p = 5.9 \cdot 10^{-3}$ mbar in $Ar_{0.99}O_{0.01}$. The growth temperature of the first and second batch was 200 and 600°C, respectively. During deposition the films growth was characterized by in-situ RHEED. X-ray analysis showed no crystalline impurity phases. For the films grown at 600°C

[1] This work is supported by the Deutsche Forschungsgemeinschaft within the coordinated program SPP 1157 (project no. GR 1132/13-1).

separate (000ℓ) film peaks could be observed, while for the first batch this was not the case. This may be due to the worse crystalline quality of the films deposited at lower temperature or due to overlapping with the substrate peaks. However, transmission electron microscopy (see Fig. 2) showed that the film deposited at 200°C also has grown epitaxially on the ZnO substrate. Furthermore, Fig. 2 shows that there is a high number of defects at the substrate-film interface and also within the film as expected for the low growth temperature. In addition, it can be seen that the crystalline quality of the films improves with increasing thickness. This may result in inhomogeneous magnetic properties across the film thickness.

We have performed electrical transport measurements for both sample batches. Fig. 3 shows the $R(T)$-curves between 5 K and 300 K at zero applied magnetic field. The resistance is plotted on a logarithmic scale versus $1/T$. In this representation a linear regime corresponds to a specific activation energy E_a according to

$$\ln R = \frac{E_a}{k_B} \cdot \frac{1}{T} + \ln R_0 \,. \qquad (1)$$

Here, k_B is the Boltzmann constant and R_0 a temperature independent contribution to the resistance. It is evident that both sample batches show a linear behavior in the temperature range between about 100 and 200 K with E_a ranging between 18 and 23 meV. We attribute this activation energy to Mn. Furthermore, the film grown at 200°C shows an additional linear regime at lower temperatures with $E_a \simeq 1.5$ meV, which is missing for the film deposited at 600°C-film [3]. Attributing this activation energy to the impurity band this suggests that there is such impurity band for the sample deposited at low substrate temperature, whereas it is absent for the 600°C-film.

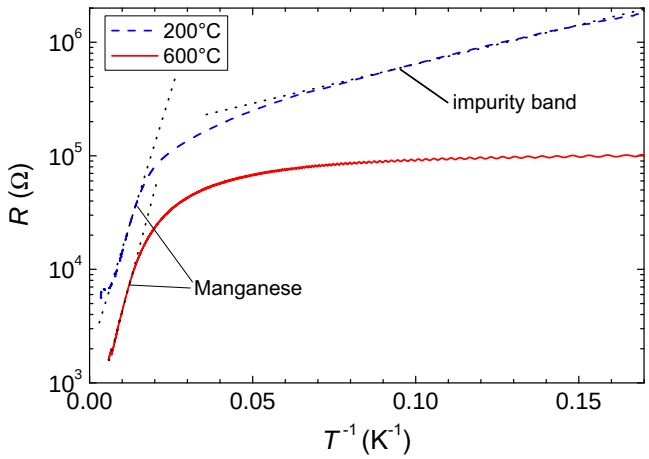

Figure 3: $\log R$ vs. $1/T$ for $Zn_{0.95}Mn_{0.05}O$-films grown at 200 and 600°C.

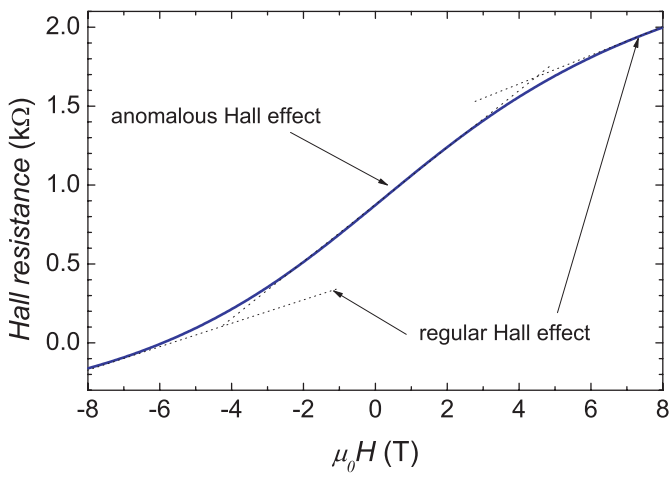

Figure 4: Hall resistance vs. applied magnetic field at $T = 50$ K for a $Zn_{0.95}Mn_{0.05}O$-film grown at 200°C.

Fig. 4 shows the Hall resistance a a function of the applied magnetic field for a $Zn_{0.95}Mn_{0.05}O$-film deposited at 200°C for $T = 50$ K. At low fields an anomalous Hall effect is observed. This observation provides strong evidence for the intrinsic nature of the observed ferromagnetism, because it is based on the interaction between spin polarized charge carriers and diluted ferromagnetic ions. The anomalous Hall contribution arises from the finite sample magnetization, which results in a field dependent Hall resistance at low fields. Since the sample magnetization saturates at higher fields, the field variation of the total Hall resistance is linear at high fields and originates only from the

regular Hall effect. That is, the measured total Hall resistance represents a superposition of the anomalous and normal contribution. It shows a non-linear field dependence due to the anomalous contribution at low fields and a linear dependence at high fields, where the sample magnetization is saturated and the field variation is only due to the normal contribution. We also note that the measured sign of the regular Hall effect shows that the charge carries in the investigated samples are electrons. The Hall effect data is consistent with magnetization measurements, which showed a ferromagnetic hysteresis only for films grown at 200°C and none for those grown at 600°C. According to the $M(T)$ measurements the Curie temperature for the $Zn_{0.95}Mn_{0.05}O$-films grown at 200°C is about 250 K.

In summary, our results support the spin-split-orbit model proposed by Venkatesan and Coey [2]. In particular, we could show that there is a correlation between the existence of an impurity band and the presence of ferromagnetic coupling in Mn substituted ZnO. However, there a several open issues that have to be addressed in our future work. For example, the optimum band gap and the detailed nature of the impurity band is not known.

References

[1] T. Dietl, H. Ohno, F. Matsukara, J. Cibert and D. Ferrand, Science **287**, 1019-1022 (2000).
[2] M. Venkatesan, C.B. Fitzgerald, J.G. Lunney and J.M.D. Coey, Phys. Rev. Lett. **9**3, 177206 (2004).
[3] K.-W. Nielsen, J.B. Philipp, M. Opel, A. Erb, J. Simon, L. Alff and R. Gross, Superlattices and Microstructures, accepted for publication (2004).

Ferromagnetism in Thin Films of Co-doped ZnO

M. Lübbe, K.-W. Nielsen, M. Diaconu[a], H. Schmidt[a], M. Opel, and R. Gross [1]

[a]University of Leipzig, Faculty of Physics and Earth Sciences, 04103 Leipzig, Germany

The field of spintronics has attracted considerable interest over the last decade. The general interest in the physics of spin transport in solids as well as the vision to develop novel spintronic devices, which make use of both the charge and spin degree of freedom of charge carriers, stimulated a broad research activity directed towards the generation, transport, manipulation, and detection of spin. With respect to potential applications, spintronic devices should be compatible to today's semiconducting electronic devices and operate at room temperature. Therefore, the development of ferromagnetic semiconducting materials, which could be used for spin injection into non-magnetic semiconductors, has attracted particular attention.

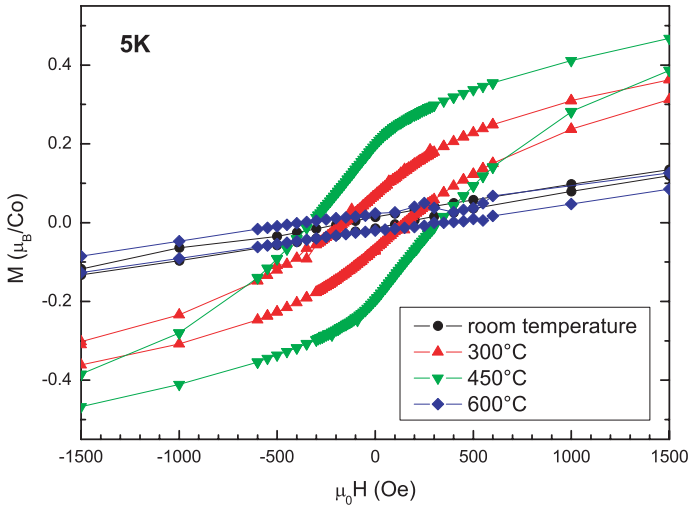

Figure 1: Magnetization curves of $Zn_{0.95}Co_{0.05}O$ films grown at different substrate temperatures measured at 5 K.

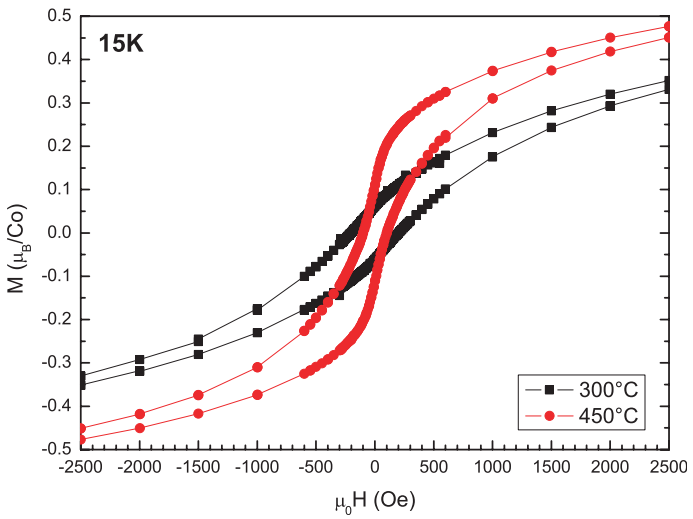

Figure 2: Magnetization curves of $Zn_{0.95}Co_{0.05}O$ films grown at 300°C and 450°C measured at 15 K.

Along this line, our research activity is focused on transition metal doped ZnO. For this diluted magnetic semiconductors (DMS), in which a few percent of the Zn ions are replaced by magnetic transition metal ions such as Mn or Co, a high Curie temperature well above room temperature has been predicted [1] making it interesting for applications. At present, the origin of ferromagnetism in transition metal doped ZnO ist discussed controversially. In the model by Dietl [1] ferromagnetism is assumed to be mediated by hole in the valence band. However, high Curie temperatures also have been observed for electron doped materials, although in this case only very weak ferromagnetism is expected according to Dietl's model. An alternative model for explaining the ferromagnetic exchange in doped ZnO was proposed recently by Venkatesan *et*

[1]This work is supported by the Deutsche Forschungsgemeinschaft within the coordinated program SPP 1157 (project no. GR 1132/13-1).

al. [2]. In this model ferromagnetism is assumed to be mediated by impurity band states. According to this model, $Zn_{1-x}Co_xO$ is expected to show the strongest ferromagnetism due to an optimum alignment of the impurity band with the Co 3*d* spin-down states. Preliminary results indeed indicate that a Co substitution of only 5% results in a magnetic moment up to 2.6 μ_B/Co and a Curie temperature above room temperature.

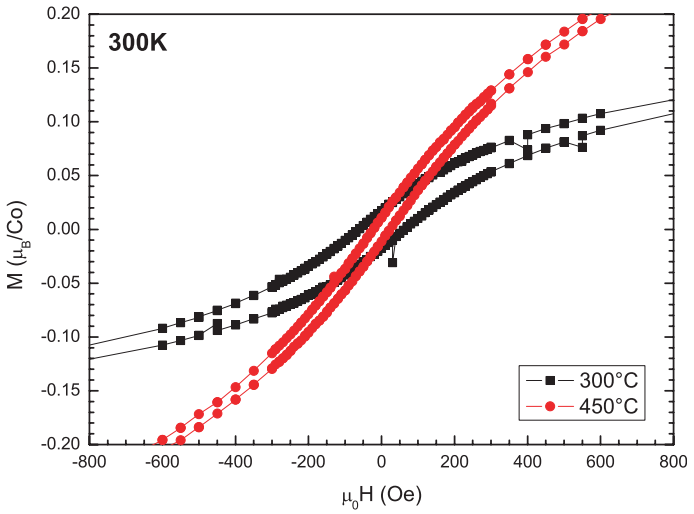

Figure 3: Magnetization curves of $Zn_{0.95}Co_{0.05}O$ films grown at 300°C and 450°C measured at 300 K.

We have prepared quasi-homoepitaxial $Zn_{0.95}Co_{0.05}O$ thin films on single crystalline ZnO substrates by UHV pulsed laser deposition under various deposition conditions. The substrate temperature was varied between room temperature and 600°C. Until now, primarily pure argon was used as deposition atmosphere (deposition pressure $p = 1.2 \cdot 10^{-3}$ Torr). The magnetic properties of the films were studied as a function of the substrate temperature used during deposition. We also made a few attempts with an argon/oxygen deposition atmosphere (99% Ar + 1% O_2). However, so far no significant improvement of the film properties compared to those obtained by using pure Ar could be achieved. Using in-situ RHEED characterization during film growth, the film thickness was estimated to be about 100 nm for all films. Unfortunately, this value obtained from RHEED could not be reconfirmed by X-ray reflectometry due to the small difference in the densities of film and substrate.

The films presented here are distinguished according to the substrate temperature used for their growth process (room temperature, 300°C, 450°C, and 600°C). The magnetic properties of the samples were analyzed by SQUID magnetometry. $Zn_{0.95}Co_{0.05}O$ films grown at room temperature or 600°C did only show a hysteresis loop down to 5 K, while those of films grown at 300°C or 450°C showed a large loop. Even at 300 K the latter films behaved ferromagnetic showing a small magnetic hysteresis. Considering the $Zn_{1-x}Co_xO$ films grown at 300°C and 450°C, the saturation magnetization increased (from 1 μ_B/Co to 1.5 μ_B/Co at 5 K) with increasing temperature. This was observed for all measurement temperatures. The hysteresis loop of the films deposited at 300°C was narrower than that of the film deposited at 450°C only at 5 K. The magnetic properties are illustrated in Figs. 1 to 3.

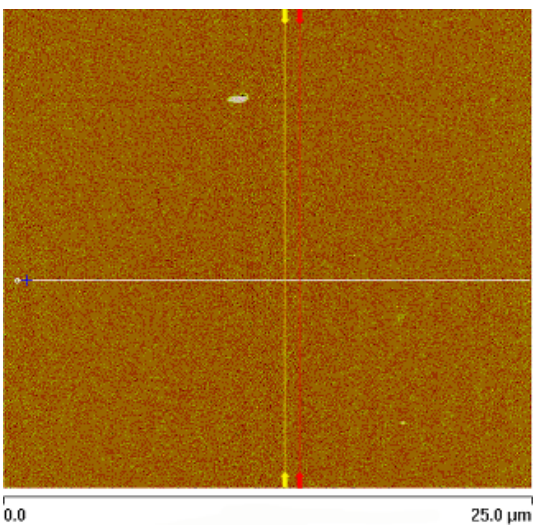

Figure 4: MFM picture of a $Zn_{0.95}Co_{0.05}O$ film grown at 300°C. The stripes (indicated by the two vertical lines) are characteristic for a ferromagnetic sample.

For samples grown at room temperature and 300°C the assumption that the magnetic hystere-

sis indicates ferromagnetism of the $Zn_{0.95}Co_{0.05}O$ film was supported by room temperature magnetic force microscopy (MFM) measurements, which were carried out at the University of Leipzig. For a film deposited at 300°C these measurements showed a pattern of vertical stripes (see Fig. 4), which are related to ferromagnetism [3]. In contrast, for a film deposited at room temperature such stripe pattern could not be observed by MFM in agreement with our magnetization measurements, which do not show any magnetic hysteresis for this sample. This result is important, since magnetization experiments alone cannot exclude the presence of ferromagnetic Co clusters as the origin of the observed ferromagnetism. The stripe pattern observed by MFM at least can exclude the presence of large Co clusters. Until now, we still cannot exclude the presence of homogenously spread small cobalt clusters. A TEM analysis of the films will help to clarify this point.

We also performed first measurements of the resistivity as a function of temperature as well as the applied magnetic field. The samples studied so far were found to be *n*-doped semiconductors.

Our preliminary results on thin films of Co-doped ZnO indicate that this material systems is promising as a DMS with high Curie temperature. Our future work will focus on detailed characterization of the magnetic, electronic and structural properties of this material system. In particular, Co clusters and effects related to the substrate-film interface have to be unambiguously excluded as possible origin of the observed magnetic hysteresis. Transmission electron microscopy (TEM) as well as optical measurements will be used to clarify this issue. Despite the remaining uncertainties, $Zn_{1-x}Co_xO$ seems to be a promising candidate for a diluted magnetic semiconductor.

References

[1] T. Dietl, H. Ohno, F. Matsukara, J. Cibert and D. Ferrand, Science **287**, 1019-1022 (2000).
[2] M. Venkatesan *et al.*, Phys. Rev Lett. **93**, 177206 (2004).
[3] P. Esquinazi *et al.*, Phys. Rev. Lett. **91**, 227201 (2004).

Dynamics of Inter-Layer Water Molecules in Graphite Oxide [1]

Anton Lerf, Alexandra Buchsteiner[a], Jörg Pieper[a], Stephan Schöttl[b]

[a] Hahn-Meitner-Institut, Berlin, Germany.

[b] National Physics Laboratory, London, UK.

Graphite oxide (GO) has been known since the 19th century [1]. Recent interest grew due to proposed application as material for battery electrodes [2, 3, 4], or as a membrane model [5]. In contrast to graphite and its intercalation compounds GO is hydrophilic and shows a remarkable hydration behaviour. However, the information about the mobility of the water molecules is not yet complete but crucial for the understanding of the structure of the C layers as well as the intercalation process. Various hydration levels are observed giving rise to different spacing of the carbon layers in the range from 6 Å to 12 Å. The degree of hydration and the kinetics of water uptake depends crucially on the preparation and aging conditions (Figure 1); we propose that it is related with the oxidation level of the GO used. The best sample we have ever got shows layer distances of 8.2, 8.7 and 11.5Å at relative humidities of 45, 75 and 100% .

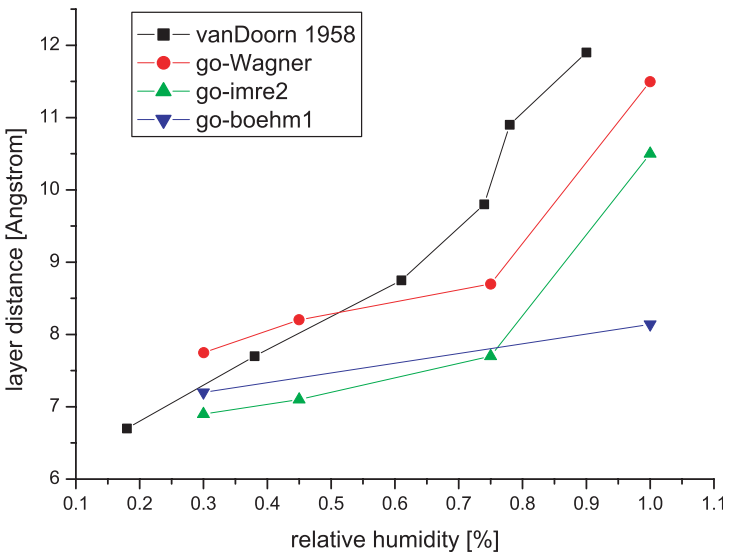

Figure 1: Layer distances vs. relative humidity. The data points are taken after a few days of equilibration time. The black curve is taken from [6].

With time-of-flight (TOF) neutron scattering at the spectrometer V3/NEAT at the Hahn-Meitner-Institut Berlin diffusion processes for the rotation and translation have been investigated. Different hydration levels were examined (usually with 1g of dry GO). Both H_2O and D_2O samples were produced. This way contributions from GO and intercalated water can be separated. Previous spectra were recorded at room temperature with two different energy resolutions of 66 μeV and 93 μeV, and measurement times of 8 to 15 hours, taking advantage of the full available beam time.

The most recent spectra of the samples were recorded in the temperature range 220 - 320 K with an energy resolution of 66 μeV. The preliminary data correction for detector efficiency and sample geometry as well as conversion to S(q,w) could be done on site. The position of the structural Bragg peak depends on hydration and is consistent with x-ray Debye-Scherrer patterns, taken at WMI. The latter finding proves that the samples can be related to the above mentioned well-defined hydration degrees and that the hydration level of the corresponding H_2O and D_2O samples was comparable. Quasielastic scattering was observed for all temperatures. The absolute intensity of the quasielastic contribution to the spectra clearly increases with hydration degree, as expected. Therefore, the spectra promise to be an excellent base for developing models of the water motion. Figure 2 shows normalized spectra of some samples at a scattering

[1] This experiment was supported by the European Union under contract HPRI-CT-2001-02138.

angle of 52°. Clearly, the lower water contents show similar peak shapes. This means that water added up to 50% has the same properties as water in the almost dry sample. This changes with the 100% sample, where the lower part of the peak broadens substantially. The central part, however, still appears similar to the less hydrated samples. Therefore, a new component of motion must be present for the added water molecules. This component has a shorter time constant, leading to a broader energy distribution.

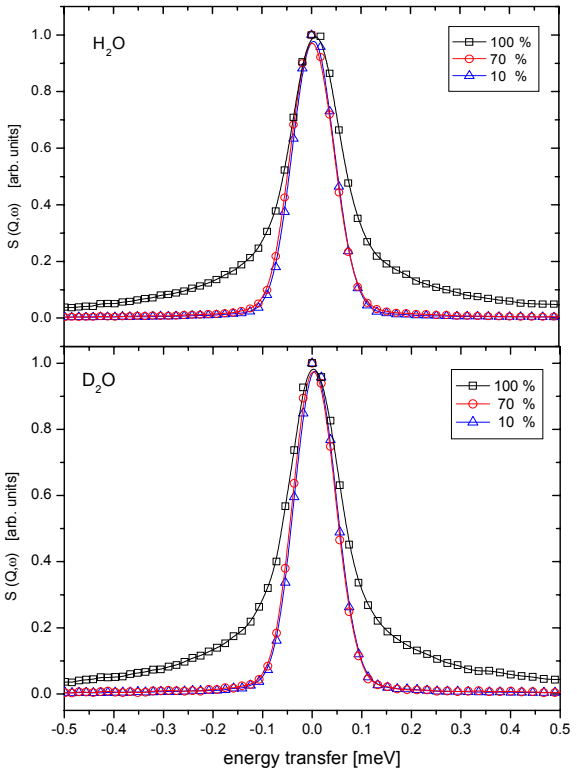

Figure 2: Normalized graphite oxide TOF neutron spectra at a scattering angle of 52°; light water samples in the upper panel; heavy water samples in the lower panel; all hydration levels are shown.

Summing up all our data three types of motion can be sorted out. The first one is a translational motion of water molecules in pores between the GO nanoparticles. Its translational diffusion constant increases with the water content of the samples and reaches the value typical for pure water in samples equilibrated over water (100% r.h.). The presence of this type of water depends crucially on the equilibration time and the sample quality.

Samples equilibrated at 45 and 70% relative humidity for three weeks (reaching layer distances of 8 and 9 Å, respectively) do not show this type of water. They exhibit instead two types of restricted motions: jumps between equivalent places with different jump distances and jump times. The jump distances of these motions are 3.05 Å and 1.5 Å, respectively. The short distance jumps are very probably due to 180°-flips of isolated water molecules encapsulated in the interlayer space between the functional groups attached to the carbon grid. This type of motion is comparable to that of water molecules in the monolayer hydrate of halloysite [7], but shows a lower activation energy than the latter. The origin of the second type of rotation (with the longer jump distances) is not clear at the moment, but it seems reasonable to assign it to OH-groups involved in hydrogen bonds with epoxide functions of the neighboring GO layers. The contribution of these long distance jumps decreases with increasing temperature and increasing water content. An increasing number of mobile water molecules due to temperature rise or higher water uptake may disturb the interlayer interaction.

References

[1] B. Brodie, Anal. Chem. Phys. **59**, 466 (1860).
[2] R. Yazami, and P. Touzain, Synth. Metals **12**, 499 (1985).
[3] M. Mermoux, R. Yazami, and P. Touzain, J. Power Sources **20**, 105 (1987).
[4] T. Cassagneau, and J. H. Fendler, Adv. Mater. **10**, 877 (1998).
[5] X. Wen et al., Nature **355**, 426 (1992).
[6] J. B. de Boer, and A .B .C . van Doorn, Koninkl. Nederl. Akad. Wetenschappen, Series B **61**, 242 (1958).
[7] M. I. Cruz, M. Letellier, and J. J. Fripiat, J. Chem. Phys. **69**, 2018 (1978).

Single crystal growth of cuprate superconductors

Andreas Erb, Michael Lambacher [1]

The physics of the cuprate superconductors is one of the most intensively studied fields in modern solid state physics. Nevertheless, up to now, there is no commonly accepted theory of high-temperature superconductivity. On the other hand, significant progress has been made especially in the last years in the quality of the available samples of the cuprate superconductors as well as in the precision of the measurement techniques. It is for this reason that we started a new coordinated research effort in the field of high temperature superconductivity. This research effort is supported by the DFG (Deutsche Forschungsgemeinschaft) within the new Research Unit 528: *"Doping Dependence of Phase Transitions and Ordering Phenomena in Cuprate Superconductors"*, which consists of 7 different research projects. One of these projects is focusing on *"Crystal Growth of p and n-doped cuprate superconductors"*.

The goal of this project is the growth and characterization of high purity single crystals of the high temperature superconductors to provide samples for different spectroscopic experiments within the coordinate research program of FOR 538. In order to cover the whole phase diagram of the high temperature superconductors we want to grow crystals with well defined and homogeneous doping of both, the p and n-doped compounds. The sample systems on the p-doped side of the phase diagram are mainly the 123-compounds and the Bi-2212 compound.

$YBa_2Cu_3O_{7-\delta}$:

In the field of the 123 - superconductors ($YBa_2Cu_3O_{7-\delta}$ and analogous rare earth compounds) crystals are grown out of high temperature solutions in the especially for this purpose developed inert crucible material $BaZrO_3$ [1,2], which allows the growth of crystals with purities up to 99.995 at. %.

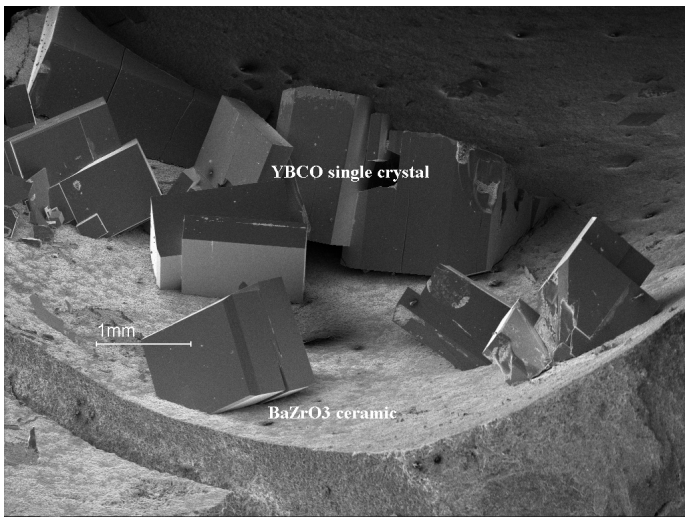

Figure 1: Single crystals of the high temperature superconductor $YBa_2Cu_3O_{7-\delta}$ inside a $BaZrO_3$ crucible.

The purities which can be reached with the use of these crucibles are at least one order of magnitude higher than with commercially available crucibles like ZrO_2 and offer therefore a big advantage in respect with the doping dependence under investigation. To vary the doping in the 123-compounds over a wider range Y-123 crystals with Ca doping will be grown. Simultaneous doping with Ca and oxygen widens the accessible doping range for the 123-compounds. Generally, it should be mentioned that the stoichiometric $YBa_2Cu_3O_{7-\delta}$ compound would be the ideal compound to probe the phase diagram of the high temperature superconductors, however not the whole doping range can be reached using this compound only.

[1] This work is supported by the Deutsche Forschungsgemeinschaft within the coordinated program FOR 538.

Bi-2212 ($Bi_2Sr_2CaCu_2O_8$), Bi-2201 ($Bi_2Sr_2CuO_6$) and Bi-2223($Bi_2Sr_2Ca_2Cu_3O_{10+\delta}$):

Besides the 123-compounds the Bi-based compounds are interesting high-T_c materials which also allow to study the phase diagram in a wider range. The family of the Bi-based high-T_c materials consists of 3 compounds: the so-called 1-layer compound $Bi_2Sr_2CuO_6$ with a transition temperature of $T_c \simeq 10$ K, the 2-layer compound $Bi_2Sr_2CaCu_2O_8$ with a T_c of about 93 K and the 3-layer compound $Bi_2Sr_2Ca_2Cu_3O_{10+\delta}$ with a T_c of about 110 K. The first single crystals of these compounds have been grown in crucibles and the problem of impurities from crucible corrosion has been a problem for these compounds as well.

Figure 2: The 4-mirror image furnace at the WMI. Maximum temperatures up to 2200°C in pressures up to 10 bar.

With the development of mirror furnaces, in which the compounds can be grown containerfree by traveling solvent floating zone technique (TSFZ), a major improvement of the sample quality has been achieved for these compounds.

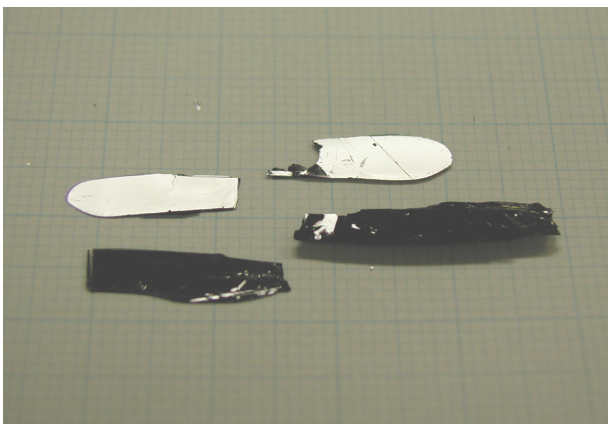

Figure 3: Single crystals of the high temperature superconductor $Bi_2Sr_2CaCu_2O_8$ grown by Traveling-Solvent-Floating-Zone technique inside a mirror furnace.

Especially the compound Bi-2212 allows to cover a broad region on the p-doped region of the phase diagram of the cuprates by doping with Yttrium. We now routinely grow cm-sized crystals of the Bi-2212 and Bi-2201 compound with various doping using the mirror furnace.

214-systems: $La_{2-x}Ce_xCuO_4$, $Nd_{2-x}Ce_xCuO_4$ and $Pr_{2-x}Ce_xCuO_4$:

The choice of possible sample systems on the n-doped side of the phase diagram is restricted to so-called 214-compounds. 214-systems, with the 2 compounds $La_{2-x}Ba_xCuO_4$ und $La_{2-x}Sr_xCuO_4$, were the first cuprate superconductors, which have been found [3]. Coming from the antiferromagnet RE_2CuO_4 increasing the doping with Sr^{2+} on the p-doped or Ce^{4+} on the n-doped side of the phase diagram leads to a formation of a solid solution crystal which turns superconducting when the doping is sufficiently high.

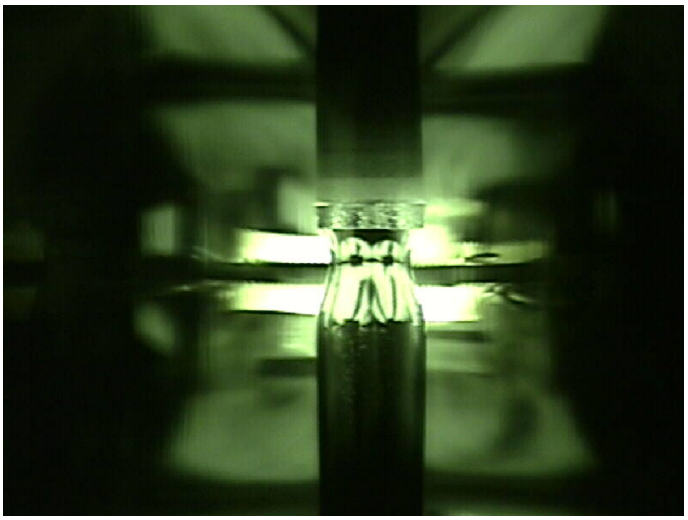

Figure 4: Molten zone during the growth of $La_{2-x}Ce_xCuO_4$ by the Travelling-Solvent-Floating-Zone technique inside a mirror furnace.

The formation of a solid solution for these compounds makes it relatively easy to cover the whole range of the doping, on the other hand it leads to intrinsic homogeneity problems during crystal growth especially for crystals which are grown in a crucible growth process. The quality of these compounds can be highly increased, when they are grown by TSFZ-technique in a mirror furnace. First growth experiments for these 214-systems compounds have also been carried out and we obtained superconducting crystals of both the compounds $La_{2-x}Ce_xCuO_4$ and $Nd_{2-x}Ce_xCuO_4$.

Figure 5: Single crystal of $La_{2-x}Ce_xCuO_4$ grown by the Travelling-Solvent-Floating-Zone

In conclusion all the relevant compounds necessary to study the phase diagram of the cuprate superconductors, both on p- and n-doped side, can now be grown at the crystal laboratory of the Walther-Meißner-Institute.

References

[1] A. Erb et al. *Physica C* **245**, 245 (1995).
[2] A. Erb, E. Walker, R. Flkiger. *Physica C* **258**, 9 (1996).
[3] J. G. Bednorz and K. A. Müller. *Z. Phys. B* **64**, 189 (1986).

Superconducting Qubits: Setup for Experimental Characterization

T. Heimbeck, B. Huber, H. Knoglinger, K. Madek, M. Mariantoni, J. Schuler, R. Stolle, G. Wild, A. Marx, C. Probst, R. Gross [1]

The efforts to establish the experimental environment for characterizing and reading out superconducting flux (phase) qubits within the SFB 631 [1] have been continued (c.f. annual report 2003 [2]). Simultaneously, the fabrication methods for flux (phase) qubits and π phase bias elements have been intensified. A report of the work on the new approach to operate a flux qubit strongly coupled to a microwave resonator (circuit quantum electrodynamics) is given in a separate section in this report.

Experimental setup: Escape of Josephson junction to voltage state

The switching of a superconducting quantum interference device (SQUID), which is coupled to a superconducting flux qubit, to the voltage state can be used to determine the quantum state of the qubit, since the switching current depends on the actual quantum state of the qubit. On the other hand, the switching behavior (escape) of a single Josephson junction to the voltage state can be taken as a sensitive test for the quantum behavior of a macroscopic degree of freedom, namely the phase difference across a current-biased Josephson junction [4]. The rate of escape to the voltage state which can be determined from switching histogram measurements shows a crossover from a thermal activated behavior at higher temperatures to a tunneling behavior at very low temperature. This crossover nicely illustrates the macroscopic quantum behavior of a Josephson junction at low temperatures and can on the other hand be used as a sensitive testbed for the experimental setup especially the shielding against environmental noise. Deviations from the theoretical behavior give evidence that external noise influences the switching of a junction (usually external noise leads to a premature switching and a broadening of the histograms). Furthermore, the experimental technique used in these switching current measurements can be directly utilized for the SQUID readout of a flux qubit.

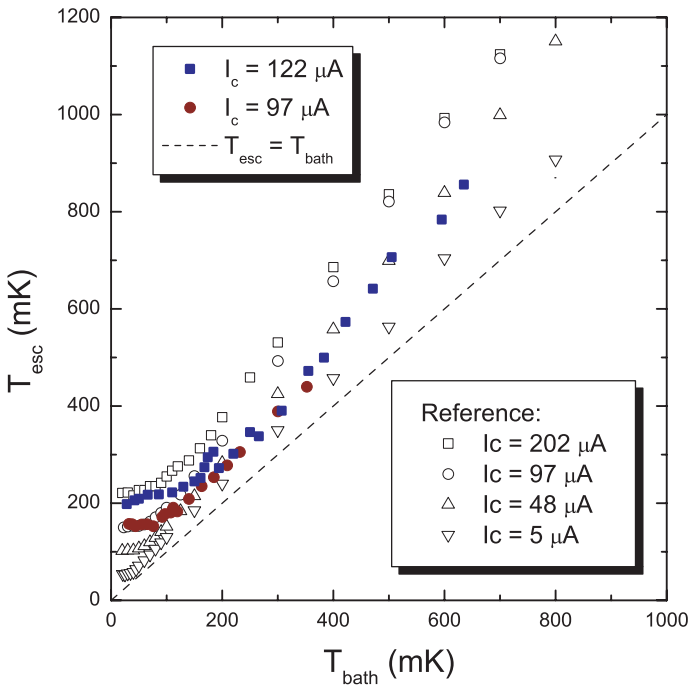

Figure 1: Escape temperature vs bath temperature of a $Nb/AlO_x/Nb$ Josephson junction for two values of the critical current (reference data are from [3])

We have performed extensive investigations of the escape of single $Nb/AlO_x/Nb$ Josephson tunnel junctions to the voltage state. The switching behavior of these junctions has been shown

[1] This work is supported by the Deutsche Forschungsgemeinschaft through SFB 631.

in previous measurements [3] to be in very good agreement with theoretical predictions. The dilution unit used in these experiments (c.f. [2]) has been equipped with several filtering stages for the bias and voltage lines at different temperatures: LCR low-pass filters at room temperature, RC filters at 4 K and at base temperature, and high-frequency copper-in-powder low-pass filters at base temperature (about 25 mK) to suppress the coupling of environmental and thermal noise of the resistive elements at higher temperatures through the bias and voltage lines. Fig. 1 shows the escape temperature T_{esc} which is extracted from switching current histograms (a large number, typically 10^4, measurements of the junction critical current I_c) [4] versus the experimental bath temperature T_{bath}. Our data taken for two different values of the junction critical current are compared to reference data from [3]. The value of the critical current is set by applying an external magnetic field. Obviously, the data show the expected transition from a thermally activated behavior at higher temperatures (here T_{esc} is proportional to T_{bath}) to a tunneling like behavior at low temperatures at a crossover temperature which depends on $I_c(T=0)$. Furthermore, the nice agreement between the two different data sets shows that our experimental setup (especially the filtering) is well suited for the experiments on Josephson junction quantum objects. During these experiments it also turned out that it is crucial to have sufficient thermal anchoring of the biasing lines especially at base temperature.

Recently, this dilution insert has been equipped with a semirigid microwave coaxial line. Here, special care has been taken to prevent heating up the sample stage by thermal conduction along the microwave line. To this end the semirigid line (Keycom ULT-01 above 4 K, Lakeshore CC-SR-10 below 4 K) is thermally anchored using 20 dB attenuators at 4 K and at the still. Initial experiments showed that this thermal anchoring scheme efficiently cools the microwave line. In the ongoing spectroscopic experiments transitions between quantum states in the Josephson junction potential are investigated by applying microwaves.

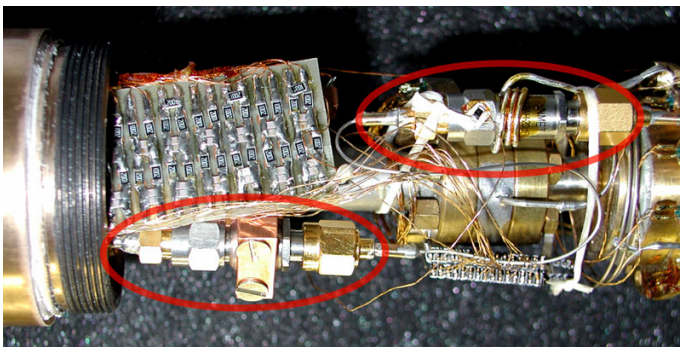

Figure 2: Thermal anchoring of microwave coaxial line by two 20 dB attenuators (red circles).

Experimental setup: new lab with shielded room

An experimental setup for investigating coherent time evolution in flux qubits in the time domain by applying pulsed microwaves is presently developed. The numerous filters and microwave components required for these experiments cannot be accommodated in the compact dilution insert used for the escape rate measurements on the Nb/AlO-junctions. Therefore, an existing dilution unit equipped with a 1 K pot and providing more space for filters and additional elements for cooling down microwave lines and components at 1 K and at base temperature [5] is presently recycled and modified for the requirements of the qubit experiments. This dilution unit will also be used for the cavity electrodynamics experiments with flux qubits strongly coupled to a high quality resonator. The dilution unit will be operated in a shielded room in a recently refurbished laboratory in the WMI basement.

Fabrication of superconducting qubits: Al-technology

Superconducting flux qubits are based on superconducting loops interrupted by one or more Josephson junctions. One approach to realize flux qubits is based on the $Al/AlO_x/Al$ junction technology [6, 7]. Within this approach Josephson junctions with nanometer dimensions, SQUIDs, and qubit structures can be fabricated using the shadow evaporation technique. The operation of superconducting qubits depends crucially on precisely engineered parameters of the Josephson junctions. The properties of the AlO_x tunnel barrier (especially its thickness) are the most sensitive parameters. Therefore, we have been working on optimizing the parameters for the oxidation process to reproducibly fabricate Josephson junctions with well defined coupling energies. To evaluate the junction oxidation process several series of $Al/AlO_x/Al$ Josephson junctions under different oxidation conditions have been realized and characterized.

Fig. 3 shows the current voltage characteristics of a $750 \times 250\,nm^2$ sized Josephson junction at approximately 25 mK. Although the figure shows a clear Josephson behavior with pronounced quasiparticle characteristics, the critical current density is too low to attain sufficiently high tunnel splitting for the qubits. Therefore, the junction optimization process is still intensively pursued. A ^{3}He insert has been put into operation to allow for a rather quick characterization of the junction properties after fabrication.

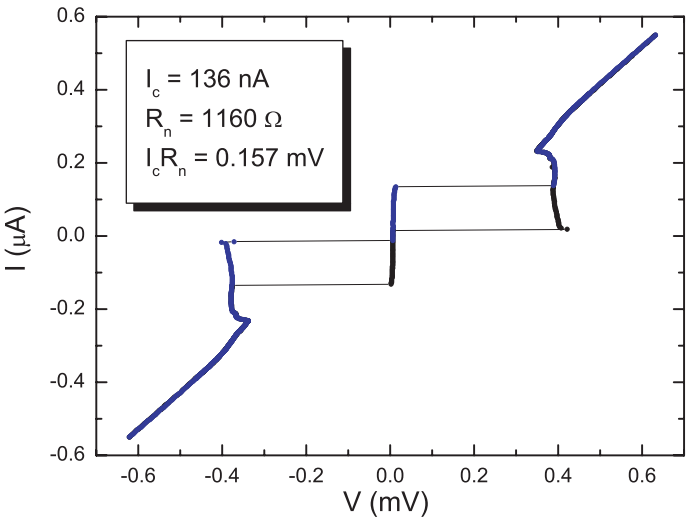

Figure 3: Current voltage characteristics of a $Al/AlO_x/Al$ Josephson junction.

Fabrication of superconducting qubits: π-junctions

All flux qubits which have been realized up to now require an externally applied magnetic flux bias to reach the degeneracy point. Because of rather large loop inductances these qubit structures are susceptible to external magnetic noise. The insertion of π-phase bias elements into the superconducting loops has been suggested to circumvent this problem. Josephson junctions with a ferromagnetic barrier are one way to realize an intrinsic π-phase bias element [8]. The fabrication of these superconductor-ferromagnet-superconductor (SFS) Josephson junctions with π coupling requires a precise tuning of the ferromagnet interlayer thickness. During the last year a UHV sputtering system has been added to the UHV-Laser-MBE system at the WMI (c.f. Fig. 4). This system consists of a UHV chamber where three sputter sources (presently installed targets: Nb, NiPd, Al) and one ion cleaning gun are attached. The sputter chamber is connected to the central transfer chamber of the UHV-Laser-MBE via a transfer tunnel. Thus, it is possible to combine in-situ the sputter technique with the various other options provided by the UHV-MBE cluster (electron beam evaporation, pulsed laser deposition, in-situ surface characterization of sputtered films by UHV AFM/STM).

For realizing π Josephson junctions both a precise control of the ferromagnet (NiPd) interlayer thickness and the quality of the involved interfaces are crucial. Therefore, after determining the

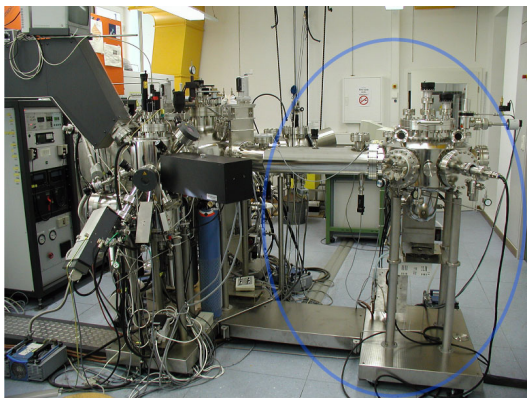

Figure 4: New sputtering system with 3 sputter sources (Nb, NiPd, Al) and argon ion cleaning gun (blue circle) attached to the UHV-Laser-MBE system via a tunnel containing the transfer system.

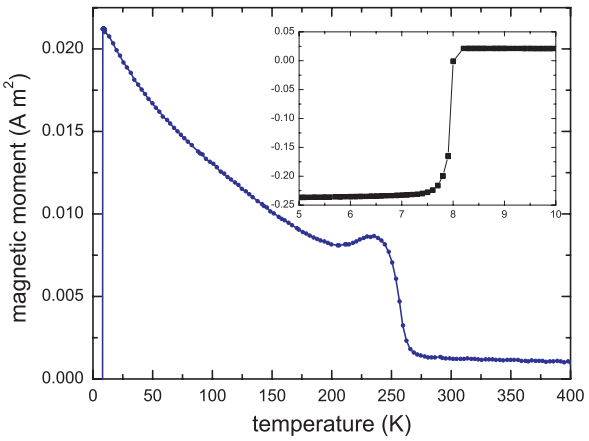

Figure 5: Temperature dependece of the magnetic moment of a Nb(49 nm)/NiPd(9 nm)/Nb(50 nm) multilayer. The inset shows the superconducting transition of the Nb layers.

individual sputter rates for the different materials we have started optimizing the process parameters to obtain thin films with smooth surfaces. The surface quality is quantified using UHV AFM and x-ray reflectometry. The sputtered Nb films turned out to be very smooth with a rms surface roughness well below 1 nm for a film thickness of about 50 nm. The superconducting critical temperature determined with the SQUID magnetometer was well above 8 K. The ferromagnet NiPd (18% weight percent Ni) layers show a comparable surface smoothness, the Curie temperature of the films was approximately 360 K. Fig. 5 shows the temperature dependence of the magnetization of a Nb(49 nm)/NiPd(9 nm)/Nb(50 nm) multilayer where initially the sample has been cooled down to 10 K in a field of $H = 70$ kOe to magnetize the NiPd layer then the sample was further cooled down to 5 K in zero field to avoid trapping vortices in the Nb layer when cooling through the superconducting transition temperature. The magnetization curve was recorded in an applied field of 10 Oe. The figure clearly shows the superconducting transition of the Nb layers above 8 K as well as the phase transition of the thin ferromagnetic interlayer at about 265 K. These results show that the multilayers are good candidates to fabricate Josephson junctions with π coupling [9]. The next step is to develop the process to laterally define Josephson junctions in these multilayers for transport measurements.

References

[1] *see* http://www.wmi.badw-muenchen.de/SFB631/
[2] Annual report 2003, Walther-Meissner-Institut, http://www.wmi.badw.de/ueberuns/jahresberichte/2003.pdf
[3] T. Bauch, Chalmers University of Technology, private communication, 2003.
[4] J. M. Martinis, M. H. Devoret, and J. Clarke, Phys. Rev. B **35**, 4682 (1987).
[5] constructed by K. Neumaier several years back
[6] J. E. Mooij, T. P. Orlando, L. S. Levitov, L. Tian, and C. H. van der Wal, S. Lloyd, Science **285**, 1036 (1999).
[7] I. Chiorescu, Y. Nakamura, C. J. P. M. Harmans, and J. E. Mooij, Science **299**, 1869 (2003).
[8] A. I. Budzdin et al., Sov. Phys. JETP **74**, 124 (1992).
[9] T. Kontos, M. Aprili, J. Lesueur, F. Geneet, B. Stephanidis, and R. Boursier, Phys. Rev. Lett. **89**, 137007 (2002).

Automatization of the Pulsed Laser Deposition Process

K.-W. Nielsen and T. Brenninger [1]

Pulsed Laser Deposition (PLD) is a powerful method for the epitaxial growth of oxide thin films and heterostructures. Fig. 1 shows the scheme of the PLD process. The short pulses of an excimer laser (Lambda Physik, Compex M201) hit the target material. Due to the high power density the target material is ablated and a plasma plume is generated containing the free atoms of the target material. Above the target a substrate is fixed. The free atoms arriving at the substrate surface have a certain probability to stick on the surface and form a thin film. In our case we are interested in the epitaxial growth, where a crystalline film forms on the substrate with the crystalline orientation predetermined by the substrate.

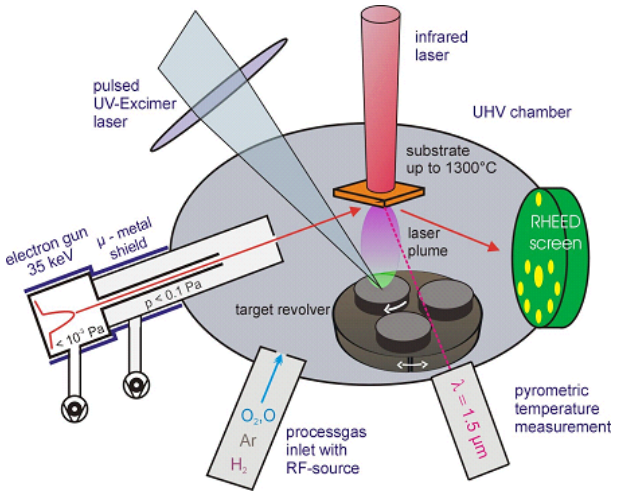

Figure 1: Schematic representation of the Pulsed Laser Deposition (PLD) process.

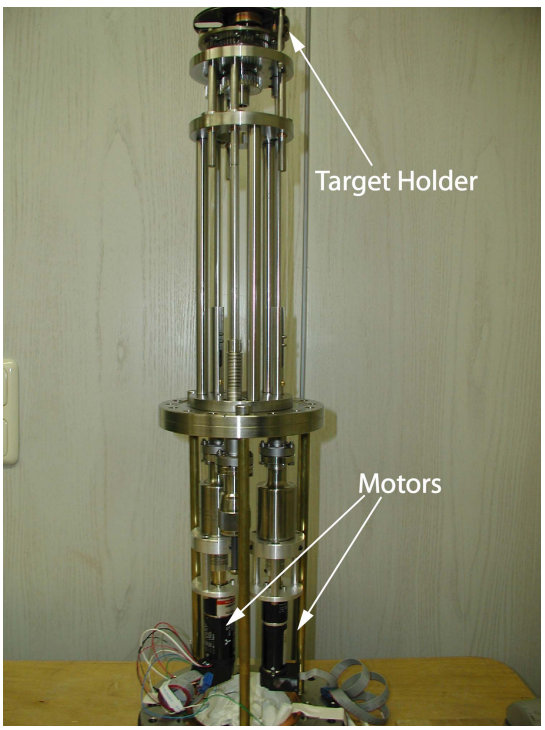

Figure 2: New target holder construction.

The substrate temperature can be varied by an infrared laser (Surface LH90) irradiating the substrate from the back-side. The substrate temperature is determined by a pyrometer. In this way the substrate heating system and temperature control systems consist only of optical components. This reduces contamination problems in the UHV chamber caused e.g. by radiation heaters positioned inside the chamber. The temperature of the substrate is one of deposition parameters, which include deposition atmosphere and pressure, laser power and repetition rate etc. The deposition parameter determine the growth mode of the films and the resulting crystalline quality.

[1]This work is supported by the Deutsche Forschungsgemeinschaft within the coordinated program SPP 1157 (project no. GR 1132/13-1).

A particular aspect of PLD is that it works far away from thermal equilibrium due to the highly excited species present in the plasma plume. This is advantageous for the growth of materials that are not thermodynamically stable. A specific advantage of the PLD process is the fact that stoichiometric targets can be used and that there is a good transfer of the target composition to the growing film in most cases. In contrast to Molecular Beam Epitaxy this allows the growth of complex materials like Sr_2CrWO_6 without expensive rate control. Furthermore, modern laser can provide a high energy density allowing for the ablation of even very refractory materials like oxides.

Over the recent years the PLD process has been improved considerably. In particular, the use of in-situ RHEED control of the growth process allows the deposition of complicated heterostructures in a layer-by-layer mode. However, the deposition of layer structures with a large number of layers requires the automatization of the deposition process in order to avoid artefacts introduced by the operator. Therefore, we started to automatize the PLD process to reach both high precision and good reproducibility. Therefore, stepper motors from Maxon Motors were installed at the lens system, the mirror, the target height and rotation control. Each of the motors is equipped with a high resolution positioning system (Maxon Motors EPOS). Furthermore, a new target holder was designed, which is shown in Figs. 2 and 3. With the new construction of the target exchange it is now possible to control the target position more precisely. Moreover, the new systems allows to install a motor control, because the cogwheels do no longer get stuck in contrast to the old holder. Another new feature is the possibility to "wobble". Here, wobbling means that in addition to the simple rotation of the target also a small oscillatory movement sidewards takes place. In this way the whole area of the target is hit by the laser and can be used for the deposition process.

Figure 3: Upper part of the new target holder.

The control software is based on LabView 7.1 from National Instruments and it will be capable to control the whole deposition process. The user can enter the deposition parameters and the PLD growth process of the thin film or heterostructure will run automatically. We expect that this development will further improve the PLD deposition process and will lead to a better control and reproducibility during the growth of complex heterostructures.

Epitaxial growth of electron doped double perovskites $La_xSr_{2-x}CrWO_6$

P. Majewski, R. Geißler, A. Boger, S. Geprägs, A. Erb, M. Opel, L. Alff, and R. Gross [1]

Ferromagnetic double perovskites have attracted renewed interest due to the fact that they combine high Curie temperatures T_C and half-metallicity [1]. Recently, for the double perovskite Sr_2FeMoO_6 it was found that T_C can be increased by about 80 K when 25% of the Sr^{2+} ions are replaced by La^{3+}, i.e. by electron doping [2, 3, 4, 5]. However, for the material Sr_2CrWO_6 the preferential formation of the $LaCrO_3$ impurity phase during high temperature synthesis prevents significant doping [6] in polycrystalline bulk samples. Here, we show that the La-doped compound $La_xSr_{2-x}CrWO_6$ can be grown as high quality epitaxial thin film using pulsed laser deposition (PLD) as this growth process is far from thermal equilibrium.

$La_xA_{2-x}CrWO_6$ (A = Sr, Ca) thin films were deposited by PLD from stoichiometric polycrystalline targets on (001) atomically flat HF etched and thermally annealed (1000°C for 4 hours in oxygen flow) $SrTiO_3$ substrates using a 248 nm KrF excimer laser [7]. Reflection high energy electron diffraction (RHEED) intensity oscillations [8] were recorded during the growth of *c*-axis oriented $La_xSr_{2-x}CrWO_6$ films [9]. The layer-by-layer or Frank-van der Merwe growth mode is achieved for a substrate temperature $T_S = 800$°C, a pressure of $p = 6 \times 10^{-4}$ Torr (99% Ar, 1% oxygen and for pure Ar), a laser repetition rate of 2 Hz, and a laser energy density on the target of about 1.3 J/cm^2.

Fig. 1 shows a $\theta - 2\theta$ X-ray scan for a 150 nm thick Sr_2CrWO_6 film. The full width at half maximum (FWHM) of the rocking curve of the Sr_2CrWO_6 (004) peak is 0.024°. The small mosaic spread and good crystalline quality are further demonstrated by the observation of Laue oscillations around the (004) peak (see inset). In the $\theta - 2\theta$ scan no parasitic phases could be detected. This suggests that one can grow Sr_2CrWO_6 thin films with high phase purity in contrast to bulk samples where the formation of Sr-W-oxides (mostly Sr_2WO_5 and Sr_3WO_6) is difficult to avoid. This is confirmed by preliminary transmission electron microscopy data of thin films, where no inclusions of parasitic phases could be found [10]. The *c*-axis lattice constant was determined to be 7.914 Å. The lattice mismatch to $SrTiO_3$ is negligible.

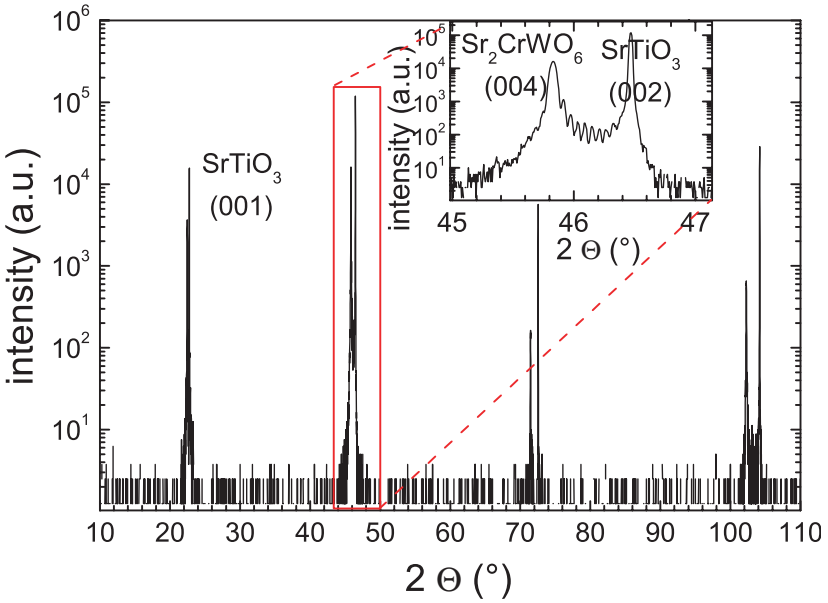

Figure 1: $\theta - 2\theta$ X-ray scan for a Sr_2CrWO_6 thin film. The inset shows the region around the Sr_2CrWO_6 (004) peak on an enlarged scale.

Fig. 2 clearly demonstrates that we succeeded in the fabrication of high quality epitaxial films of the compound $La_xSr_{2-x}CrWO_6$ (here an example with $x = 0.5$) with good phase purity. In

[1] This work is supported by the BMBF (project no. 13N8279).

particular, we found no peak broadening due to the presence of $LaCrO_3$ as it is the case for polycrystalline samples [6].

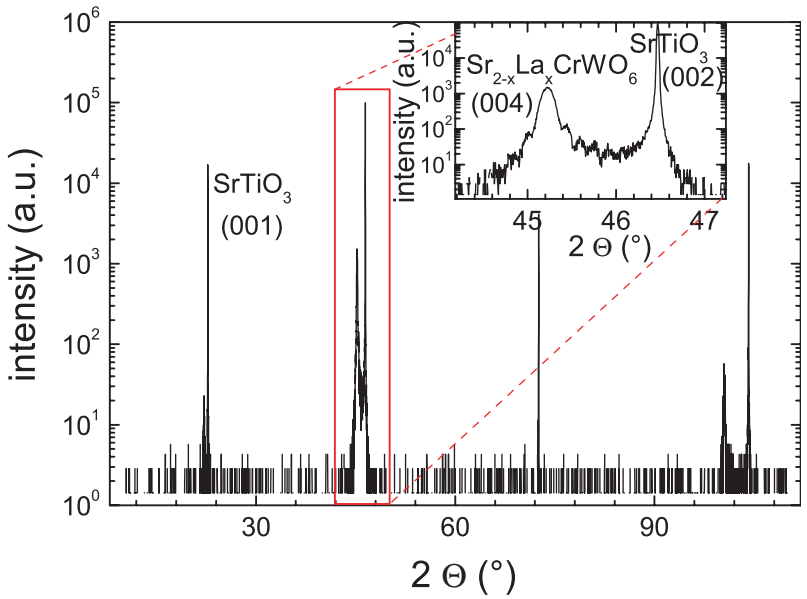

Figure 2: $\theta - 2\theta$ X-ray scan for a $La_{0.5}Sr_{1.5}CrWO_6$ thin film. The inset shows the region around the $La_{0.5}Sr_{1.5}CrWO_6$ (004) peak on an enlarged scale.

The 90 nm thick film has a FWHM of the rocking curve of the (004) peak of $\approx 0.036°$ which is slightly larger than for the undoped compound (similar results were obtained for samples with $x = 0.3$). The small increase in the mosaic spread may be related to the structural distortions induced by La-doping. The growth parameters correspond to those used for the undoped film. The c-axis parameter of the sample shown in fig. 2 (8.00 Å) is enlarged compared to the undoped compound. This increase of the lattice parameter with increasing x has also been observed for La-doped Sr_2FeMoO_6 bulk samples [2] and is most likely of electronic nature. Note that steric effects should result in the opposite behavior, since the ionic radius of La^{3+} is smaller than that of the substituted Sr^{2+}. However, the surplus charge increases the valence of the metal ions thereby increasing their radius.

Fig. 3 gives an overview about the c-axis lattice parameters obtained from $La_xSr_{2-x}CrWO_6$ for $x = 0$, $x = 0.3$, and $x = 0.5$. The spread in the data is most likely related to the different amounts of strain relaxation (films with different thickness are included) and differences in oxygen content. If the samples are grown in a more reducing atmosphere, the c-axis parameter is larger [11]. Figure 3 clearly shows that the increase of c with doping x is significant. The mean values for c are 7.91 Å ($x = 0$), 7.95 Å ($x = 0.3$), and 8.00 Å ($x = 0.5$).

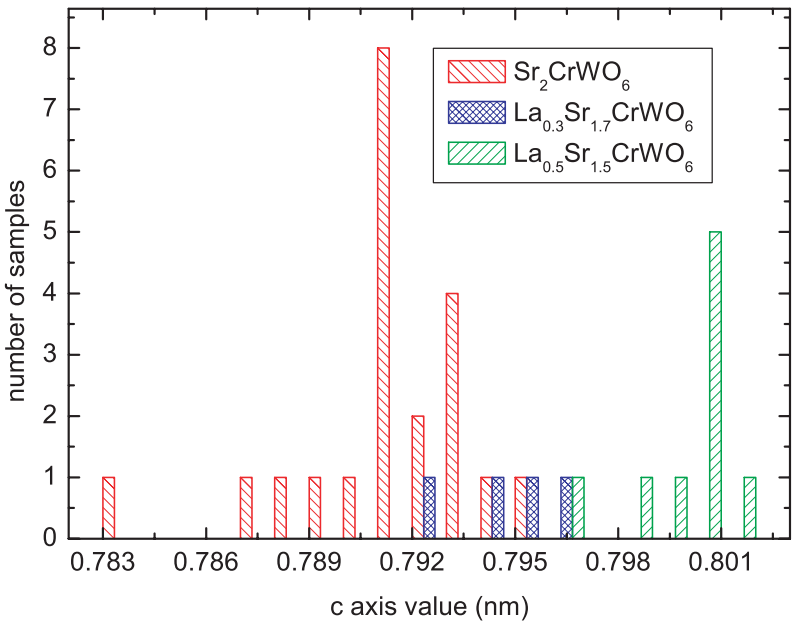

Figure 3: Histogram of the c-axis lattice parameters obtained from various $La_xSr_{2-x}CrWO_6$ films for $x = 0$, $x = 0.3$ and $x = 0.5$. The shift of c with electron doping is evident.

In summary, we succeeded in the fabrication of high quality epitaxial $La_xSr_{2-x}CrWO_6$ films. This will allow to study the

doping dependence of $T_C(x)$ in the Cr-W-system. Preliminary results show that T_C clearly exceeds 400 K for $x = 0 \ldots 0.5$.

References

[1] K.-I. Kobayashi, T. Kimura, H. Sawada, K. Terakura, and Y. Tokura, Nature **395**, 677 (1998).
[2] J. Navarro, C. Frontera, Ll. Balcells, B. Martínez, and J. Fontcuberta, Phys. Rev. B **64**, 092411 (2001).
[3] D. Serrate, J.M. De Teresa, J. Blasco, M.R. Ibarra, L. Morellón, and C. Ritter, Appl. Phys. Lett. **80**, 4573 (2002).
[4] C. Frontera, D. Rubi, J. Navarro, J.L. García-Muñoz, J. Fontcuberta, and C. Ritter, Phys. Rev. B **68**, 012412 (2003).
[5] J. Navarro, J. Nogués, J.S. Muñoz, and J. Fontcuberta, Phys. Rev. B **67**, 174416 (2003).
[6] S. Geprägs, P. Majewski, Y. Krockenberger, M. Opel, A. Erb, L. Alff, R. Gross, C. Ritter, J. Simon, and W. Mader, to be published.
[7] R. Gross, J. Klein, B. Wiedenhorst, C. Höfener, U. Schoop, J. B. Philipp, M. Schonecke, F. Herbstritt, L. Alff, Yafeng Lu, A. Marx, S. Schymon, S. Thienhaus, W. Mader, in *Superconducting and Related Oxides: Physics and Nanoengineering IV*, D. Pavuna and I. Bosovic eds., SPIE Conf. Proc. **Vol. 4058** (2000), pp. 278–294.
[8] J. Klein, C. Höfener, L. Alff, and R. Gross, Supercond. Sci. Technol. **12**, 1023 (1999), see also J. Magn. Magn. Mater. **211**, 9 (2000).
[9] P. Majewski, S. Geprägs, A. Boger, M. Opel, L. Alff, and R. Gross, J. Magn. Magn. Mat., accepted for publication (2004).
[10] J.B. Philipp, P. Majewski, L. Alff, A. Erb, R. Gross, T. Graf, M.S. Brandt, J. Simon, T. Walther, W. Mader, D. Topwal, and D.D. Sarma, Phys. Rev. B **68**, 144431 (2003).
[11] J.B. Philipp, D. Reisinger, M. Schonecke, M. Opel, A. Marx, A. Erb, L. Alff, and R. Gross, J. Appl. Phys. **93**, 6853 (2003).

Cryogen-free dilution refrigerator precooled by pulse-tube cooler with non-magnetic regenerator

K. Uhlig

In last year's report we described a "dry" ^{3}He/^{4}He-dilution refrigerator (DR) where a commercial closed-cycle refrigerator, a so-called pulse-tube refrigerator (PTR), precooled the dilution unit. The base temperature of the cooler was 4.3 mK [1, 2]. We cannot emphasize enough the advantages of this type of refrigerator compared to standard dilution refrigerators with liquid helium precooling.

As cryostats with closed-cycle precooling do not require cryo-liquids, they are especially efficient in the cooldown process. To cool a mid-size helium cryostat from room temperature to 4.2 K you have to spend about a day, whereas the cooldown with a PTR is automatic and can be done overnight. And in long-term experiments there are no interruptions of the experiments due to helium re-fills, and electrical leads do not change resistance or capacitance due to changes of the helium level in the cryostat. There are no frosted or wet recovery lines after helium transfers, either. In addition, the PTR-DR allows for a short and compact construction of the cryostat which is a clear advantage when the cryostat is mounted in the lab where the height of the lab is limited. You don't need a helium dewar with helium transfer line; instead, you use a simple vacuum can. To change samples it is not necessary to lower the entire helium dewar, but instead it is sufficient to open the lower part of the vacuum can. You don't need a charcoal trap with liquid nitrogen with this cryostat. And at the first stage at a fixed temperature of about 50 K one has a possibility to heat-sink electrical leads or amplifiers or filters at a fixed temperature. At last, the PTR can be operated through the internet and thus the entire cryostat can be internet controlled.

The important advantage of PTRs versus their closed-cycle brethren is that they have no moving parts inside, and so they do not vibrate like other types of closed-cycle refrigerators. There is one item, though, with PTRs that could be a problem in high sensitivity experiments (NMR, MRI, Squid). This concerns the fact that the material of the low temperature regenerator consists of a magnetic rare-earth compound (Er_3Ni) which produces a small magnetic field of about 20 nT. This field oscillates with the frequency of the gas flow of the PTR (1 Hz) due to temperature changes of the regenerator.

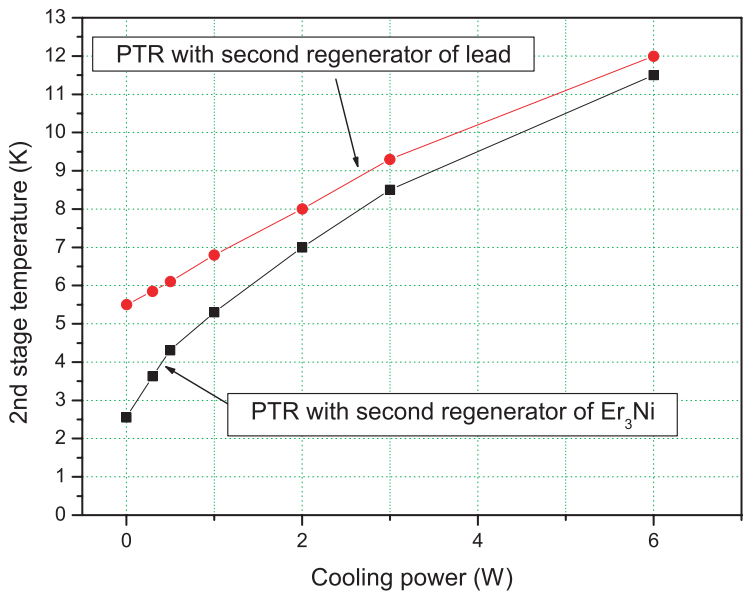

Figure 1: Final temperatures of the 2nd stage of two PTRs with and without rare-earth compounds in their 2nd regenerator. The final temperature of the new PTR with lead regenerator is 5.5 K, whereas the one with Er_3Ni reaches 2.5 K.

It was the goal of the experiment described below to show

that a DR can be precooled by a PTR with a non-magnetic regenerator consisting of lead in its second stage, even though the cooling capacity of this PTR is hindered considerably by this type of regenerator. In Fig. 1 the temperature of the second stage of two PTRs is given as a function of the cooling power where the black curve is for a PTR with Er_3Ni in its second regenerator and the red curve for one with lead. The two PTRs which, apart from their second regenerators, are identical, have very different cooling capacities at their lowest temperatures.

In Fig. 2 a cross section of the cryostat is depicted which shows the relative positions of its most important components. The ^{3}He gas enters the cryostat through a charcoal trap which is attached to the first stage of the PTR. Then the gas flow is cooled at its second stage in a heat exchanger and in the subsequent Joule-Thomson-stage before it enters the dilution unit where the lowest temperature is reached. As the final temperature of the new PTR is about 3 K higher than that of the PTR used thus far, the Joule-Thomson heat exchanger has to transfer the corresponding amount of enthalpy in order to get similar precooling conditions of the ^{3}He-flow before it is expanded in the impedance and enters the dilution unit.

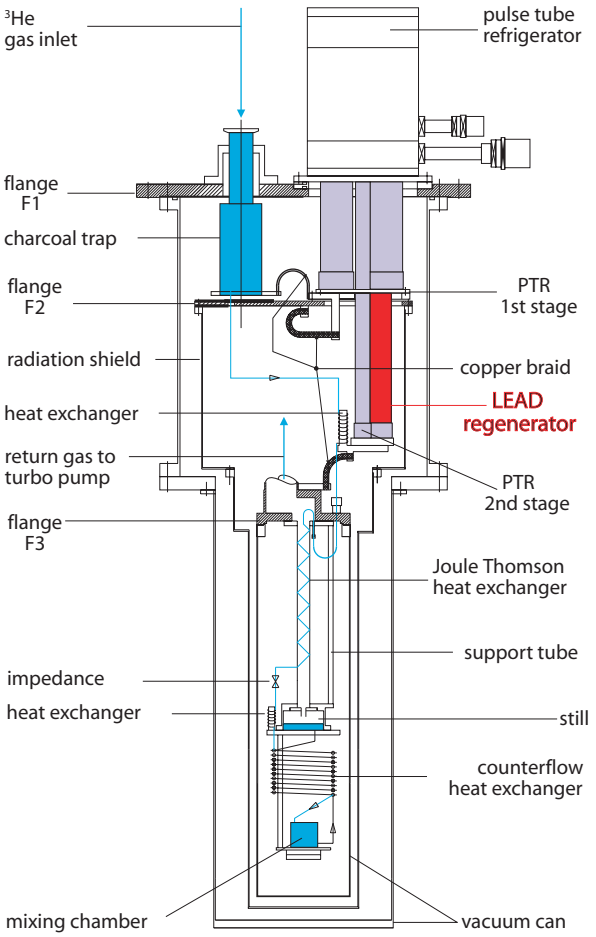

Figure 2: Cross-sectional view of the cryostat. The PTR, the Joule-Thomson refrigerator and the dilution unit are the most important components of the fridge. The second regenerator of the PTR is marked in red.

In Fig. 3 two cooldown curves of our cryostat are shown, one for the PTR with rare-earth regenerator, and one for the new PTR with lead regenerator. Whereas the cool-downs of the first stages where a big radiation shield is attached, are identical as expected, we find the temperature of the second stage of the PTR with lead regenerator about 3.5 K higher than the one with the Er_3Ni regenerator; the second stage cools the vacuum can with the dilution unit inside.

After the cryostat is cooled below 10 K, the ^{3}He/^{4}He mash is condensed into the dilution unit with a pressure of 5 bar at the inlet of the cryostat - the cryostat now works like a miniature Joule-Thomson liquefier where the liquefied mash accrues in the dilution unit, and the enthalpy of the cold return gas is used to precool the inflowing high pressure gas. The rate of liquefaction

is 12 std.l./hour or 26% of the inflowing stream with the new PTR (it was 28 std.l./hour or 53% with the old one).

After the condensation of the ^{3}He/^{4}He gas the dilution unit is operated at inlet pressures of 0.5 bar to 0.9 bar, depending on the ^{3}He flow. These pressures are one-to-one with the old PTR; however, the cooling capacity of the still, and herewith the heat supplied to it, are reduced. A more detailed thermodynamic description of the conditions in the Joule-Thomson heat exchanger will be given in an upcoming publication. The lowest temperatures in the mixing chamber are approached after about 4 hours of running.

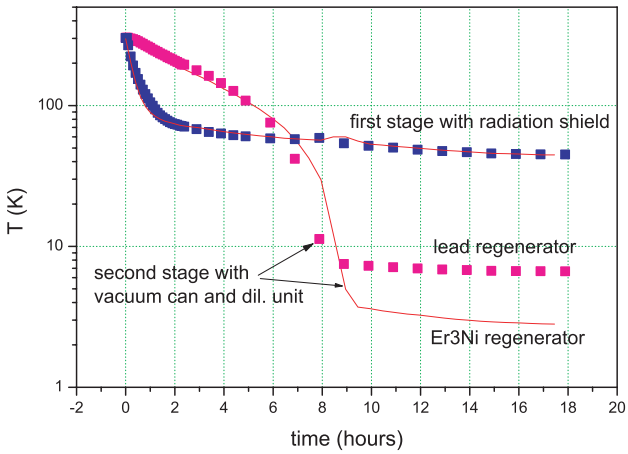

Figure 3: Cool-downs for our cryostat. Squares are for the PTR with lead regenerator, lines for the PTR with rare-earth regenerator. After about nine hours the cryostat is ready for the condensation of the helium mash.

In Fig. 4 the base temperatures of the cryostat are depicted as a function of the ^{3}He flow. In our dilution unit the flow is divided in two streams, and these streams are diluted in two separate mixing chambers; the first stream cools the second one so that a lower final temperature is reached there. A description of this so-called double mixing chamber can be found in [3]. For thermometry a ^{3}He melting curve thermometer was used [4, 5] to measure the temperatures of the second mixing chamber, and calibrated thick-film resistors [6] for all other low temperature thermometers.

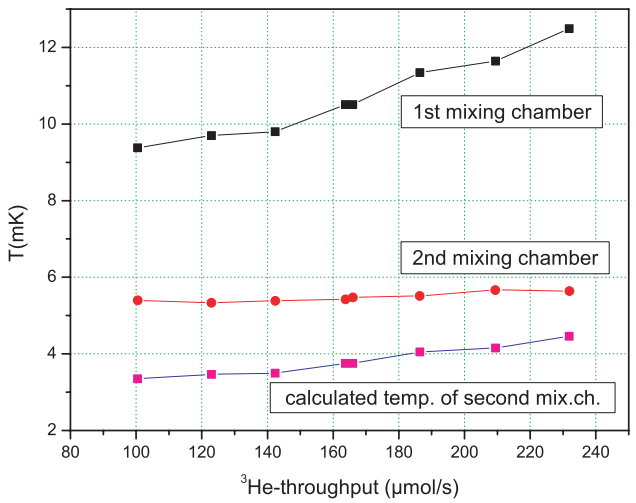

Figure 4: Final temperatures of the dilution fridge. The 1st mixing chamber precools the ^{3}He stream of the second mixing chamber so that lower temperatures can be reached there. Also shown is the calculated base temperature of the 2nd mixing chamber in the case of a vanishing heat leak.

Using the theoretical description of the double mixing chamber one can derive a curve for the temperature of the second mixing chamber for the case of a vanishing external heat leak. In our case final temperatures of below 4 mK would be expected. From the temperature gap between this curve and the measured one (red curve in Fig. 4) the spurious heat leak can be calculated and is found to be 0.16 μW; it is constant for all ^{3}He throughputs. The source of the heat leak has not been tracked down unambiguously, but it is probably the sum of viscous heating, heat conduction in the liquid, dissipation by vortices and possibly heating caused by vibrations of the PTR. The vibrations of the compressor could be responsible for those vibrations if they are transferred to the PTR by the metal pressure lines. A better PTR where the pulse-tubes and the gas distributor are separated by a soft plastic line would solve that problem.

In summary, we have demonstrated that a PTR with a simple lead regenerator at the second stage is suited to precool a DR if the small magnetic fields of the second regenerator pose a problem for an experiment. In addition, this type of PTR offers a welcome price advantage compared to a standard PTR.

References

[1] K. Uhlig, *^{3}He/^{4}He dilution refrigerator with pulse-tube refrigerator precooling*, Cryogenics **42**, 73 (2002).
[2] K. Uhlig, *"Dry" dilution refrigerator with pulse-tube precooling*, Cryogenics **44**, 53 (2004).
[3] G. Coops, A.T.A.M. de Waele, H.M. Gijsman, *The multiple mixing chamber*, Cryogenics **19**, 659 (1979).
[4] D.S. Greywall, *3He specific heat and thermometry at millikelvin temperatures*, Phys Rev B **33**, 7520 (1986).
[5] R.L. Rusby et al., *The Provisional Low Temperature Scale from 0.9 mK to 1K*, PLTS-2000. AIP Conf. Proc. **684**, 77 (2003).
[6] K. Uhlig, *Magnetoresistance of thick-film chip resistors at millikelvin temperatures*, Cryogenics **35**, 525 (1995).

The New Helium-Liquifier at the WMI

J. Höss, K. Neumaier, W. Biberacher, R. Gross

The liquefaction of helium has a longstanding tradition at the Walther-Meißner-Institute. It was Walther Meißner, who built the first helium liquefier in Germany in Berlin from 1922 to 1925 (it was the third system of its kind all over the world). In 1934, he moved to the Technical High School of Munich and installed the first helium liquefier in Munich. During World War II his institute was transferred to Herrsching for security reasons. In 1946, W. Meissner founded the Commission for Low Temperature Research of the Bavarian Academy of Sciences, which took over the experimental facilities at Herrsching together with the helium liquefier. This machine was very difficult to handle, but under optimal conditions it could deliver 3 l of liquid per hour. The further development of liquefier machines was one of the main research projects of Walther Meißner and in the following years important contributions on this subject came from him and his coworkers Franz Xaver Eder, Robert Doll and Werner Wiedemann. When the Commission laboratory moved in 1967 from Herrsching to the present building of the Walther-Meißner-Institute at Garching, it became an official task specified in the statutes of the Commission for Low Temperature Research of the Bavarian Academy of Sciences to supply helium also to the research institutes at both Munich universities. At present around 20 laboratories are supplied with liquid helium (about 150.000 l per year).

Figure 1: The new screw compressor in the compressor hall.

Since a few decades, helium liquefiers are no longer homemade by research groups but have developed to industrial products. In 1982, the WMI obtained a new system supplied by the Swiss company Sulzer AG. It was planned to operate for 10 years, but due to the perfect maintenance of the system by the staff of the WMI and the high quality of the product it has been running for more than 22 years without serious problems. Of course it became more and more difficult to get spare parts for this system. Therefore, the WMI started to plan the installation of a new system in 2001. The system requirements and the liquefaction power were chosen according to the needs of the involved research institutes. In average, an annual consumption of 150 000 to 200 000 l of liquid helium is expected for the next 10 to 20 years. The new liquefaction system has been financed to equal parts by the State of Bavaria and the German Federal Government (within the program "Hochschulbauförderungsgesetz"). After the money was granted in 2003, the new system could be ordered in autumn of 2003 at the company Linde Kryotechnik AG: a new version of the TCF 20 liquefier. The system was delivered at the end of August 2004 and

became fully operative in December 2004.

The most important components of the new liquefier are the following: The helium gas coming from the gas storage tank first enters a gas drier. The design of this helium drier was initiated by W. Wiedemann at the WMI around 1990 and proved to be very effective with the old system. The liquefier itself consists of a screw-type compressor followed by an oil separator and the cold box with integrated freeze-out purifier to remove further contaminants from the helium. Cooling and liquefaction of the compressed gas take place in two gas-bearing expansion turbines followed by a pneumatically controlled Joule-Thomson valve followed by an ejector. The liquid Helium is transferred to the existing 5000 l tank. The liquefier is provided with a Siemens S7-400 automatic control and monitoring system connected to a PC for visualization and the possibility of remote control via modem. The liquid helium output is approximately 30 l/h and can be increased to more than 60 l/h by precooling with liquid nitrogen.

Figure 2: The liquefier hall of the WMI with the new coldbox and control unit (blue coloured,) the storage tank with transfer system and the old liquefier (yellow)

The liquefier with ejector allows to keep the storage tank at atmospheric pressure. This is an important requirement for optimal functioning of the transfer system, developed at the WMI by W. Wiedemann, R. Doll and H. Berndt, whose main part is a helium pump with magnetic bearing operating at 4.2 K. It allows to transfer the liquid helium to the transport vessels without considerable drop in pressure and at the same time the cold gas from the transport vessel to return the storage tank. The use of this system increases the efficiency of the helium liquefier by 20-25% compared to conventional ones.

Experimental Facilities and Infrastructure

Within the last years, several new experimental facilities and various components of the technical infrastructure have been installed at the Walther-Meißner-Institute. On the following pages a brief overview is given on the main equipment and techniques that are available at the Walther-Meißner-Institute at present.

UHV-Laser-MBE

The Walther-Meißner-Institute operates a UHV-Laser-Molecular Beam Epitaxy (L-MBE) system for the growth of complex oxide heterostructures. The system has been designed to meet the special requirements of oxide epitaxy. The UHV cluster tool consists of the following main components:

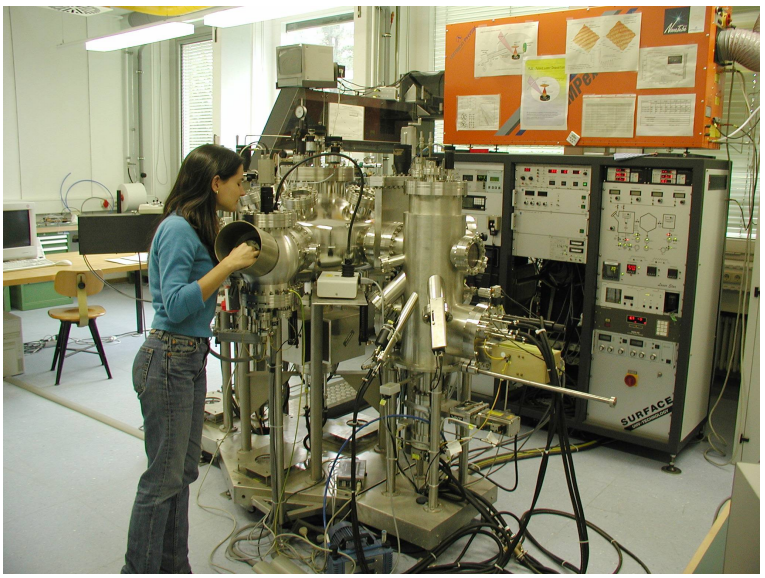

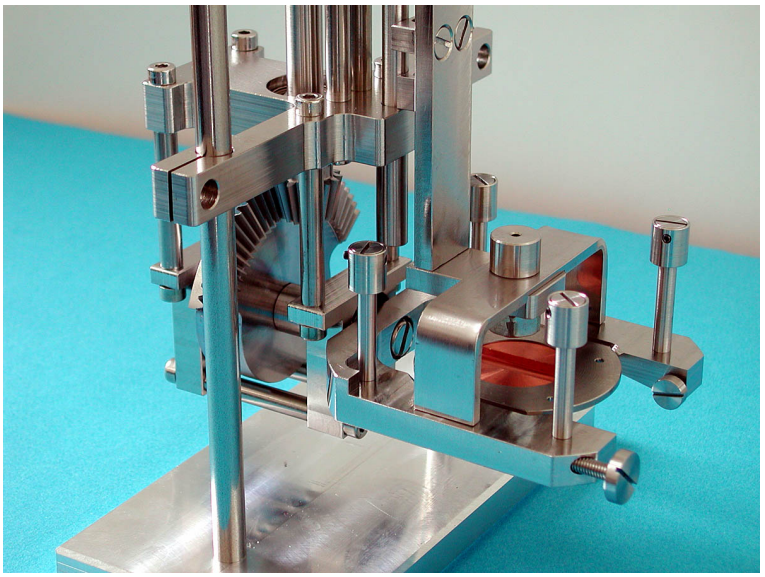

Figure 1: Top: UHV-Laser-Molecular Beam Epitaxy System. Bottom: Sample holder for metallization chamber allowing for evaporation under different angles.

- central transfer chamber.
- load-lock chamber with heater system for substrate annealing.
- laser deposition chamber with in-situ reflection high energy electron diffraction (RHEED) system, laser substrate heating system, and atomic oxygen source. The RHEED system has been modified to allow for the operation at high oxygen partial pressure up to 0.5 mbar.
- surface characterization chamber with UHV scanning force microscope (Omicron).
- metallization chamber with a four heart electron gun system and a liquid nitrogen cooled sample stage. The sample holder can be tilt for shadow evaporation.
- KrF excimer laser.

The system is used for the growth of complex oxide heterostructures consisting of supercon-

ducting, magnetic and dielectric materials such as the high-temperature superconductors, the doped manganites, the double perovskites, magnetite etc..

During 2002 and 2003, the laser molecular beam epitaxy system (laser-MBE) which was installed at the Walther-Meißner-Institut during 2001 has been extended and modified. In particular, the substrate heating system and the temperature control unit was changed from a resistive radiation heater to a new infrared laser heating system (see Fig. 3, left) including a pyrometer for determining the sample temperature. In addition, a source for atomic oxygen has been added. The main advantage of the new heating system is that only the substrate is heated while the surrounding parts are hardly affected (Fig. 3, right). In this way one can achieve an essentially better vacuum at temperatures well above 1000°C. The achievable substrate temperature is limited by the melting point and the size of the substrate material (approx. 1410°C for a 5×5 mm^2 silicon substrate). The laser heating system has already been successfully used for removing the amorphous silicon oxide layer form the surface of silicon substrates at 1150°C. This is required for the epitaxial growth of oxide thin films on this substrate.

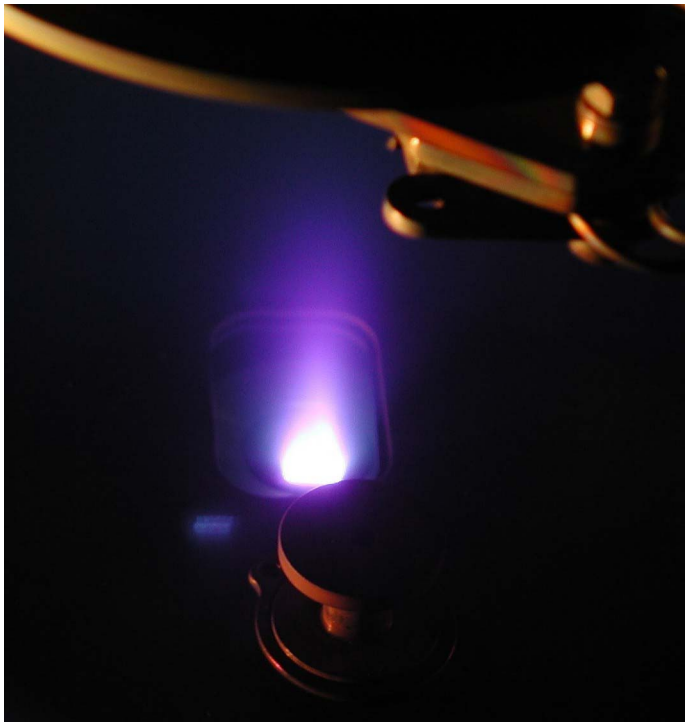

Figure 2: Pulsed Laser Deposition (PLD): When the pulse of the UV laser (KrF excimer laser, 248 nm) hits the target, the target material is ablated and the so-called laser "plume" containing highly excited atoms and molecules is formed.

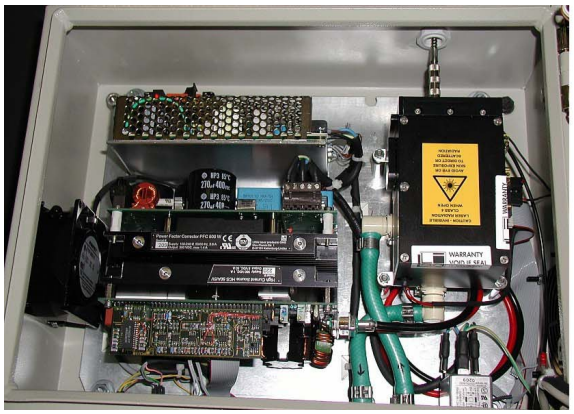

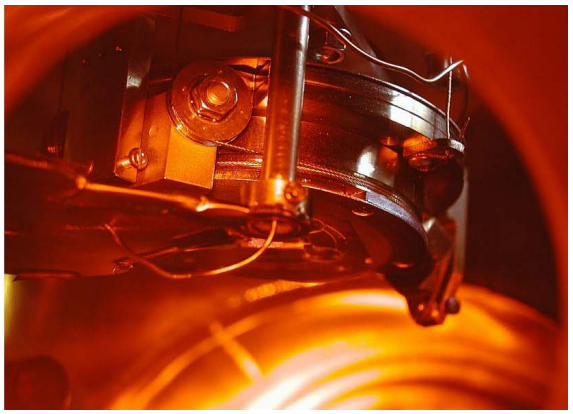

Figure 3: Components of the laser heating system: The substrate is heated using an IR diode laser head that is located in a separate box far away from the deposition chamber (left). The laser light is brought to the substrate (right) via an optical fiber.

Single Crystal Growth and Synthesis of Bulk Materials

Transition metal oxides are of great interest due to their various interesting physical properties (e.g. high temperature superconductivity, colossal magnetoresistance, ferroelectricity, nonlinear optical properties etc.) and their high potential for applications. In the last 2 years a new laboratory for the synthesis of bulk materials and single crystals has been built up at the WMI. With the installation of a four-mirror image furnace the laboratory is now fully operational. With this furnace crystals of various high temperature superconducting materials or other transition metal oxides can be grown as single crystals using the traveling solvent floating zone technique. The furnace consists basically of 4 elliptical mirrors with a common focus on the sample rod and with halogen lamps in their other focus. By irradiation of the focused light the sample rod is locally heated and eventually molten. The molten zone can be moved up and down along the entire sample rod under simultaneous rotation. By repeated melting and crystallization of the sample seed selection takes place and the formerly polycrystalline rod is transformed into a single crystal. Single crystal growth can be performed with this furnace at maximum temperatures up to 2200°C in the pressure range from 10^{-5}mbar up to 10 bar and in oxidizing, reducing as well as inert atmosphere.

Figure 4: The four-mirror image furnace installed at the crystal laboratory of the WMI. Crystals can be grown by the floating zone and traveling solvent floating zone technique at temperatures up to 2200°C and pressures up to 10 bar.

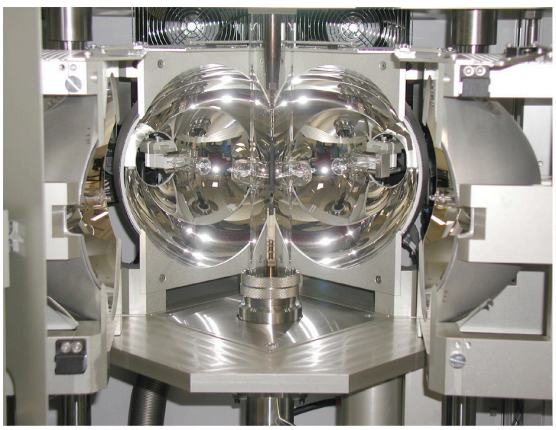

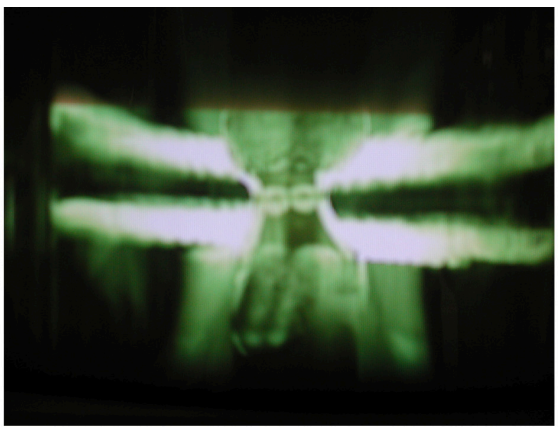

Figure 5: Left: Central part of the image furnace with the four elliptical mirrors. In the center one can see the quartz tube with the poly-crystalline rod. Right: View on the molten zone of TiO_2 (melting point: 1800°C) obtained by a CCD camera.

The X-ray diffraction systems

For x-ray analysis the Walther-Meissner-Institute operates two X-ray diffractometers (Bruker D8 Advance and D8 Discover). The two-circle system is used for powder diffraction. In this system the samples can be heated in oxygen atmosphere up to 1600°C. It is equipped with a Göbel mirror and an area detector to save measuring time. The second system is a high resolution four-circle diffractometer that can be used for reciprocal space mappings. It is equipped with a Göbel mirror and an asymmetric two-fold monochromator and allows for the texture analysis of thin film superlattices and single crystalline materials. In both systems measurements can be carried out fully computer controlled.

Figure 6: The two-circle X-ray diffractometer Bruker D8 Advance.

Beyond these two Bruker x-ray systems a Laue camera for single crystal analysis and a Debye-Scherrer camera are available.

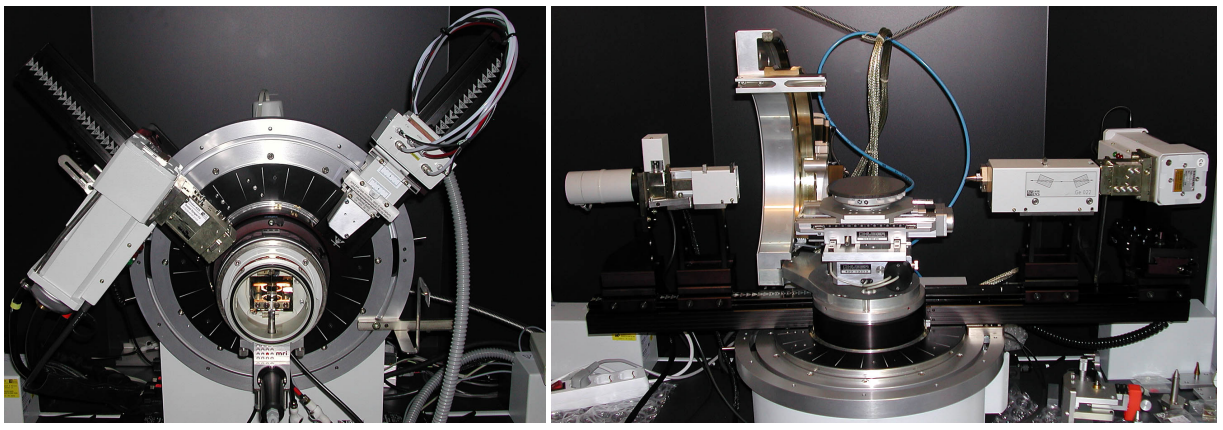

Figure 7: Left: High temperature sample holder of the D8 Advance system. Right: Four-circle high resolution X-ray diffractometer Bruker D8 Discover.

Figure 8: Quantum Design SQUID magnetometer.

The SQUID-magnetometer

For the analysis of the magnetic properties of materials, a Quantum Design SQUID magnetometer system as shown in Fig. 8 is used at the WMI. The SQUID magnetometer allows for measurements in the temperature regime from 1.5 to 400 K and provides excellent sensitivity particularly in the low field regime. Due to the excellent sensitivity of the system, thin film samples with a very small sample volume can be analyzed. In a special inset, samples can be measured up to temperatures well above room temperature (up to 700°C). For this option the sample volume has to be reduced. The SQUID magnetometer is equipped with a superconducting solenoid allowing for a maximum field of 7 T. At present, the magnetometer is used for the characterization of magnetic materials (both in bulk and thin film form). Examples are the doped manganites, magnetite, the double perovskites or magnetic semiconductors.

The High Field Laboratory

Transport and thermodynamic properties of samples are often studied as a function of applied magnetic field. For such measurements several superconducting magnets are available at the WMI. Two of them (8/10 and 15/17 Tesla magnet system) are located in the high magnetic field laboratory in the basement of the WMI. The magnet systems are lowered below the ground level to facilitate the access to the top flange and the change of the sample sticks. The magnet systems are decoupled from the building to avoid noise due to mechanical vibrations. A variety of sample holders can be mounted allowing for e.g. sample rotation during the measurement. For standard sample holders the accessible temperature regime is 1.5 K$< T <$ 300 K. However, also ^{3}He/^{4}He dilution refrigerator inserts ($T >$ 20 mK) or high temperature units ($T <$ 700 K) can be mounted. All measurements are fully computer controlled (by the use of the LabView software tool) allowing for remote control and almost continuous measurements.

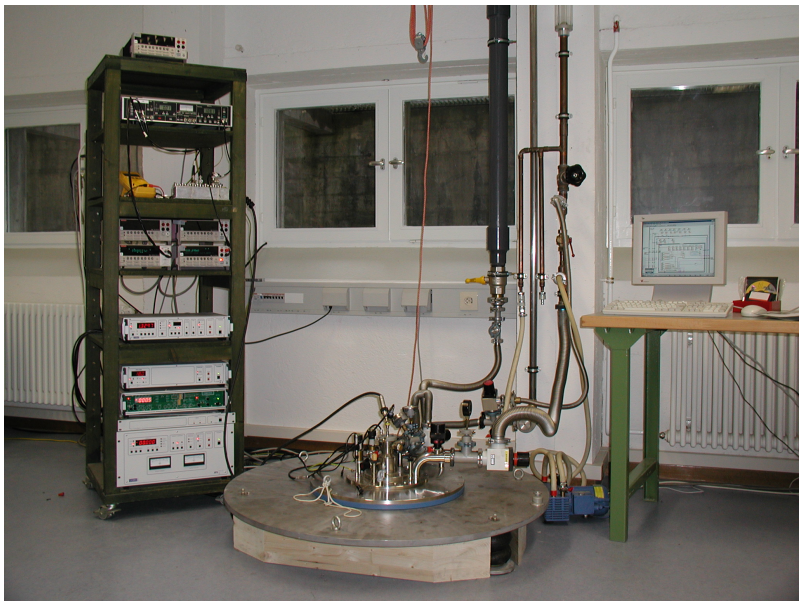

Figure 9: High field laboratory with Oxford 17 T magnet system.

Figure 10: Top: Part of the clean room facility with optical lithography equipment and clean room benches. Bottom: Resist coater and hot plates.

The Clean Room Facility

For the fabrication of nanostructures and superconducting as well as spintronic devices the WMI operates a class 1000 clean room facility with an area of about $50\,m^2$. This clean room facility has been put into operation at the WMI within the year 2001. The clean room is subdivided into two parts for optical lithography and electron beam lithography, respectively. The clean room facility is equipped with the standard tools for optical lithography such as resist coaters, hot plates, wet benches, a Karl Süss MJB3 mask aligner and an optical projection lithography system. The technical infrastructure for the clean room is located in the basement of the WMI directly below the clean room area.

Electron Beam Lithography

The Electron Beam Lithography System is installed in one part of the clean room facility. It consists of a Philips XL 30 SFEG scanning electron microscope (SEM) with a Raith Elphy Plus electron beam lithography system and a laser stage. The SEM is equipped with a hot field emitter and typically provides a beam diameter of less than 1.5 nm at $\geq$ 10 keV or about 2.5 nm at 1 keV. The lithography unit allows the fabrication of nanostructures down to about 10 nm. We have realized the controlled fabrication of metallic strip patterns with a strip width of about 20 nm. The electron beam lithography is used for the fabrication of nanostructures in metallic and oxide systems required for the study of quantum effects in mesoscopic samples.

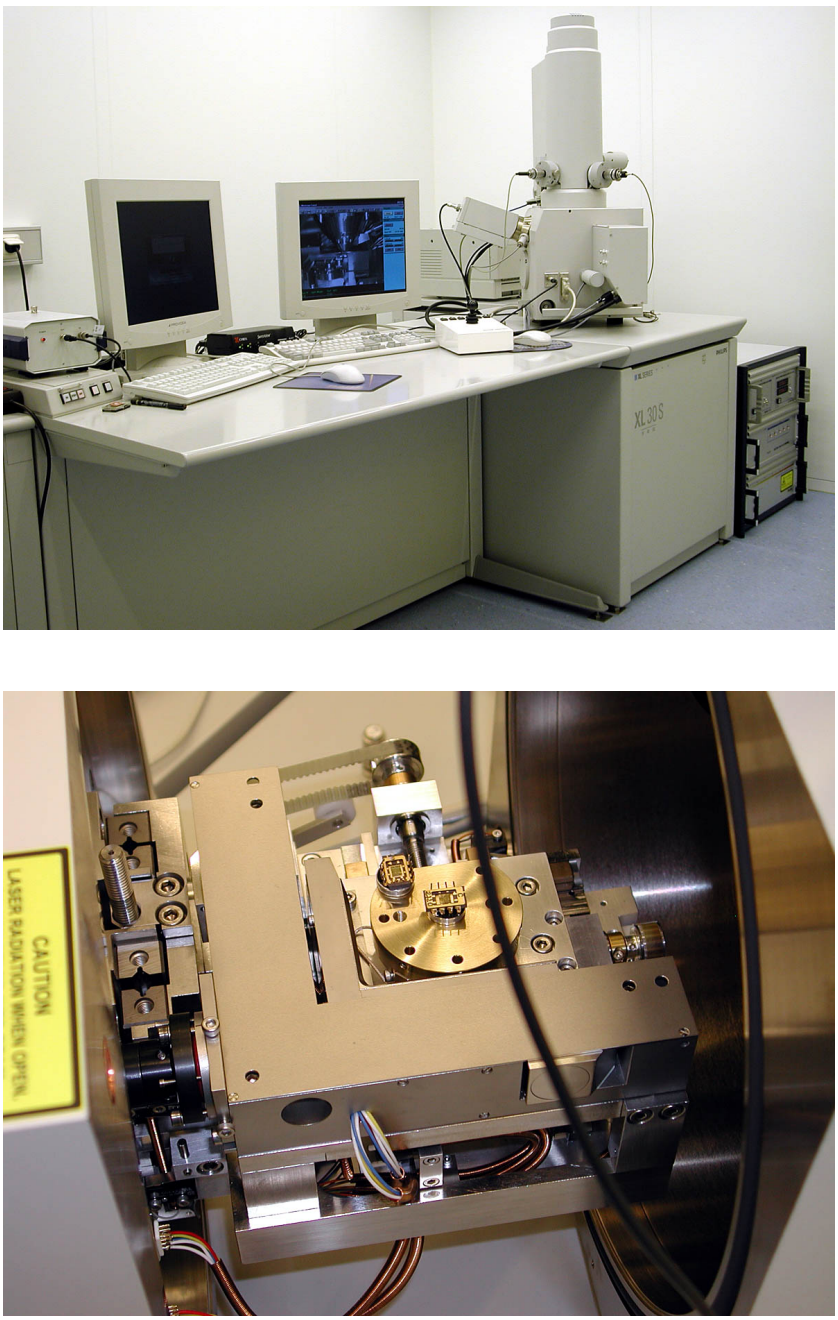

Figure 11: Top: Philips XL 30 SFEG Scanning Electron Microscope with Raith Elphy Plus Lithography System. Bottom: Raith Laser Stage.

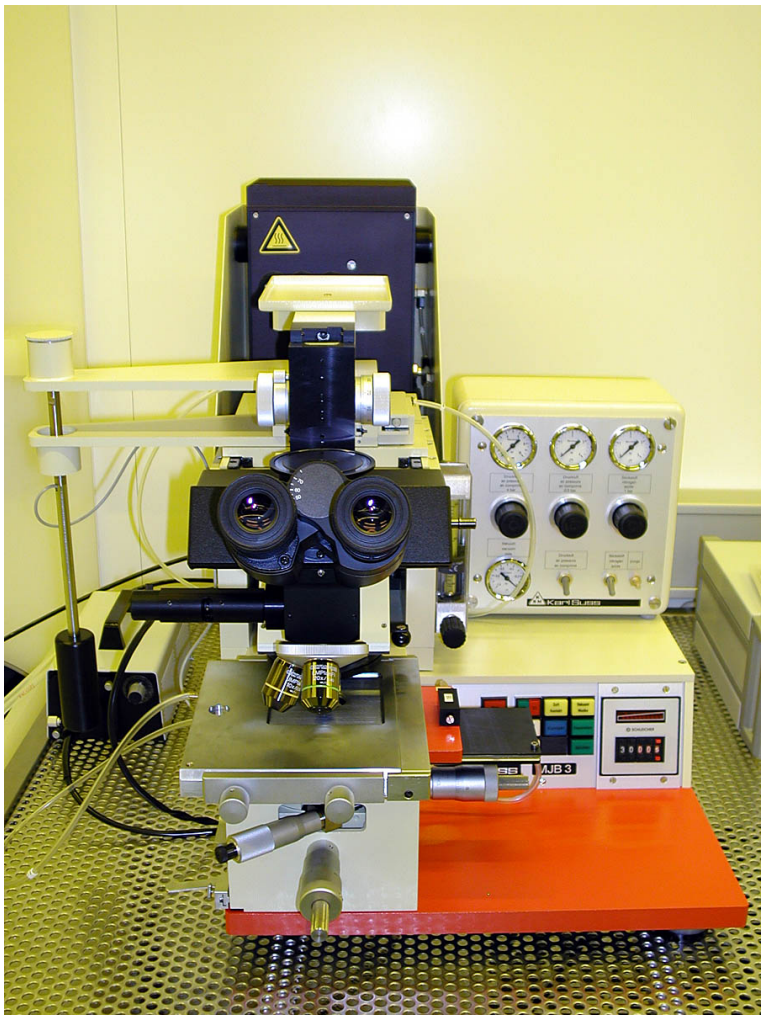

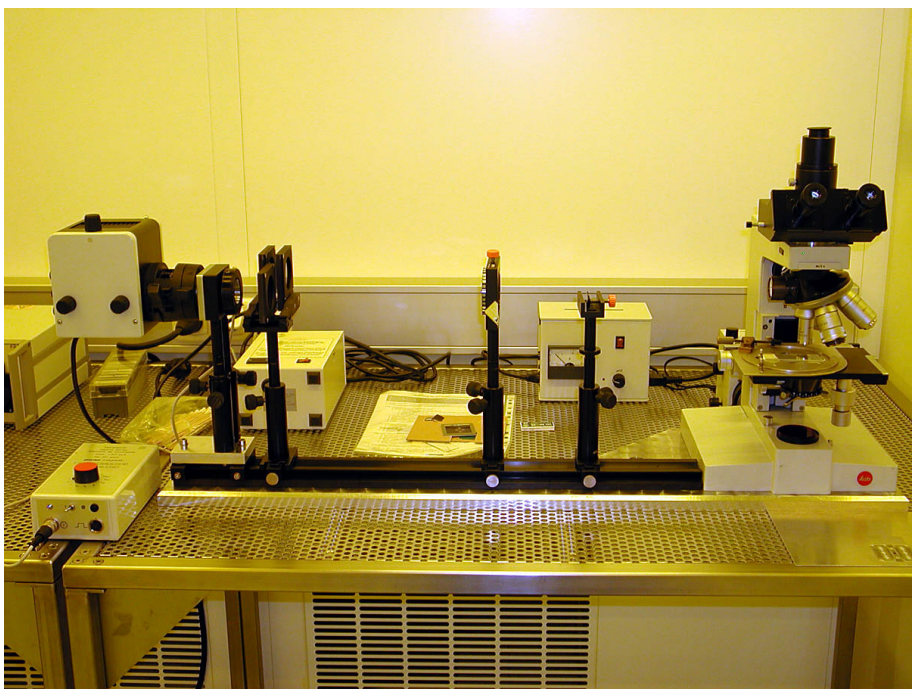

Figure 12: Top: Süss MJB 3 maskaligner for optical lithography. Bottom: Optical projection lithography based on an optical microscope.

Optical Lithography

For optical lithography a Karl Süss MJB 3 maskaligner or an optical microscope based projection system are used. The maskaligner is operating in the 1 : 1 soft or hard contact mode and is using chromium metal masks. In the projection system the mask pattern is demagnified by a factor of 5 to 100. Therefore, cheap foil masks can be used. With both systems microstructures with a lateral dimension down to 1 μm can be fabricated.

Low and Ultra-low Temperature Facilities

The Walther-Meissner-Institute operates several low and ultra-low temperature facilities that have been developed and fabricated in-house.

The lowest temperature is achieved by the nuclear demagnetization cryostat "Bayerische Millimühle 2". This ultra-low temperature facility consists of an in-house built dilution refrigerator and originally of two nuclear demagnetization stages. The first of those is based on a hyperfine enhanced van Vleck paramagnet $PrNi_5$ (0.9 mole), the second, which has been removed a few years ago, was based on purified copper (0.2 mole). The lowest temperature reached with this system was slightly below 30 μK in the copper nuclear spin system. At the moment, the first stage can be cooled to below 400 μK and, due to the large heat capacity of $PrNi_5$, it stays below the mixing chamber temperature (5 mK) for nearly 3 weeks. In this cryostat three measuring sites are provided, two in a magnetic field compensated region and one in the center of an 8 T magnet. They are suitable for specific heat measurements, for capacitive torque- and SQUID magnetometry, as well as for transport measurements (electrical und thermal conductivity). The cryostat is also equipped with a pressure cell for liquid and solid ^{3}He, which at the moment is used for nuclear spin resonance measurements below 1 mK.

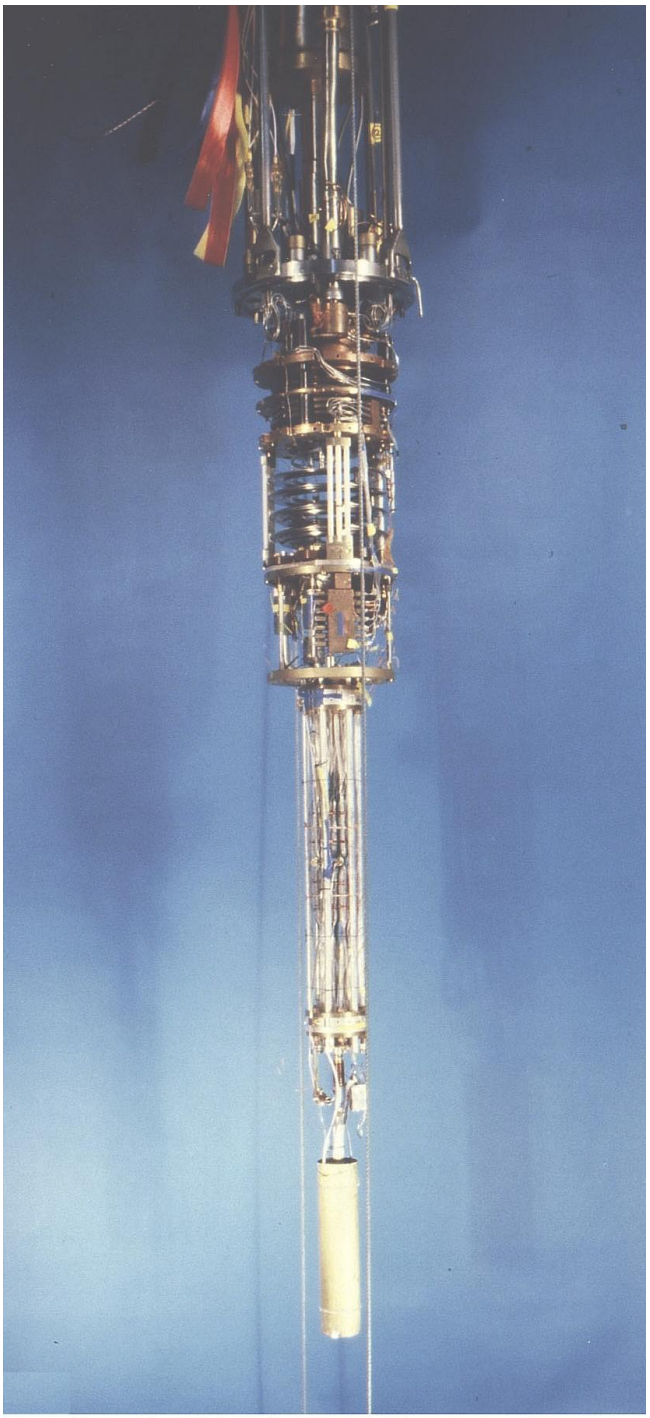

Figure 13: The dilution refrigerator and the nuclear demagnetization stage of the nuclear demagnetization cryostat "Bayerische Millimühle 2".

Figure 14: A "dry" millikelvin cooler: dilution refrigerator with pulse-tube pre-cooling.

Within the last years, the Walther-Meissner-Institute has developed a dilution refrigerator with pulse-tube pre-cooling. We denote such system as a "dry millikelvin cooler", since it does no longer require liquid helium for precooling. In contrast, this ultra-low temperature system is pre-cooled using a pulse tube refrigerator. The system is under test at the moment and temperature below 10 mK have already been achieved at the mixing chamber.

We note that the pulse-tube refrigerator based pre-cooling system also cannot only be used for providing the base temperature of a dilution refrigerator but also for various other cryogenic systems. The dry systems are highly attractive for locations where the supply with liquid helium is complicated and/or expensive. In future they even may displace standard liquid helium systems in low temperature laboratories.

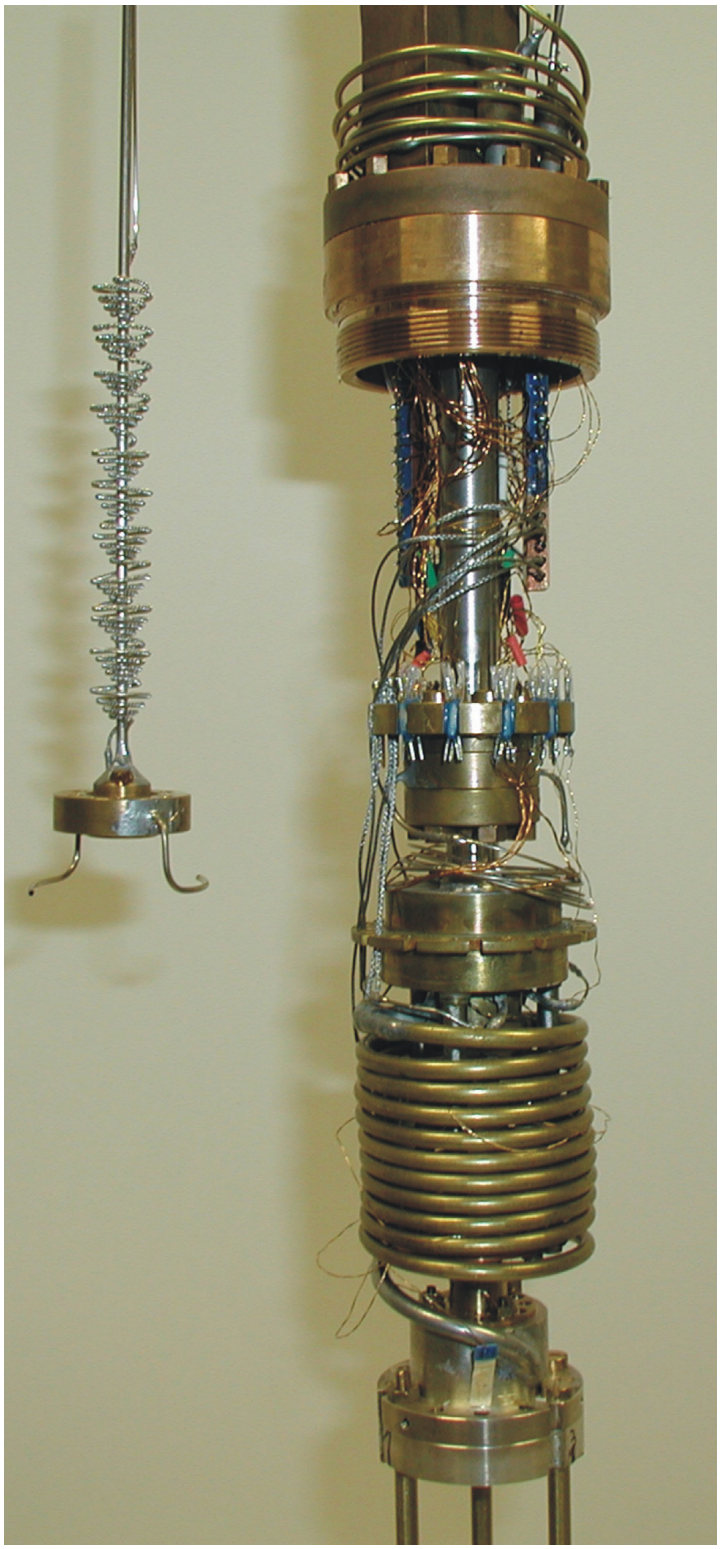

Figure 15: Dilution refrigerator insert with the Joule-Thompson stage, the heat exchanger and the mixing chamber.

The Walther-Meissner-Institute also develops and fabricates dilution refrigerator inserts for temperatures down to about 20 mK. The inserts fit into all cryogenic systems (e.g. superconducting magnets) having a two inch bore. They allow fast sample change and rapid cool down cycles of less than five hours.

The dilution refrigerator inserts are engineered and fabricated in-house and are also provided to other low temperature laboratories for ultra low temperature experiments.

New Network Infrastructure

The Walther-Meissner-Institute has a modern data network infrastructure. It was planned and installed in close cooperation with the Leibniz-Rechenzentrum and is based on fiber optic cables. About 270 double fiber optic lines with an average length of 50 m are installed in the WMI together with the corresponding number of data link sockets in all the labs and offices. In the basement of the institute, one room is hosting the central fiber optic network switch (see Fig. 16). There, the fibers coming from all rooms in the WMI meet together (Fig. 17, left). The switch provides the data link between the nodes within the WMI as well as from the WMI to the internet. The structured concept of the new network consisting of single node-to-node connections leads to higher reliability and efficiency for the data transfer as compared to the old coaxial ring lines (Fig. 17, right). With possible transfer rates up to 10 GBit/s per node the WMI fiber optic network is prepared for the coming generations of hardware and software.

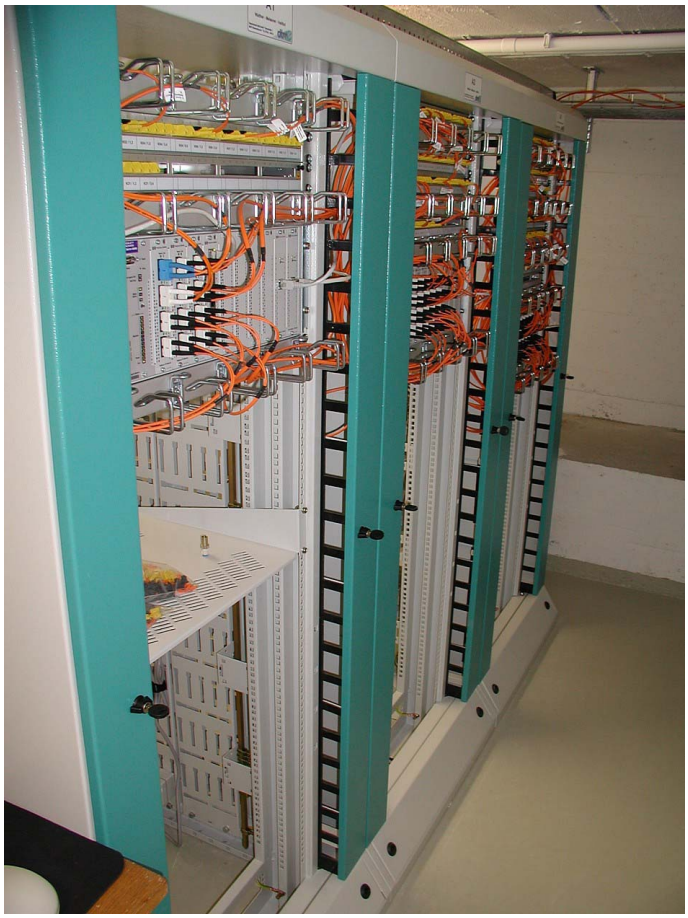

Figure 16: In the basement of the WMI a new stacked switch providing 68 fiber optic connectors was installed to switch data packets within the WMI as well as from the WMI to the internet and vice versa.

Figure 17: Left: 270 double optical fibers from all rooms of the WMI joining at the central switch. Right: The old coaxial cables after removal.

Publications

1. UHLIG K.,
   "Dry" dilution refrigerator with pulse-tube precooling
   Cryogenics **44**, 53-57 (2004).
2. GRIGORIEV P.D., WYDER P., KARTSOVNIK M.V., BIBERACHER W., KUSHCH N.D.,
   The interlayer magnetoresistance in quasi-2D layered organic metals
   I.D. Vagner et al. (eds.), Recent Trends in Theory of Physical Phenomena in High Magnetic Fields, 1-16 (2003).
3. LERF A.,
   Different modes and consequences of electron transfer in intercalation compounds
   J. of Physics and Chemistry of Solids **65**, 553-563 (2004).
4. BROWN S.P., CHARALAMBOUS D., JONES E.C., FORGAN E.M., KEALEY P.G., ERB A., KOHLBRECHER J.,
   Triangular to Square Flux Lattice Phase Transition in $YBa_2Cu_3O_7$
   Phys. Rev. Lett. **92**, 067004 (2004).
5. RIETSCHEL H., EINZEL D.,
   Hochtemperatur-Supraleiter
   Faszination Physik, Katja Bammel Hrsg. Elsevier Spektrum Akademischer Verlag (2004).
6. JIMÉNEZ DE HARO M.C., MARTÍNEZ BLANES J.M., POYATO J., PÉREZ-MAQUEDA L.A., LERF A., PÉREZ-RODRÍGUEZ J.L.,
   Effects of mechanical treatment and exchanged cation on the microporosity of vermiculite
   J. of Physics and Chemistry of Solids **65**, 435-439 (2004).
7. KARTSOVNIK M., ANDRES D., GRIGORIEV P., BIBERACHER W., MÜLLER H.,
   Interplay between the orbital quantization and Pauli effect in a charge-density-wave organic conductor
   Physica B **346-347**, 368-372 (2004).
8. SIMON J., WALTHER T., MADER W., KLEIN J., REISINGER D., ALFF L., GROSS R.,
   Diffusion and segregation effects in doped manganite/titanate heterostructures
   Appl. Phys. Lett. **84**, 3882-3884 (2004).
9. GOLOV A.I., EINZEL D., LAWES G., MATSUMOTO K., PARPIA J.M.,
   Dissipation Mechanisms near the Superfluid 3He Transition in Aerogel
   Phys. Rev. Lett. **92**, 195301 (2004).
10. RAMA N., PHILIPP J.B., OPEL M., CHANDRASEKARAN K., SANKARANARAYANAN V., GROSS R., RAO Ramachandra M.S.,
    Study of magnetic properties of $A_2B'NbO_6$ (A=Ba, Sr, BaSr and B′ = Fe, Mn) double perovskites
    J. Appl. Phys. **95**, 7528 (2004).
11. BIBERACHER W., CHRIST P., KARTSOVNIK M.V., ANDRES D., MÜLLER H., KUSHCH N.,
    Anisotropic susceptibility of α-(BEDT-TTF)$_2$KHg(SCN)$_4$
    J. Phys. IV France **114**, 291-292 (2004).
12. GOENNENWEIN S.T.B., WASSNER T.A., HÜBL H., BRANDT M.S., PHILIPP J.B., OPEL M., GROSS R., KÖDER A., SCHOCH W., WAAG A.,
    Hydrogen control of ferromagnetism in a dilute magnetic semiconductor
    Phys. Rev. Lett. **92**, 227202 (2004).
13. RAMA N., PHILIPP J.B., OPEL M., ERB A., SANKARANARAYANAN V., GROSS R., RAO Ramachandra M.S.,
    Effect of rare earth ion substitution on the magnetic and transport properties of $Pr_{0.7}RE_{0.04}Sr_{0.26}MnO_3$ (RE = Er, Tb and Ho)
    Eur. Phys. J. **B 38**, 553-557 (2004).
14. KARTSOVNIK M.V., ANDRES D., BIBERACHER W., GRIGORIEV P.D., SCHUBERTH E.A., MÜLLER H.,
    New electronic phase transitions in α-(BEDT-TTF)$_2$KHg(SCN)$_4$
    J. Phys. IV France **114**, 191-197 (2004).
15. LERF A., CAPKOVÁ P.,
    Dye/Inorganic Nanocomposites
    Encyclopedia of Nanoscience and Nanotechnology Ed. by H.S. Nalwa **2**, 639-693 (2004).

16. KARGL V., MIRMELSTEIN A., BÖNI P., SHEPTYAKOV D., AMATO A., KAZAKOV S., KARPINSKI J., ERB A.,
Neutron diffraction, specific heat and SR study of the spin-chain compounds $Ca^{2+}Y^{2-}Cu_5O_{10}$
Physica B **350**, 257-259 (2004).
17. EINZEL D., MANSKE D.,
Electronic Raman response in anisotropic metals
Phys. Rev. B **70**, 172507 (2004).
18. NOTHARDT A., BALTHES E., SCHMIDT W., SCHWEITZER D., KARTSOVNIK M.V., SHEIKIN, I.,
SdH experiments on the organic superconductor κ-(BEDT-TTF)$_2$I$_3$ under hydrostatic pressure
J. Phys. IV France **114**, 351-353 (2004).
19. KARTSOVNIK M.V.,
High magnetic fields: a tool for studying electronic properties of layered organic metals
Chem. Rev. **104**, 5737-5781 (2004).
20. PÉREZ-RODRIGUEZ J.L., POYATO J., JIMÉNEZ DE HARO M.C., PÉREZ-MAQUEDA L.A.,
Thermal decomposition of ammonium vermiculite from Santa Olalla and its relation to the metal ion distribution in the octahedral layer
Phys. Chem. Mater. **31**, 415-420 (2004).
21. FISCHER F., GRAYSON M., SCHUBERTH E.A., SCHUH D., BICHLER M., ABSTREITER G.,
New Anisotropic Behavior of Quantum Hall Resistance in (110) GaAs Heterostructures at mK Temperatures and Fractional Filling Factors
Physica E **22**, 108 (2004).
22. SCHUBERTH E.A., MILLAN-CHACARTEGUI C., SCHÖTTL S.,
Pulsed NMR in the Nuclear Spin Ordered Phases of Solid ^{3}He in a Silver Sinter
J. Low Temp. Phys. **134**, 637 (2004).
23. REISINGER D., MAJEWSKI P., OPEL M., ALFF L., GROSS R.,
Hall effect, magnetization and conductivity of Fe_3O_4 epitaxial thin films
Appl. Phys. Lett. **85**, 4980 (2004).
24. GÖNNENWEIN S.T.B., WASSNER T.A., HÜBL H., KÖDER A., SCHOCH W., WANG A., PHILIPP J.B., OPEL M., GROSS R., STUTZMANN M., BRANDT M.S.,
Hydrogen and magnetism in $Ga_{1-x}Mn_xAs$
Adv. in Solid State Phys. 44, 453 – 465 (2004).
25. PHILIPP J.B., MAJEWSKI P., REISINGER D., GEPRÄGS S., OPEL M., ERB A., ALFF L., GROSS R.,
Magnetoresistance and magnetic properties of the double perovskites
Acta Physica Polonica **A 105**, 7 (2004).
26. GÖNNENWEIN S.T.B., HÜBL H., STUTZMANN M., BRANDT M.S., PHILIPP J.B., OPEL M., GROSS R., KÖDER A., SCHOCH W., WAAG A.,
Spin wave resonance investigation of the macroscopic magnetic properties of the ferromagnetic semiconductor $Ga_{1-x}Mn_xAs$
Phys. Rev. **B**, submitted for publication (12/2003).
27. RAMA N., RAO M.S. Ramachandra, SANKARANARAYANAN V., OPEL M., GROSS R.,
A-site disorder dependent percolative transport and Griffith phase in doped manganites
Phys. Rev. **B**, accepted for publication, (10/2004).
28. MAJEWSKI P., GEPRÄGS S. BOGER A., OPEL M., ALFF L., GROSS R.,
Epitaxial growth of electron doped double perovskites $La_xA_{2-x}CrWO_6$ with $A =$ Sr and Ca
J. Magn. Magn. Mat., accepted (07/2004).
29. DIACONU M., SCHMIDT H., HOCHMUTH H., LORENZ M., BENNDORF G., LENZNER J., SPEMANN D., SETZER A., ESQUINAZI P., PÖPPL A., von WECKSTERN H., NIELSEN K.-W., GROSS R., SCHMID H., MADER W., GRUNDMANN M.,
Room-temperature ferromagnetic Mn-doped ZnO-films obtained by pulsed laser deposition
Phys. Rev. **B**, submitted for publication (10/2004).
30. SCHUBERTH E.A., KATH M., TASSINI L., MILLAN-CHARCARTEGUI C.,
Magnetization Studies of the Nuclear Spin Ordered Phases of Solid ^{3}He in Silver Sinters
Europ. Phys. Journ., submitted for publication (2004).
31. SAFAROWSKY C., MERZ L., RANG A., BROEKMANN P., HERMANN B.A., SCHALLEY C.A.,

Template zweiter Ordnung: geordnete Schichten aus supramolekularen Quadraten auf einer Chlorid-bedeckten Cu(100)-OberflÃd′che
Angewandte Chemie 1311-1314, 116 (2004).

32. CONSTABLE C., HERMANN B.A., HOUSECROFT C., MERZ L., SCHERER L.,
Monitoring conformational diversity in self-organised monolayers with scanning tunnelling microscopy at near atomic resolution
Chemical Communication 928-929, (2004).
33. NIELSEN K.-W., PHILIPP J.B., OPEL M., ERB A., SIMON J., ALFF L., GROSS R.,
Ferromagnetism in Mn-doped ZnO due to impurity bands
Superlattices and Microstructures, accepted for publication (10/2004).
34. REISINGER D., QURESHI S., MAJEWSKI P., ALFF L., OPEL M., GROSS R.,
Room temperature magnetoresistance in magnetite based tunnel junctions: Influence of tunneling barrier
J. Appl. Phys., submitted for publication (2004).

Theses, Appointments, Awards

Appointments

Priv.-Doz. Dr. habil. Lambert Alff has been appointed full professor at the Institute of Sensor and Actuator Systems of the Technical University of Vienna, Austria.

Completed and ongoing Ph.D. Theses

1. **Magnetit in ultradünnen, epitaktischen Schichtsystemen für die Spinelektronik**
   Daniel Reisinger, 03. 05. 2004.
2. **Grenzflächeneffekte zwischen Hochtemperatur-Supraleitern und Normalleitern**
   Mitja Schonecke, 12. 05. 2004.
3. **Spinabhängiger Transport und Quanteninterferenzeffekte in mesoskopischen metallischen Systemen**
   Jürgen Schuler, seit Dezember 1998.
4. **Symmetrie des Ordnungsparameters und Pseudogap-Verhalten in Hochtemperatur-Supraleitern**
   Bettina Welter, seit August 2000.
5. **Elektronische und magnetische Eigenschaften von organischen Metallen und Supraleitern**
   Dieter Andres, seit September 2000.
6. **Herstellung und Charakterisierung von supraleitenden Quantenbits**
   Frank Deppe, seit April 2002.
7. **Spininjektion in Halbleiter mit ferromagnetischen Oxiden**
   Petra Majewski, seit November 2002.
8. **Raman scattering in materials with quantum phase transitions**
   Leonardo Tassini, seit April 2003.
9. **Supraleitende Quantenbits mit π-Josephson-Kontakten für die Quanteninformationsverarbeitung**
   Matteo Mariantoni, seit November 2003.
10. **Wachstum und Physik künstlicher magnetischer Heterostrukturen**
    Karl Nielsen, seit Dezember 2003.
11. **Magnetisierungsmessungen an festem ^{3}He bei ultratiefen Temperaturen**
    Matthias Kath, seit April 2004.
12. **Supraleitende Quantenbits mit -Josephson-Kontakten**
    Georg Wild, seit September 2004.
13. **Kristallzüchtung und Charakterisierung von elektronendotierten Hochtemperatur-Supraleitern**
    Michael Lambacher, seit September 2004.
14. **Spin-Engineering in funktionalen Schichtsystemen aus Übergangsmetalloxiden**
    Stephan Geprägs, seit Oktober 2004.
15. **Herstellung und Charakterisierung von supraleitenden Nanostrukturen für die Realisierung von Quantenbits**
    Tobias Heimbeck, seit November 2004.
16. **Raman-Spektroskopie an Kupratsupraleitern**
    Wolfgang Prestel, seit November 2004.
17. **Scanning Tunnelling Microscope (STM) Investigation of Self-Organizing (Magnetic) Molecules on Surfaces**
    Michaela Entfellner, since October 2004.

Completed and ongoing Diploma, Bachelor, Master Theses

1. **Thermodynamische Untersuchung einer tankinternen Hochdruckpumpe für Flüssigwasserstoff**
   Florian Kuhn, Februar 2004.
2. **Magnetisierungsmessungen an festem ^{3}He bei ultratiefen Temperaturen**
   Matthias Kath, März 2004.
3. **Bestimmung der effektiven Spinpolarisation von $La_{2/3}Ba_{1/3}MnO_3$**
   Stephanie Wagner, Juni 2004.
4. **Elektronendotierung und strukturelle Effekte in ferromagnetischen Doppelperowskiten**
   Stephan Geprägs, Juli 2004.
5. **Macroscopic Quantum Tunneling in Josephson Junctions – a Method to Characterize a Well-shielded Low Temperature Setup**
   Georg Wild, Juli 2004.
6. **Herstellung und Charakterisierung von supraleitenden Phasen-Qubits**
   Heribert Knoglinger, August 2004.
7. **Magnetic Tunnel Junctions Based on Fe_3O_4**
   Suleman K. Qureshi, September 2004:
8. **Control Allocation**
   Ingmar Mayerbuch, Oktober 2004.
9. **Tunnelspektroskopie an elektrondotierten Hochtemperatur-Supraleitern**
   Andreas Winkler, Dezember 2004.
10. **Magnetische Tunnelkontakte mit Sr_2CrWO_6**
    Andrea Boger, Dezember 2004.
11. **Untersuchung der Zustandsquantisierung in Josephson-Kontakten**
    Karl Madek, seit Dezember 2003.
12. **Nachweis von Kupfer in Silizium mit der Transient Ion Drift (TID) Methode**
    Robert Christopher Burns, seit April 2004.
13. **Ferromagnetische II-IV-Halbleiter**
    Maike Lübbe, seit 31. 08. 2004.
14. **Epitaxiale Verspannungseffekte in ferromagnetischen Doppelperowskiten**
    Robert Geißler, seit 31. 08. 2004.
15. **Magnetische Tunnelkontakte auf der Basis epitaktischer Magnetit-Schichten**
    Edwin Menzel, seit November 2004.
16. **Einfluss des Cr/W Verhältnisses auf die Curie-Temperatur von Sr_2CrWO_6**
    Oliver Sanganas, seit November 2004.
17. **Parameterisiertes Simulationsmodell des Wärmeeintrages am Flüssigwasserstofftank**
    Sascha Gasser, seit November 2004.
18. **Charakterisierung von supraleitenden Fluss-Qubits**
    Renke Stolle, seit Dezember 2004.
19. **Herstellung von π-Josephson-Kontakten mit Supraleiter/Ferromagnet/Supraleiter Schichtsystemen**
    Bernhard Huber, seit Dezember 2004.
20. **Annealing and Characterization of High-T_c Single Crystals**
    Manwan Abbas, seit Dezember 2004.
21. **Circuit Quantum Electrodynamics with Superconducting Flux Qubits**
    Andreas Emmert, seit Dezember 2004.

Research Projects and Cooperations

Many of our research projects have benefited from the collaboration with external groups via joint research projects, individual collaborations, exchange programs and visitors. Several collaborations are based on joint projects which are financially supported by different organizations (see list below). A large number of collaborations also exists with several universities and other research institutions without direct financial support. These are also listed below.

Funded Projects

Deutsche Forschungsgemeinschaft: Sonderforschungsbereiche

Sonderforschungsbereich 631: Festkörperbasierte Quanteninformationsverarbeitung: Physikalische Konzepte und Materialaspekte

1. Teilprojekt A3/A4: Supraleitende Bauelemente mit π-Kontakten als Grundelemente für Quanteninformationssysteme
   Gross, Alff, Marx
2. Teilprojekt C5: Spinabhängiger Transport in nanostrukturierten Festkörpern
   Marx, Gross, Opel
3. Teilprojekt S: Verwaltung des Sonderforschungsbereichs
   Gross

Deutsche Forschungsgemeinschaft: Forschergruppen

Forschergruppe 538: Dotierungsabhängigkeit von Phasenübergängen und Ordnungsphänomenen in Kupratsupraleitern

1. Teilprojekt: Einkristallzüchtung von p- und n-dotierten Kupratsupraleitern
   A. Erb, R. Gross
2. Teilprojekt: Raman-Untersuchungen zu konkurrierenden Ordnungsphänomennen in Kupraten
   R. Hackl, R. Gross
3. Sprecherprojekt
   R. Hackl

Deutsche Forschungsgemeinschaft – Normalverfahren

1. Heteroepitaxie von Übergangsmetalloxiden
   (L. Alff und R. Gross, Az. Al 560/1-1+2)

2. Kristalline organische Metalle und Supraleiter: Synthese und elektronische Eigenschaften,
   gefördert von der DFG und der russischen Stiftung für Grundlagenforschung (RFFI)
   (W. Biberacher, WMI, und N. Kushch, Institut für Probleme der chemischen Physik, Cernogolovka, Az.: 436 RUS 113/592/0)

3. Untersuchung des Wechselwirkungspotentials in Kuprat–Supraleitern durch Vergleich verschiedener spektroskopischer Methoden
   (R. Hackl, Az. HA 2071/2-1+2)

4. Neue funktionale Schichtsysteme auf der Basis künstlicher heteroepitaktischer Mehrlagenstrukturen aus Übergangsmetalloxiden
   im Rahmen des Schwerpunktprogramms 1157 *Integrierte elektrokeramische Funktionsstrukturen*
   (R. Gross, Az. GR 1132/13-1)

5. Entwicklung eines hochgenauen Rotatiossensors mit superfluidem ^{3}He als Arbeitsmedium
   (E. Schuberth, Az. Schu 450/4-1+2)

Bundesminister für Bildung, Wissenschaft, Forschung und Technologie (BMBF)

1. Wissenschaftlich–Technologische Zusammenarbeit mit Indien: Ferromagnetische Oxide mit hoher Spinpolarisation
   (R. Gross, Projektkennzeichen: IND 01/009)
   Partner: Prof. Dr. M. S. R. Rao, Indian Institute of Technology, Madras, India.

2. Verbundprojekt: Spinelektronik und Spinoptoelektronik in Halbleitern
   Teilprojekt: Ferromagnetische metallische Oxide mit hoher Spinpolarisation für die Spinelektronik
   (R. Gross, Förderkennzeichen: 13N8279)
   Partners: Universities of Würzburg, Hamburg, Regensburg, Hannover and Marburg, Max–Planck–Institute Halle, Siemens AG, Infineon Technologies, Aixtron GmbH.

3. Wissenschaftlich–Technologische Zusammenarbeit mit Ungarn: Transporteigenschaften hochkorrelierter Schichtsysteme
   (R. Hackl, Projektkennzeichen: HUN 01/008)
   Partner: Ungarische Akademie der Wissenschaften, Institut für Festkörperphysik und Optik, Prof. Dr. Istvan Tüttö.

European Union

1. European Science Foundation Network *"Thin Films for Novel Oxide Devices: THIOX"*
   (R. Gross; coordination: Prof. D. Blank, University of Twente, The Netherlands)
   partners: several European Universities and research facilities.

2. Research and Training of Young Researchers on the Magnetic Properties of ^{3}He by Means of Neutron Diffraction
   (E. Schuberth; coordination: Dr. Konrad Siemensmeyer, Hahn–Meitner Institute Berlin GmbH)
   European Community, Contract No.: HPRN-CT-2000-00166

Partners: Hahn–Meitner Institut, Berlin, Univ. of Florida, Royal Holloway College, London, Univ. Liverpool, CNRS, Grenoble and Univ. Paris, Saclay.

3. High Field Infrastructure Cooperative Network
(W. Biberacher, coordination by CNRS Grenoble, contract No.: HPRI-CT-1999-40013)
Partners: in total 31 participants.

Deutscher Akademischer Austauschdienst (DAAD)

1. Projektbezogener Personenaustausch mit Spanien, Aciones Integradas Hispano–Alemanas
(A. Lerf)
Centro de Investigaciones Cientificas "Isla de Cartuja", Universidad de Sevilla, Prof. Dr. Jose Luis Perez Rodriguez

Alexander von Humboldt Stiftung

1. Humboldt Forschungsstipendium "Devereaux"
(R. Hackl, Förderkennzeichen IV-USA/109800 6 STP)

INTAS

1. *Magnetic quantum oscillations in layered organic superconductors*
(W. Biberacher, M. Kartsovnik, Förderkennzeichen INTAS 01-0791)

NATO

1. NATO Advanced Research Workshop on Nanoscale Devices – Fundamentals and Applications
(R. Gross, Reference No.: PST.EAP.ARW 980607).

IDK-NBT

1. STM on magnetic layers and self-organized magnetic molecules
(B. Hermann, head: C. Bräuchle, J. Rädler, IDK-NBT 1506-42501-1).

Research Equipment financed via HBFG

1. Helium Liquefaction System, Linde TCF 20
(R. Gross, reference No.: HBFG-163-957)

2. Reactive Ion Etching System
(R. Gross, reference No.: HBFG-163-1009)

3. Low Temperature Scanning Tunneling Microscope with UHV Preparation Chamber
(B. Hermann, reference No.: HBFG-5882/03)

Conferences and Workshops

The Walther-Meißner-Institute has organized/co-organized the following conferences and workshops in 2004:

1. **International Workshop on Fluctuating Charge Order in HTSC**
   May 27-28, 2004, Walther-Meißner-Institute, Garching, Germany

2. **International Workshop on Solid State Based Quantum Information (QIP 2004)**
   September 13 - 17, 2004, Herrsching, Germany.

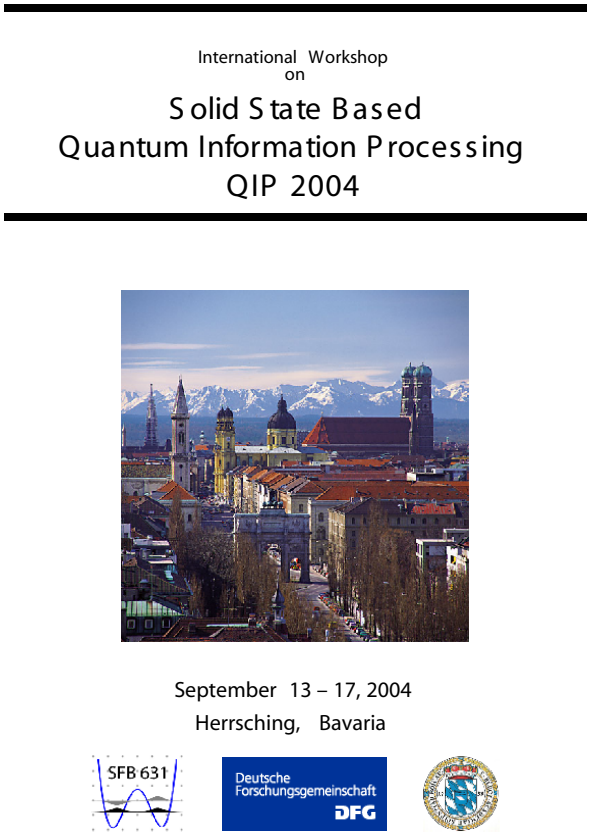

3. **NATO Advanced Research Workshop on Nanoscale Devices - Fundamentals and Applications (NDFA-2004)**
   September 18 – 22, 2004, Kishinev, Moldova.

4. **International Workshop on Ordering Phenomena in Cuprate Superconductors**
   November 4 – 5, 2004, Munich Residence, Munich, Germany.

Collaborations

Other collaborations without direct project funding involve:

- NTT, Japan (Prof. Dr. H. Takayanagi, Dr. M. Naito)
- Tokyo Institute of Technology, Japan (Prof. K. Koinuma)
- Universitá di Roma "La Sapienza", Roma, Italy (Prof. Dr. Paolo Calvani, Prof. C. Di Castro)
- Materials Physics Laboratory, Helsinki University of Technology (Dr. Tero Heikkilä)
- Department of Condensed Matter Physics, The Weizmann Institute of Science, Israel (Dr. Moshe Schechter)
- Instituto de Ciencia de Materiales de Sevilla (Prof. J. Poyato, Prof. J.L. Perez-Rodriguez)
- Chalmers University of Technology, Gothenburg, Sweden (Prof. Dr. P. Delsing)
- Hungarian Academy of Sciences, Budapest University of Technology and Economics Budapest, Hungary (Prof. Dr. K. Kamaras, Dr. Attila Virosztek, Prof. Dr. A. Zawadowski)
- Hungarian Academy of Science, Eötvös Lorand University, Budapest, Hungary (Dr. I. Tüttö)
- University of Waterloo, Department of Physics, Ontario, Canada (Prof. Dr. T.P. Devereaux)
- University of Basel, Institute of Inorganic Chemistry, Switzerland (Prof. E. Constable, Prof. C. Housecroft)
- University of Szeged (Prof. I. Dekany)
- CSIC Oviedo (Prof. J. Tascon)
- Royal Holloway University, London (Prof. J. Saunders)
- University of Liverpool (Dr. J. Goff)
- CNRS Grenoble (Prof. H. Godfrin)
- University of Florida (Prof. D. Adams, Prof. Y. Takano)
- Institute of Problems of Chemical Physics, Chernogolovka (Dr. N. Kushch, Dr. S. Pesotskii, S. Simonov)
- National Pulsed Magnetic Field Facility, Toulouse, France (Dr. E. Haanappel)
- Materials Science Research Centre, Indian Institute of Technology, Madras, Indien (Prof. M.S. Ramachandra Rao)
- Cryomech, Inc. N.Y. (Dr. Ch. Wang)
- Vericold Technologies, Ismaning (Dr. J. Höhne, Dr. M. Bühler)
- University of Bonn (Prof. W. Mader)
- University of Leipzig, Germany (Dr. H. Schmidt)
- Hahn-Meitner-Institut, Berlin (Dr. A. Buchsteiner, Dr. J. Pieper, Dr. K. Siemensmeyer)
- IFW Dresden (Prof. B. Büchner, Prof. J. Fink, Dr. S. V. Borisenko, Dr. M. Knupfer)
- Ludwig–Maximilians–University Munich, Germany (Prof. Kotthaus, Prof. von Delft, Dr. F. Wilhelm)
- University of Tübingen, Germany (Prof. R. Kleiner, Prof. D. Kölle)
- University of Würzburg, Germany (Prof. W. Hanke, Prof. L. Molenkamp)
- University of Augsburg, Germany (Prof. Dr. P. Hänggi)
- Walter-Schottky-Institut, Garching (Prof. G. Abstreiter, Dr. M. Brandt)
- Ludwig-Maximilians-University Munich, Germany (Prof. von Delft, Dr. R. Dahlke)

- University of Hamburg (Dr. D. Grundler, Dr. G. Meier)
- University of Bayreuth (Prof. J. Breu)
- Neutronenquelle FRM 2, Garching (Dr. Ch. Schanzer)
- Lehrstuhl f. Anorganische Chemie, TU München (Prof. T. Fässler)
- Institut für Experimentelle Physik, Slowakische Akademie der Wissenschaften, Kosice (Prof. K. Flachbart)
- Northwestern University Evanston, Illinois
- Institute of Solid State Physics, Chernogolovka, Russia (Dr. R.P. Shibaeva, Prof. Dr. V. Ryazanov, Prof. Dr. Lev Vinnikov)
- High–Magnetic–Field Laboratory, Grenoble, France (Dr. I. Sheikin)
- B. Verkin Institute for Low Temperature Research and Engineering, Kharkov, Ukraine (Prof. V.G. Peschansky)
- Landau Institute for Theoretical Physics, Chernogolovka, Russia (Dr. P. Grigoriev)

Stays abroad

Extended visits of members of the Walther-Meissner-Institute at foreign research laboratories:

1. **Mark Kartsovnik, Werner Biberacher**
   High Magnetic Field Laboratory, Grenoble, France
   25. 01. – 02. 02. 2004
2. **Mark Kartsovnik, Werner Biberacher**
   High Magnetic Field Laboratory, Grenoble, France
   04. 04. – 12. 04. 2004
3. **Mark Kartsovnik, Dieter Andres**
   High Magnetic Field Laboratory, Grenoble, France
   20. 11. – 29. 11. 2004
4. **Werner Biberacher**
   National Pulsed Magnetic Field Facility, Toulouse, France
   03. 05. – 08. 05. 2004
5. **Anton Lerf**
   Instituto de Ciencia de Materiales de Sevilla, Spain
   17. 04. – 24. 04. 2004
6. **Erwin Schuberth**
   National Physics Laboratory, Richmond, UK
   26. 08. – 28. 08. 2004
7. **Erwin Schuberth**
   Royal Holloway University, London
   29. 08. – 31. 08. 2004
8. **Rudolf Hackl**
   Università di Roma La Sapienza, Istituto Nazionale di Fisica della Materia (Prof. Paolo Calvani and Prof. Carlo Di Castro) Rom, Italien
   06. - 10. 01. 2004
9. **Rudolf Hackl**
   Technical University of Budapest and Research Institute for Solid State Physics (Profs. I. Tüttö, A. Virosztek, A. Zawadowski), Budapest, Ungarn
   22. 06. – 25. 06. 2004
10. **Bianca Hermann**
    University of Basel, Institute of Physics (Prof. H.-J. Güntherodt) Basel, Switzerland
    09. - 12. 01. 2004 and 17. - 20. 09. 2004
11. **Bianca Hermann**
    University of Basel, Institute of Physics and Institute of Inorganic Chemistry (Prof. H.-J. Güntherodt and Prof. E. Constable) Basel, Switzerland
    09. - 11. 02. 2004, 28. 02. - 03. 03. 2004, 0.2. - 03. 05. 2004, 16. - 17. 05. 2004, 06. -07. 06. 2004, 04. -05. 07. 2004, and 28. - 29. 07. 2004

Conference Talks and Seminar Lectures

Lambert Alff

1. **Grenzflächen in oxidischen Materialien: Von Josephson-Kontakten mit Hochtemperatur-Supraleitern zu Tunnelmagnetowiderstandsbauelementen**
   07. 01. 2004
   Physikalisches Institut, Universität Würzburg
2. **Hidden pseudogap in electron doped high-temperature superconductors**
   11. – 16. 01. 2004
   Workshop on Unconventinal Superconductivity, University of Maimi
3. **Hidden pseudogap in electron doped high-temperature superconductors**
   22. – 26. 03. 2004
   APS-March Meeting, Montreal, Canada
4. **Novel considerations about the phase diagram of electron doped high-temperature superconductors**
   21. 04. 2004
   Max-Planck-Institut für Festkörperphysik, Stuttgart
5. **Novel considerations about the phase diagram of electron doped high-temperature superconductors**
   27. 05. 2004
   Laboratoire de Physique Quantique, ESPCI (Ecole Supérieure de Physique et de Chimie Industrielles, CNRS (Centre National de la Recherche Scientifique, Paris
6. **Phase diagram of the electron doped cuprates**
   14. – 15. 06. 2004
   Workshop on New Superconductors, Berlin
7. **Pulsed Laser Deposition**
   8. – 9. 07. 2004
   Technology Days, TUI-Laser, München
8. **Novel considerations about the phase diagram of electron doped high-temperature superconductors**
   14. – 15. 10. 2004
   2. International Workshop on Electronic and Magnetic Properties in Novel Superconductors (INTAS), Freie Universität Berlin

Dietrich Einzel

1. **Viscous Transport in Dirty Fermi Superfluids**
   09. 03. 2004
   AKF-Frühjahrstagung, Regensburg
2. **Viscous Transport in Dirty Fermi Superfluids**
   07. 06. 2004
   Seminar über neuere Arbeiten der Physik, Universität Marburg
3. **Analytische Zweiflüssigkeitsbeschreibung von paarkorrelierten Fermisystemen**
   16. 06. 2004
   Theoretisch-Physikalisches Kolloquium, TUM Garching
4. **Quantenflüssigkeiten I**
   30. 11. 2004
   Seminar über Makroskopische Quantensysteme, WMI Garching
5. **Quantenflüssigkeiten II**
   07. 12. 2004
   Seminar über Makroskopische Quantensysteme, WMI Garching

6. **Analytic Two-Fluid Description of Pair-Correlated Fermi Systems**
   15. 12. 2004
   Seminar über Aktuelle Fragen der Festkörperphysik, MPI Stuttgart

Andreas Erb

1. **Oxygen in High Temperature Superconductors: Oxygen Diffusion and Oxygen Microstructure probed by Transport and Magnetic Measurements**
   27. 05. 2004
   European Materials Research Society, Strasbourg, France
2. **Oxygen in High Temperature Superconductors: Oxygen Diffusion and Oxygen Microstructure probed by Transport and Magnetic Measurements**
   23. 06. 2004
   Universität Budapest, Ungarn

Stephan Geprägs

1. **Doping and lattice effects in the half-metallic A2CrWO6**
   6. - 10. 09. 2004
   Joint European Magnetic Symposia, Dresden

Rudolf Gross

1. **Doping and lattice effects in the half metallic double perovskite A_2CrWO$_6$**
   9^{th} Joint MMM/Intermag Conference
   January 5 - 9, 2004, Anaheim, California, USA
2. **Spin injection using half metallic ferromagnets**
   317^{th} WE-Heraeus-Seminar on *Spin Electronics and Spin Optoelectronics in Semiconductors*
   January 11 - 14, 2004, Bad Honnef, Germany
3. **Hochtemperatur-Supraleiter: Einblicke in die Geheimnisse einer faszinierenden Materialklasse**
   29. 01. 2004
   Physikalisches Kolloquium, Fachbereich Physik, Universität Frankfurt.
4. **Hochtemperatur-Supraleiter: Einblicke in die Geheimnisse einer faszinierenden Materialklasse**
   13. 02. 2004
   Physikalisches Kolloquium, Fakultät für Physik, Universität Heidelberg.
5. **Spinelektronik mit ferromagnetischen Oxiden**
   08. 07. 2004
   Kolloquium des Instituts für Festkörper- und Werkstoffforschung Dresden.
6. **Doping dependence of pseudogap and superconductivity in electron doped cuprate superconductors**
   8^{th} Japanese-German Symposium on *Competing Phases in Novel Condensed Matter Systems*
   August 1 – 5, 2004, Lauterbad, Germany
7. **Neue funktionale Schichtsysteme auf der Basis künstlicher heteroepitaktischer Mehrlagenstrukturen aus Übergangsmetalloxiden**
   28. 09. 2004
   Statusseminar des DFG-Schwerpunktprogramms 1157 *Integrierte Elektrokeramische Funktionsstrukturen*, Bonn.
8. **Magnetic tunnel junctions based on transition metal oxides with high spin polarization**
   11^{th} International Workshop on Oxide Electronics,
   Oktober 3 – 5, 2004, Hakone, Japan.

9. **Research at the WMI: Spintronics and Superconducting Quantum Bits**
   06. 10. 2004
   NTT Basic Research Laboratories, Atsugi, Japan.

Rudolf Hackl

1. **A Raman study of electronic correlations in copper-oxygen compounds**
   14. – 15. 06. 2004
   University of Hamburg
2. **Raman Study of Ordering Phenomena in Copper-Oxygen Systems**
   11. – 17. 07. 2004
   Spectroscopies in Novel Superconductors, SNS2004, Barcelona, Spain
3. **Raman Study of Ordering Phenomena in Copper-Oxygen Compounds**
   18. - 23. 07. 2004
   International Conference on Low Energy Electron Dynamics LEES2004, Kloster Banz

Bianca Hermann

1. **Netzwerke und ihre Bedeutung für Wissenschaftskarrieren**
   01. - 02. 04. 2004
   Fonds der Chemischen Industrie, Frankfurt.
2. **Self-Organizing Molecules - Connections to Organic Computing**
   15. 10. 2004
   Institute of AIFB, Karlsruhe.
3. **Overview of the research contribution to the NRP47 "Supramolecular Chemistry"**
   11. 11. 2004
   Institute of Condensed Matter, Basel.

Anton Lerf

1. **Helfen chemische Modifizierungen bei der Interpretation von Mössbauer-Spektren der Tonminerale**
   13. 12. 2004
   Institut für Anorganische Chemie, Universität Bayreuth

Petra Majewski

1. **Thin ferromagnetic oxide films prepared by Pulsed Laser Deposition**
   13. 12. 2004
   Universität Regensburg

Matteo Mariantoni

1. **Circuit-QED with Superconducting Flux Qubits**
   International Workshop on *Solid State Based Quantum Information Processing*
   16. 09. 2004, Herrsching, Germany
2. **Circuit-QED with Superconducting Flux Qubits**
   25. 08. 2004
   Special Seminar: Orlandot's group at Massachussets Institute of Technology (MIT), Boston
3. **Circuit-QED with Superconducting Flux Qubits**
   27. 08. 2004
   USC Condensed Matter Physics Seminar, University of Southern California, Los Angeles

4. **Circuit-QED with flux qubits**
   20. 10. 2004
   Seminar: Tieftemperaturphysik und Mesoskopische Systeme, Universität Erlangen-Nürnberg

Achim Marx

1. **Low frequency 1/f noise in doped manganite films**
   5. - 10. 09. 2004
   Joint European Magnetic Symposia JEMS 04, Dresden

Matthias Opel

1. **Magnetic Tunnel Junctions Based on Oxide Thin Films Structures**
   11. 05. 2004
   Seminar über spezielle Probleme der Halbleiterphysik, Universität Hamburg
2. **Ferromagnetische metallische Oxide mit hoher Spinpolarisation für die Spinelektronik**
   05. 07. 2004
   Projekttreffen BMBF-Verbundprojekt 13N8279, Universität Hannover
3. **Magnetic Tunnel Junctions Based on Heteroepitaxial Oxide Thin Films Structures**
   09. 01. 2004
   9th Joint MMM/Intermag Conference Anaheim, California USA

Erwin Schuberth

1. **Magnetization Studies of the Nuclear Spin Ordered Phases of Solid ^{3}He**
   13. 04. 2004
   3. Sommerschule des EU Projekts *Neutronenstreuung an festem ^{3}He*, Cargese, Corsica
2. **NMR and SQUID Magnetometry in solid ^{3}He**
   29. 08. 2004
   Royal Holloway University, London

Seminars, Courses, Lectures and other Scientific Activities

The WMI Seminars

The Friday Seminar — Walther-Meissner-Seminar on Current Topics in Low Temperature Physics

1. **Quantum Coherent Dynamics in Superconducting Circuits**
   Prof. Dr. Kees Harmans, Dept. of Nanoscience, Delft University of Technology
   16. 01. 2004
2. **Electron correlation effects in expanded liquid metals**
   Dr. Paola Giura, ESRF, Grenoble, France
   23. 01. 2004
3. **Singular band behavior of high T_c superconductors**
   Dr. Ivana Mrkonjic, Dept. of Physics, University of Zagreb
   06. 02. 2004
4. **Design Rules for Perovskites with Novel Magnetic and Electronic Properties**
   Prof. Dr. Bogdan Dabrowski, Dept. of Physics, Northern Illinois University
   12. 02. 2004
5. **Photoemissionspektroskopie in Fe_3O_4**
   David Schrupp, Experimentalphysik II, Universität Augsburg
   13. 02. 2004
6. **Point-contact investigations of electron-phonon interaction and superconducting gaps in diborides**
   Dr. Oksana Kvitnitskaya, Institute for Low Temp. Physics and Engineering, Kharkov, Ukraine
   07. 04. 2004
7. **The role of interfaces in superconducting oxide heterostructures**
   Dr. Gennadij Logvenov, Experimentalphysik VI, Institut f. Physik, Universität Augsburg
   23 04. 2004
8. **Superfluide Turbulenz**
   Prof. Dr. W. Schoepe, Universität Regensburg
   30. 04. 2004
9. **Charged complexes on the surface of liquid helium**
   Dr. Pavel Grigoriev, L.D. Landau Institute for Theoretical Physics, Chernogolovka, Russia
   14. 05. 2004
10. **Low-temperature scanning tunneling microscopy of surface and interface states**
    Dr. Jascha Repp, IBM Zürich Research Laboratory Rüschlikon, Schweiz
    28. 05. 2004
11. **Abbildung elektrischer Transporteigenschaften in magnetischen Tunnelkontakten und in 0 − ß Josephson-Kontakten**
    Prof. Dr. Dieter Kölle, Physikalisches Institut, Universität Tübingen
    04. 06. 2004
12. **Animationen für die Physik**
    Ing. HTL Hans-Rudolf Hidber, Institut f. Physik, Universität Basel
    18. 06. 2004
13. **Spontaneous supercurrent induced by a ferromagnetic π-junction**
    Andreas Bauer, Institut für Experimentelle und Angewandte Physik, Universität Regensburg
    09. 07. 2004
14. **Quantum computing and superconducting qubits**
    Dr. Per Delsing, Microtechnology and Nanoscience Chalmers University of Technology Goeteborg, Schweden
    16. 07. 2004
15. **Ferromagnetic/superconducting nanostructures: From an inhomogeneous superconductivity to a macroscopic two-level system**
    Dr. Marco Aprili, CSNSM-CNRS, Université Paris-Sud and Laboratoire de Physique Quantique

ESPCI, Frankreich
23. 07. 2004

16. **High magnetic field study of $CePd_2Si_2$**
Dr. Ilya Sheikin, Grenoble High Field Laboratory, Frankreich
01. 10. 2004
17. **Electronic properties of hydrogen-terminated diamond surfaces**
Tobias Heimbeck, Walter-Schottky-Institut, Garching
18. 10. 2004
18. **Non-equilibrium dynamics in ultracold glasses**
Dr. Stefan Ludwig, LMU München
22. 10. 2004
19. **Ferromagnetism observed in Mn-alloyed ZnO thin films**
Dr. Heidemarie Schmidt, Universität Leipzig
12. 11. 2004
20. **Magnetotransport in magnetischen Halbleitern**
Dr. Sebastian Gönnenwein, TU Delft, Niederlande
19. 11. 2004
21. **Untersuchung von FeCoV/NiO/FeCoV-Schichten mittels polarisierter Neutronenreflektrometrie**
Dr. Christian Schanzer, Lehrstuhl E21, TU München
26. 11. 2004
22. **Brennstoffzellen**
Claus Huber, Lehrstuhl für Thermodynamik, TUM Garching
03. 12. 2004
23. **Coherent atomic motions in a nanostructure studied by femtosecond x-ray diffraction**
Dr. Michael Woerner, Max-Born-Institut, Berlin
10. 12. 2004
24. **Nachweis von Kupfer in Silizium mit der Transient Ion Drift (TID) Methode**
Robert Christopher Burns, Silitronic AG, Burghausen
14. 12. 2004
25. **Macroscopic Quantum Tunneling in d-wave $YBa_2Cu_3O_7$ Josephson Junctions**
Dr. Thilo Bauch, Chalmers University of Technology
17. 12. 2004

The Tuesday Seminar – SS 2004

1. **Bericht vom APS March Meeting (Teil 1: Supraleitung)**
Rudolf Hackl, Walther-Meissner-Institut, Garching
13. 04. 2004
2. **Die Deutsche Forschungsgemeinschaft (DFG)**
Rudolf Gross, WMI, Garching
20. 04. 2004
3. **Die neue Abteilung "Rastersonden-Mikroskopie"**
Bianca Hermann, LMU München und WMI, Garching
27. 04. 2004
4. **Cryophysics 50 years ago**
B.S. Chandrasekhar, WMI, Garching
04. 05. 2004
5. **Proceedings in the Qubit Lab: Escape Rate Measurements on Josephson Junctions**
Georg Wild, WMI, Garching
11. 05. 2004
6. **Reports on APS March Meeting (Part 2: Quantum Computing)**
Matteo Mariantoni, WMI, Garching
18. 05. 2004
7. **Elektronendotierungsreihe und strukturelle Effekte in ferromagnetischen Doppelperowskiten**
Stephan Geprägs, WMI, Garching

25. 05. 2004
8. **Bestimmung der Spinpolarisation nach der Methode von Meservey und Tedrow**
   Stephanie Wagner, WMI, Garching
   01. 06. 2004
9. **Eigenschaften von n-dotierten Hochtemperatursupraleitern**
   Andreas Winkler, WMI, Garching
   08. 06. 2004
10. **Tunnelmagnetowiderstandseffekt in Sr_2CrWO_6**
    Andrea Boger, WMI, Garching
    15. 06. 2004
11. **Herstellung und Charakterisierung von Phasen-Qubits**
    Heribert Knoglinger, WMI, Garching
    22. 06. 2004
12. **Industrial Property Rights and Patents**
    Dr. Cruz Ramos Flores, Europäisches Patentamt, München
    29. 06. 2004
13. **Mangan-dotiertes Zinkoxid**
    Karl Nielsen, WMI, Garching
    06. 07. 2004
14. **Herstellungsverfahren für Hochtemperatur-Supraleiter**
    Sascha Gasser
    13. 07. 2004
15. **Untersuchung der Zustandsquantisierung in Josephson-Kontakten**
    Karl Madek, WMI, Garching
    21. 07. 2004
16. **Some features of lanthanum manganite magnetic state**
    Prof. Dr. Ya. M. Mukovskii, Moscow State Steel and Alloys Institute
    27. 07. 2004

Topical Seminar on Mesoscopic Systems and Nanotechnology – WS 2003/2004

This topical seminar is held for students in the 7th and 8th semester. It is part of the special physics course on superconductivity and low temperature physics offered by the WMI.

1. **Einführung in die Physik mesoskopischer Systeme: Längen-, Energie- und Zeitskalen**
   Achim Marx
   18. 11. 2003
2. **Herstellungsverfahren für nanostrukturierte Festkörper**
   Edwin Menzel
   25. 11. 2003
3. **Quanteninterferenzeffekte bei Ladungstransport in mesoskopischen Systemen: Aharonov-Bohm-Effekt, Schwache Lokalisierung, universelle Leitwertfluktuationen**
   Bernhard Musch
   02. 12. 2003
4. **Der Quantenhalleffekt**
   M. Schmidt
   09. 12. 2003
5. **Ladungsquantisierungseffekte in kleinen Tunnelkontakten: Der Einzelelektronen-Transistor**
   Holger Specht
   16. 12. 2003
6. **Mesoskopische Supraleiter/Normalleiter/Supraleiter Systeme**
   Andreas Brandlmaier
   13. 01. 2004
7. **Physik ultrakleiner Josephson-Kontakte**
   Chiara Coppi
   20. 01. 2004

8. **Physikalische Eigenschaften von Kohlenstoff-Nanoröhrchen**
   A. Kaniber
   27. 01. 2004
9. **Elektronischer Transport durch atomare Punktkontakte**
   Christian Jäger
   03 02. 2004
10. **Molekulare Elektronik**
    Thomas Niemczyk
    10. 02. 2004

Topical Seminar on Macroscopic Quantum Systems – WS 2004/2005

This topical seminar was held for students in the 7th and 8th semester. It was part of the special physics courses in low temperature physics and quantum phenomena offered by the WMI.

1. **Quantenflüssigkeiten I**
   Dietrich Einzel
   30. 11. 2004
2. **Quantenflüssigkeiten II**
   Dietrich Einzel
   07. 12. 2004
3. **Geladene Quantenflüssigkeiten: Supraleitung**
   Markus Bröll
   14. 12. 2004
4. **Quantenmechanische Grundlagen der Supraleitung**
   Martin Zeppenfeld
   11. 01. 2005
5. **Suprafluide Gyrometer**
   Matthias Kath
   18. 01. 2005
6. **Supraleitende Quanteninterferometer**
   Susanne Hoffmann
   25. 01. 2005
7. **Transporteigenschaften von Quantenflüssigkeiten: Zwei-Flüssigkeiten-Modell**
   Yvonne Gawlina
   01. 02. 2005
8. **Quanteninterferenzexperimente mit atomaren Gasen**
   Riedlberger, Eva
   08. 02. 2005

Lectures

A: Technical University of Munich

Lambert Alff

WS 2003/2004
- Magnetismus (Introduction to Magnetism)

Dietrich Einzel

WS 2003/2004
- Mathematische Methoden der Physik I (Mathematical Methods of Physics I)
- Übungen zu Mathematische Methoden der Physik I (Mathematical Methods of Physik I, Problem Sessions)
- Festkörperkolloquium (Colloquium on Solid State Physics (with R. Gross)
- WMI-Seminar über aktuelle Fragen der Tieftemperatur-Festkörperphysik (WMI Seminar on Current Topics of Low Temperature Solid State Physics) (with R. Gross)
- Farbe (Seminar organisiert von den Sprechern der Wissenschaftler der BAdW)

SS 2004
- Mathematische Methoden der Physik II (Mathematical Methods of Physics II)
- Übungen zu Mathematische Methoden der Physik II (Mathematical Methods of Physics II, Problem Sessions)
- Festkörperkolloquium (Colloquium on Solid State Physics (with R. Gross)
- WMI-Seminar über aktuelle Fragen der Tieftemperatur-Festkörperphysik (WMI Seminar on Current Topics of Low Temperature Solid State Physics) (with R. Gross)

WS 2004/2005
- Mathematische Methoden der Physik I (Mathematical Methods of Physics I)
- Übungen zu Mathematische Methoden der Physik I
- Festkörperkolloquium (Colloquium on Solid State Physics (with R. Gross)
- WMI-Seminar über aktuelle Fragen der Tieftemperatur-Festkörperphysik (WMI Seminar on Current Topics of Low Temperature Solid State Physics) (with R. Gross)

Rudolf Gross

WS 2003/2004
- Applied Superconductivity: Josephson Effects and Superconducting Electronics
- WMI-Seminar über aktuelle Fragen der Tieftemperatur-Festkörperphysik (WMI Seminar on Current Topics of Low Temperature Solid State Physics) (with D. Einzel)
- Festkörperkolloquium (Colloquium on Solid State Physics (with D. Einzel)
- Seminar über Mesoskopische Systeme und Nanotechnologie (Seminar on Mesoscopic Systems and Nanotechnology)

SS 2004
- Spinelektronik (Spin Electronics, with A. Marx)
- Festkörperkolloquium (Colloquium on Solid State Physics (with D. Einzel)
- WMI-Seminar über aktuelle Fragen der Tieftemperatur-Festkörperphysik (WMI Seminar on Current Topics of Low Temperature Solid State Physics) (with D. Einzel)

WS 2004/2005
- Festkörperphysik I (Solid State Physics I)
- Übungen zu Festkörperphysik I in Gruppen (Solid State Physics I, exercises)
- Magnetimus (Magnetism, with M. Opel)
- Festkörperkolloquium (Colloquium on Solid State Physics (with D. Einzel)
- WMI-Seminar über aktuelle Fragen der Tieftemperatur-Festkörperphysik (WMI Seminar on Current Topics of Low Temperature Solid State Physics) (with D. Einzel)
- Seminar über Makroskopische Quantensysteme (Seminar on Macroscopic Quantum Systems)

Rudi Hackl

WS 2004/2005
- Supraleitung und Tieftemperaturphysik I (Superconductivity and Low Temperature Physics I, with D. Einzel)
- Übungen zu Supraleitung und Tieftemperaturphysik I (Superconductivity and Low Temperature Physics I, exercises, with D. Einzel)

Anton Lerf

WS 2003/2004
- Stoffströme in Natur und Technik (mit Prof. Köhler), (Material fluxes in nature and technology)
- Einführung in die Festkörperchemie (mit Prof. Köhler), (Introduction to Solid State Chemistry)

SS 2004
- Übungen zur Vorlesung Physik für Chemiker (Exercises to the lecture Chemistry for Physicists)

WS 2004/2005
- Angewandte Anorganische Chemie (Applied Inorganic Chemistry)
- Moderne Aspekte der Chemie (Modern Aspects of Chemistry)

Erwin Schuberth

WS 2003/2004	• Experimente bei tiefsten Temperaturen 1 (Experiments at very Low Temperatures 1)
SS 2004	• Experimente bei tiefsten Temperaturen 2 (Experiments at very Low Temperatures 2)

B: Ludwig-Maximilians University of Munich

Bianca Hermann

SS 2004	• Experimentalphysik II (Experimental Physics II) (with R. Kersting, R. Netz)
WS 2004/2005	• Selbst-organisierende Moleküle (Self-Organizing Molecules) • Erstkontakt mit der Programmiersprache LabVIEW (First contact with the programming language LabVIEW)

Staff of the Walther-Meissner-Institute

Director
Prof. Dr. Rudolf Gross

Deputy Director
Dr. Werner Biberacher

Technical Director
Dr. Karl Neumaier

Head of the Scanning Probe Division
Prof. Dr. Bianca Hermann

Administration/Secretary's Office

Jutta Laaser	Emel Dönertas

Scientific Staff

Dr. habil. Lambert Alff	Dipl.-Phys. Dieter Andres	Dipl.-Phys. Leonardo Tassini
Dr. habil. Dietrich Einzel	Dr. Boris Philipp	Dipl.-Phys. Matteo Mariantoni
Dr. habil. Andreas Erb	Dr. Daniel Reisinger	Dipl.-Phys. Michael Lambacher
Dr. habil. Rudi Hackl	Dr. Mitja Schonecke	Dipl.-Phys. Stephan Geprägs
Dr. Mark Kartsovnik	Dipl.-Phys. Jürgen Schuler	Dipl.-Phys. Tobias Heimbeck
Prof. Dr. Anton Lerf	Dipl.-Phys. Chiara Coppi	Dipl.-Phys. Wolfgang Prestel
Dr. Achim Marx	Dipl.-Phys. Bettina Welter	Dipl.-Phys. Matthias Kath
Dr. Matthias Opel	Dipl.-Phys. Georg Wild	Dipl.-Chem. Michaela Entfellner
Dr. Christian Probst	Dipl.-Phys. Petra Majewski	
Dr. habil. Erwin Schuberth	Dipl.-Phys. Y. Krockenberger	
Dr. Kurt Uhlig	Dipl.-Phys. Karl-Wilhelm Nielsen	

Technical Staff

Thomas Brenninger	Robert Müller	Christian Reichlmeier
Joachim Geismann	Josef Höss	Harald Schwaiger
Gabrielle Görblich	Julius Klaus	Helmut Thies
Ulrich Guggenberger	Walter Nitschke	Siegfried Wanninger
Dieter Guratzsch	Georg Nitschke	
Wolfgang Hehn	Jan Naundorf	

Assistants

Sybilla Plöderl	Brigitte Steinberg

Permanent Guests
Prof. Dr. B. S. Chandrasekhar
Dr. Robert Doll
Prof. Dr. Schöllhorn

Guest Researchers

1. Prof. Dr. B.S. Chandrasekhar
   permanent guest
2. Dr. Robert Doll
   permanent guest
3. Prof. Dr. Schöllhorn
   permanent guest
4. Prof. Dr. Juan Poyato Ferrera, Instituto de Ciencia de Materiales, Sevilla, Spain
   26. 07. – 13. 08. 2004
5. Dr. Sergei Pesotskii, Institut für Probleme der Chemischen Physik, Chernogolovka, Russia
   23. 03. – 23. 04. 2004
6. Prof. V.G. Peschansky, B.I. Verkin Institute for Low Temp. Physics and Engineering, Kharkov, Ukraine
   01. 07. – 21. 07. 2004
7. Sergey Simonov, Institute of Solid State Physics, Chernogolovka, Russia
   20. 09. – 30. 11. 2004
8. Prof. C. Di Castro, Universitá di Roma "La Sapienza", Rom, Italien
   17. 05. – 12. 06. 2004
9. Prof. T.P. Devereaux, University of Waterloo, Canada
   18. 05. – 29. 07. 2004
10. Dr. Nataliya D. Kushch, Institute of Problems of Chemical Physics, Chernogolovka, Russia
    19. 10. – 18. 12. 2004

Commission for Low Temperature Physics

Members of the Commission for Low Temperature Research of the Bavarian Academy of Sciences:

Kaiser, Wolfgang, Leiter (Technische Universität München)
Brenig, Wilhelm, stellv. Leiter (Technische Universität München)
Gross, Rudolf (Walther-Meißner-Institut)
Landwehr, Gottfried (Universität Würzburg)
Hänsch, Theodor (Max-Planck Institut für Quantenoptik, Garching)
Koch, Frederick (Technische Universität München)
Kotthaus, Jörg Peter (Ludwig-Maximilians-Universität München)
Renk, Karl Friedrich (Universität Regensburg)
Schwoerer, Markus (Universität Bayreuth)
Vollhardt, Dieter (Universität Augsburg)

Prof. Dr. Dierk Rainer, University of Bayreuth, left the Commission for Low Temperature Research in 2004.

Prof. Dr. Dieter Vollhardt has been elected as a new member of the Commission for Low Temperature Research by the Class for Mathematics and Natural Sciences of the Bavarian Academy of Sciences on November 12, 2004.